Development and Validation of an Electromagnetic Formation Flight Simulation as a Platform for Control Algorithm Design

by

Bruno Alvisio

Submitted to the Department of Aeronautics and Astronautics
in partial fulfillment of the requirements for the degree of

Master of Science in Aeronautics and Astronautics

at the

MASSACHUSETTS INSTITUTE OF TECHNOLOGY

February 2015

Signature redacted

Author ....
Department of Aeronautics and Astronautics
December 19, 2014

Certified by.................. Signature redacted ....
David W. Miller
Professor of Aeronautics and Astronautics
Signature redacted Thesis Supervisor

Certified by..
Alvar Saenz-Otero
Principal Research Scientist
Thesis Supervisor

Accepted by .... Signature redacted ....
Paulo C. Lozano
Professor of Aeronautics and Astronautics
Chair, Graduate Program Committee

Development and Validation of an Electromagnetic Formation Flight Simulation as a Platform for Control Algorithm Design

by

Bruno Alvisio

Submitted to the Department of Aeronautics and Astronautics
on December 19, 2014, in partial fulfillment of the
requirements for the degree of
Master of Science in Aeronautics and Astronautics

Abstract

Electromagnetic Formation Flight (EMFF) consists of using electromagnetic forces to position or orient satellites in a relative target location or attitude and achieve a certain target formation on orbit. This thesis introduces the fundamental equations of EMFF and the design of the Resonant Inductive Near-Field Generation System (RINGS). RINGS is a testbed composed of two vehicles that are used to demonstrate EMFF in a 6 DoF environment. In this thesis, a RMS current level controller is modeled and implemented in RINGS to give the system electromagnetic actuation capability. Subsequently, a simulation of RINGS that incorporates an EM dynamics model applicable to two RINGS vehicles operating in close proximity is developed. This model was validated using a set of open-loop maneuvers by comparing it with data obtained from experiments using the RINGS aboard the International Space Station (ISS). Finally, this simulation was used to test linear controllers that incorporate an 'Adaptive Control' approach to achieve system stability for a specific configuration and range of disturbances.

Thesis Supervisor: Alvar Saenz-Otero
Title: Principal Research Scientist

Acknowledgments

I am grateful to my academic advisers Prof. David W. Miller and Dr. Alvar Saenz-Otero for their guidance and for giving me the opportunity to work on the RINGS program. Thank you to Professor Raymond Sedwick and the UMD team, Prof. Enrico Lorenzini, 1st Lt. Gregory Eslinger, LTJG Alexander Buck, Aurora Flight Sciences and DARPA for making this project possible.

I also want to give special thanks to my colleague 2nd Lt. Andrew Hilton for working with me in the RINGS project for the past two years. Drew has given extremely valuable input and insight to all portions of this project.

I want to thank all my friends who have walked with me along the way. In life chronological order: Luciano Bortolin, Nicolás Tusca, Juan Ángel Rodriguez, Frank Hall Schmidt and Christopher Jewison. Thank you for being extremely patient with me (I know how annoying I can sometimes be) and for always being there to listen me complain. You all have taught me how to become a better person and friend.

I want to thank my parents Diego and María Claudia for being a constant source of support. Finally, I want to express my gratitude to my two ultimate sources of inspiration, my brothers: Fernando and Marcelo. Both have always guided me in the right direction since the day I was born and you have been my examples to follow.

Contents

1 Introduction **19**

1.1 Motivations for Electromagnetic Formation Flight (EMFF) 19

1.2 Previous Work 21

1.2.1 EMFF Control 21

1.2.2 EMFF Testbeds 22

1.3 Resonant Inductive Near-Field Generation System (RINGS) 22

1.3.1 RINGS Hardware Description 23

1.3.2 RINGS Firmware 26

1.3.3 EMFF Near-Field Dynamics Model 26

1.4 Thesis Overview 29

2 Modeling and Implementation of a PI Current Controller for RINGS **31**

2.1 Introduction 31

2.2 Motivation 31

2.3 Proportional-Integrator (PI) Controller 33

2.4 'Ziegler-Nichols' Method for Tuning PI Controller Gains 34

2.5 One-Coil Model 36

2.6 One-Coil PI Current Controller Model 38

2.7 Two-Coil PI Current Controller Model 40

2.8 Summary 45

3 SPHERES - RINGS Simulation (SRS) **47**

3.1 Introduction 47

3.2 Description of SPHERES Simulation 47

3.3 Description and Integration of RINGS Simulation 51

3.3.1 RINGS Units Firmware & SPHERES - RINGS Communication 55

3.3.2 RINGS PI Current Controller 56

3.3.3 Features Excluded from the SRS 58

4 SPHERES - RINGS Simulation (SRS) Validation 61

4.1 SPHERES - RINGS Test Design 61

4.2 Coordinate Frames 63

4.3 RINGS Physical Parameters Tuning 63

4.4 RINGS Physical Parameters Validation 71

4.5 EM Force Validation 76

4.6 RINGS Hardware/Software Verification 84

4.7 EM Force Validation: Repulsion 89

4.8 EM Torque Validation 91

4.9 Summary 94

5 Evaluation of Closed-Loop Position Controllers Using the SRS 97

5.1 Introduction 97

5.2 Description of the CLPC 98

5.3 Axial Station Keeping Tests for Optimal RU Orientation 100

5.4 Step Input Tests 104

5.5 Direct Adaptive Control 106

5.6 Summary 107

6 Conclusions and Future Work 109

6.1 Conclusions 109

6.2 Future Work 110

A RINGS - SPHERES Communication Interface and API 117

A.1 RINGS Communication Interface 117

A.1.1 Integration of RINGS to a SPHERES GSP Project 117

A.1.2 RINGS Packet Structure 118

A.1.3 Transmitted Messages 119

A.1.4 Received Messages 121

A.1.5 Telemetry Data Conversion Tables 122

A.2 SPHERES - RINGS API 123

B SPHERES - RINGS Simulation - Payload UART TX/RX MATLAB Code 125

List of Figures

1-1 SPHERES-RINGS Unit [1] 23

1-2 RINGS Unit Coil Schematic [2] 24

1-3 RLC Circuit Diagram [2] 25

1-4 Two Loops of Current [3] 28

1-5 Near vs Far-Field - Relative Error for Axial Force and Shear Torque [4] 29

2-1 I_{ss} vs. Duty Cycle for different (V_{Batt}) [2] 32

2-2 RINGS Response to 20 % DC Input Step 34

2-3 RINGS Response to 60 % DC Input Step 35

2-4 'One-Coil Model' Block Diagram [2] 36

2-5 One-coil Model vs. Experiment - Response to 20 % DC Step 37

2-6 One-coil Model vs. Experiment - Response to 60 % DC Step 37

2-7 PI Current Controller Model Block Diagram 38

2-8 One-Coil PI Current Controller Model - System Response to a 12A Step Input 39

2-9 One-Coil PI Current Controller Model - System Response to a -9A Input Step 40

2-10 Two-Coil PI Current Controller - Simulation Block Diagram [2] . . . 41

2-11 Coupling coefficient (κ) vs. Axial Separation Distance [2] 42

2-12 Two-Coil Experimental Set-Up 43

2-13 Two-Coil PI Current Controller Simulation vs. Experiment - Scenario 1 43

2-14 Two-Coil PI Current Controller Simulation vs. Experiment - Scenario 2 44

2-15 Two-Coil PI Current Controller Simulation vs. Experiment - Scenario 3 44

3-1 SPHERES Test Development Process 48
3-2 SPHERES Simulation Block Diagram [5] 49
3-3 SRS Block Diagram 52
3-4 SRS Block Diagram - RINGS Units & EM Physics Model 53
3-5 SRS Block Diagram - State Input 54
3-6 SRS Block Diagram - Output Variables 54
3-7 RINGS Communication Buffer 56
3-8 RLC Circuit Current with Lowpass Filter 57
3-9 RU RLC Circuit Dynamics Test - Experiment vs. SRS 58

4-1 RINGS Test Initial Position Set-Up 62
4-2 Body (blue) & Inertial (black) Reference Frames 63
4-3 Thruster Test Timeline 64
4-4 RINGS Unit Angular Velocity - SRS Results 66
4-5 RINGS Unit Angular Velocity - ISS 67
4-6 SPHERES-RINGS Thrusters Impingement 68
4-7 Gyro Readings - ISS vs. SRS 70
4-8 Y-Axis Accelerometer Readings - ISS vs. SRS 70
4-9 RU 1 Position - ISS Test vs. SRS 73
4-10 RU 1 Attitude - ISS Test vs. SRS 74
4-11 RU 1 Position and Attitude Error - ISS Test vs. SRS 74
4-12 EM Actuation Test - Current Profile 76
4-13 EM Actuation Test - RU 2 Position Oscillations 78
4-14 EM Actuation Test - RU 2 Attitude Oscillations 78
4-15 SRS Validation of Axial EM Tests - Inputs 79
4-16 Axial EM Type 1 Test - RU 1 Position - ISS Test vs. SRS 79
4-17 Axial EM Type 1 Test - RU 1 Position Error - ISS Test vs. SRS . . . 80
4-18 Axial EM Type 3 Test - RU 1 Position - ISS vs. SRS with 'Drag Model' and 'Current Model' 83

4-19 Axial EM Type 3 Test - RU 1 Error - ISS vs. SRS with 'Drag Model' and 'Current Model' 83

4-20 RINGS Hardware Verification - Induced Voltage - 3A RMS 85

4-21 RINGS Hardware Verification - FFT - 3A RMS 85

4-22 Hardware Verification Test Setup 87

4-23 Commanded vs. Real I_{RMS} Current - Error: 8.6% 87

4-24 Hardware Verification - Phase Shift Anomaly 88

4-25 Axial EM Repulsion Test - Position 90

4-26 Axial EM Repulsion Test - Error 90

4-27 EM Shear Test - Initial Configuration 91

4-28 SRS Validation of Shear Tests - Inputs 92

4-29 Shear EM Test Type 1 - RU 1 Position - ISS vs. SRS 92

4-30 Shear EM Test Type 1 - RU 1 Attitude - ISS vs. SRS 93

4-31 Shear EM Test Type 1 - RU 1 Error - Validation 94

5-1 PID Position Controller 99

5-2 Mixer Function for Axial Configuration - I_{RMS}/F vs. Axial Separation Distance 100

5-3 Test - Configuration A 101

5-4 Test - Configuration B 101

5-5 PID Controller - Test 1 (Configuration A) 102

5-6 PID Controller - Test 2 (Configuration B) 103

5-7 PID Controller - Test 3 - Step Input - Attraction 104

5-8 PID Controller - Test 4 - Step Input - Repulsion 105

5-9 EM PID Controller with 'Input Shaping' 106

5-10 EM PID Controller - Input Shape - Repulsion 107

A-1 SPHERES-RINGS Packet Structure 119

List of Tables

2.1 Two-Coil PI Current Controller Model vs. Experiment - RMS Error . 45

3.1 SRS Output Variables 55

4.1 SPHERES-RINGS Moment of Inertia - Baseline 64

4.2 SPHERES-RINGS Center of Mass - Baseline 64

4.3 SPHERES Thrusters Torque Direction 66

4.4 SPHERES-RINGS Moment of Inertia - ISS 68

4.5 SPHERES-RINGS Center of Mass - ISS 69

4.6 SPHERES-RINGS Thrusters Force Matrix - ISS 69

4.7 RINGS PD Controller Gains for Initial Positioning 72

4.8 System Response Characteristics 72

4.9 'Initial Positioning' Phase - RU 1 Target Position and Attitude 73

4.10 Thruster Actuation in 6 DOF 77

4.11 Drag Model Parameters 81

4.12 'Current Model' Parameters 82

4.13 RINGS Hardware Verification - Additional Power 86

5.1 CLPC Test Parameters 98

5.2 PID Controller Performance Comparison - Configuration A vs. B . . 104

A.1 Mode Packet Structure Details 119

A.2 PWM Packet Structure Details 120

A.3 RMS Current Packet Structure Details 120

A.4 Short Telemetry Packet Structure Details 121

A.5 Long Telemetry Packet Structure Details 122

A.6 Operation Mode Acknowledgment Packet Structure Details 122

A.7 RINGS Units Sensor Gains and Physical Parameters 123

A.8 Telemetry Data Conversion Factors 123

List of Acronyms and Initialisms

ADC - Analog to Digital Converter
AFS - Aurora Flight Sciences
AI - Astronomical Interferometry
CFD - Computational Fluid Dynamics
CoM - Center of Mass
DARPA - Defense Advanced Research Projects Agency
DOF - Degree of Freedom
DSP - Digital Signal Processor
ELC - Express Laptop Computer
EMF - Electromotive Force
EMFF - Electromagnetic Formation Flight
ESA - European Space Agency
EXPV2 - Expansion Port Version 2
FFT - Fast Fourier Transform
GMS - Global Metrology System
GSP - Guest Scientist Program
GUI - Graphical User Interface
HES - Hall-Effect Sensor
HTS - High-Temperature Superconductor
IC - Integrated Circuit
ISS - International Space Station
LEO - Low Earth Orbit
MIT - Massachusetts Institute of Technology
MOSFET - Metal-Oxide Field Effect Transistor
NASA - National Aeronautics and Space Administration
OS - Operating System
PADS - Position and Attitude Determination System
PD - Proportional-Derivative
PID - Proportional-Integral-Derivative
PWM - Pulse Width Modulation
RGA - Reduced Gravity Aircraft
RINGS - Resonant Inductive Near-field Generation System
RMS - Root Mean Square
RRM - Robotic Refueling Mission
RTOS - Real-Time Operating System
RU - RINGS Unit

SIT - System Identification Test
SK - Station Keeping
SPDM - Special Purpose Dexterous Manipulator
SPHERES - Synchronized Position Hold Engage and Reorient Experimental Satellites
SRS - SPHERES-RINGS Simulation
SSL - Space Systems Laboratory
TOF - Time of Flight
TPF - Terrestrial Path Finder
UART - Universal Asynchronous Receiver/Transmitter
UMD - University of Maryland
US - Ultra Sound
USB - Universal Serial Bus
VERTIGO - Visual Estimation for Relative Tracking and Inspection of Generic Objects
WPT - Wireless Power Transfer

Chapter 1

Introduction

1.1 Motivations for Electromagnetic Formation Flight (EMFF)

Electromagnetic Formation Flight (EMFF) consists of using electromagnetic forces to position or orient satellites in a relative target location or attitude to achieve a certain formation in orbit. Having this capability of keeping a cluster of satellites with similar orbital parameters could enable multiple technologies:

1. Astronomical Interferometry (AI): Relies on an array of satellites in close proximity to take images of a target location of a space body. By cross-referencing these images, the angular resolution of the instrument is comparable to the one that would be obtained by a single telescope with a much larger aperture. The 'Darwin' mission is an ESA study that consisted of a constellation of four to nine spacecrafts to detect Earth-like planets orbiting nearby stars. However, the development of this proposal was stopped in 2007 [6].

2. Fractionated Spacecraft Architecture: Brown et al. [7] proposed a new architectural paradigm called 'Fractionated Spacecraft' in which a satellite is decomposed into different modules. These components communicate wirelessly to achieve certain tasks while orbiting in a cluster. This architecture seeks not only

to reduce program development time but also make the system more flexible and robust to uncertainties.

3. Robotic Assembly: For some missions the aforementioned 'Fractionated Architecture' may not be a viable solution. In order to overcome limiting factors imposed by size and weight of the spacecraft, a possible solution is to launch modules separately and assemble them while in orbit using robots. Everist proposes an experimental system for assembly in space [8]. As an example, the Special Purpose Dexterous Manipulator (SPDM), a two armed robot aboard the ISS, has been used in the Robotic Refueling Mission (RRM) to show its capability to perform tasks such as unscrew caps and adjust valves of a module that was not originally designed to be serviced [9].

Multiple technologies can be used to correct for disturbances and achieve a target formation. One solution is to use thrusters as the actuation system. However, given that spacecrafts can only carry a limited amount of propellant this solution poses a limitation in the operational lifetime of the cluster. A second alternative is to use tethers between the spacecrafts that form the cluster. However, this solution requires the deployment of tethers in space which has proven to be an extremely difficult task that limits the possible orientations of the cluster.

In EMFF magnetic fields are generated by the different nodes of the cluster. The interaction of these fields generate electromagnetic forces and torques that are used to control and maintain the formation. Due to the Conservation of Momentum and the fact that all the electromagnetic forces generated are internal to the cluster, its center of mass (CoM) cannot change. Thus, the EMFF approach can only be used to control the relative position and attitude of the spacecraft.

EMFF has three major advantages over the aforementioned solutions. This technology is propellant-free since the electrical currents required to generate the magnetic fields can be obtained from sustainable sources such as batteries that are charged using solar panels. Thus, the operational lifetime constraint would be eliminated since the system would have a replenishable power source. The second major advantage is for missions that have payloads with optical sensors that can be damaged by propellants. As an example, the Terrestrial Path Finder (TPF) mission utilizes an infrared interferometer to detect an Earth-like planet [10]. In this mission a cluster of satellites rotate in close proximity and the plume of the thrusters could cloud the sensors.

A complementary application of EMFF is Wireless Power Transfer (WPT). WPT consists in generating an alternating magnetic field to transfer energy to another device wirelessly. This technology adds flexibility to the mission architecture since some spacecraft in the cluster could only be responsible for power generation and distribution while other spacecraft could be specialized in the science objective and be powered remotely.

1.2 Previous Work

1.2.1 EMFF Control

A significant amount of work on EMFF control has been published. The concept of using electromagnetic forces for space Formation Flight in Low Earth Orbit (LEO) is originally presented in series of papers by Hashimoto, Sakai, Ninomiya, et al. [11].

Elias [12] developed an EMFF dynamics model that considered satellites to have a fully controllable dipole and showed closed loop controllability of the system. Satellites are assumed to be a distance great enough from each other that they can be modeled as magnetic dipoles.

In his thesis, Schweighart [3] developed three models for EM forces and torques, namely 'Near-Field', 'Mid-Field' and 'Far-Field'. In his work, closed form solutions for the 'Mid-Field' and 'Far-Field' are derived and control methods for multi-satellite clusters are given.

Wawrzaszek et al. [13] developed a linear model for a two-satellite cluster that performs a spin-up maneuver. Their work proves that feedback control is required for system stability and a linear controller is shown to stabilize the system for a range of disturbances.

1.2.2 EMFF Testbeds

Since 2004, multiple testbeds have been developed in the Space Systems Laboratory (SSL) at MIT:

1. In 2004, a 1-Dimensional EMFF testbed was created [12]. It featured one electromagnet fixed at one end of a linear track while a second electromagnet was able to float in the track. By changing the current in the magnets and using an ultrasonic device to measure position, it was possible to control the position of the magnet floating on the track.

2. In 2005, a 2-Dimensional EMFF testbed (3 DoF) was created [14]. It consisted of two vehicles that floated on a flat floor using air carriages. Each vehicle was equipped with two coils that were orthogonal to each other. The material used was High-Temperature Superconducting wire (HTS) to allow the circulation of high levels of current and generation of appreciable forces.

3. A 1-Dimensional testbed, known as μEMFF [15], used two non-superconducting coils to test different control algorithms and demonstrate the possibility of achieving EMFF using non-superconducting electromagnets.

1.3 Resonant Inductive Near-Field Generation System (RINGS)

The Resonant Inductive Near-Field Generation System (RINGS) is an experimental testbed to demonstrate EMFF and WPT in a micro-gravity environment. RINGS is composed of two vehicles, referred to as RINGS units (RUs), that integrate to the Synchronized, Position Hold, Engage, Reorient, Experimental Satellites (SPHERES) and was launched to the International Space Station (ISS) in August 2013. SPHERES satellites are placed on the center of the RU and are equipped with their own propulsion, power and navigation system. These satellites are capable of being programmed to perform different type of maneuvers such as autonomous rendezvous and docking [16] [17] [18]. Figure 1-1 shows one RU:

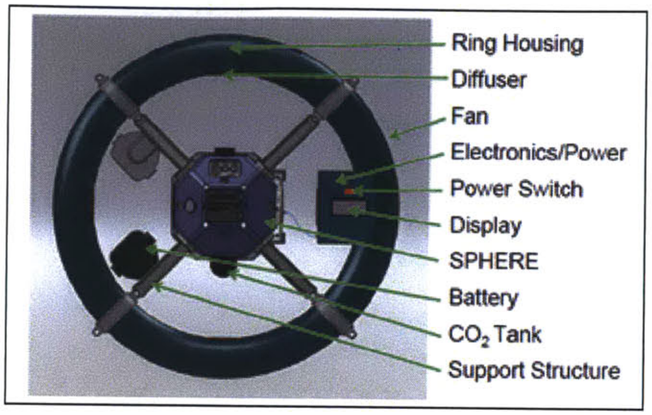

Figure 1-1: SPHERES-RINGS Unit [1]

The RUs can be configured to operate in the following 'Operational Modes':

1. Electromagnetic Formation Flight (EMFF): the RUs generate attractive, repulsive forces and torques that can be used to control the vehicles.
2. Wireless Power Transfer (WPT): One RU generates alternating magnetic fields to transfer energy to the secondary RU which dissipates it through a load resistor connected in series with the circuit.

1.3.1 RINGS Hardware Description

This section provides an overview of the RUs RLC circuit, also known as 'resonant coil', which is the component that generates the magnetic fields for EMFF and WPT. RINGS circulate AC current through the resonant coils due to requirements imposed by WPT and to eliminate parasitic torques derived from the coil's interaction with the Earth's magnetic field. In his thesis, Alinger [2] gives a full description of the RINGS design and implementation.

RLC Circuit

RUs' resonant coil is constructed from a rectangular cross-section wire. The average diameter of the coils is 0.62 meters. This design was chosen because it allowed SPHERES satellites and RINGS electronics to be placed on the center of the coil structure. Each layer of wire has 20 turns and the coil consist of five layers that are placed on top of each other and connected in series. These design decisions were driven by the criteria that the RUs should be able to exert enough rotational force to allow the RUs to perform a circular maneuver in a period of 1 minute. The coil wire material is 6061 aluminum due to beneficial heat treatment properties during construction and its market availability in the desired aspect ratio. Figure 1-2 shows an schematic of the coil; in red are shown the poly-carbonate spacers used to prevent the contact between turns and layers and give structural rigidity to the coil.

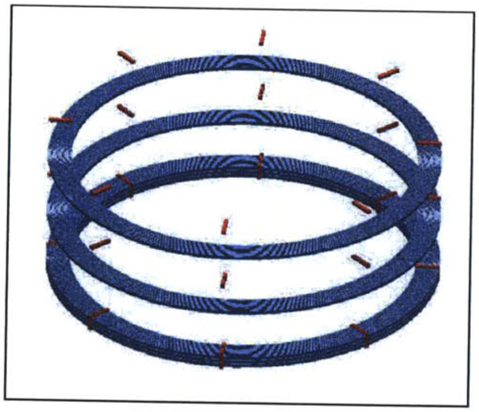

Figure 1-2: RINGS Unit Coil Schematic [2]

Figure 1-3 shows the circuit diagram of the resonant coil and the driving circuit in the EMFF configuration. The resonant coil drive circuit is based on a H-Bridge architecture. This architecture allows the generation of alternating current. Its frequency and amplitude are controlled by varying the frequency at which the metal-oxide field effect transistors (MOSFETs) are switched 'ON' and 'OFF' and duty cycle of the applied voltage. An alternative architecture using High Power Operational Amplifiers was also considered but it was not viable due to thermal dissipation issues caused by the high power level that operational amplifiers would draw.

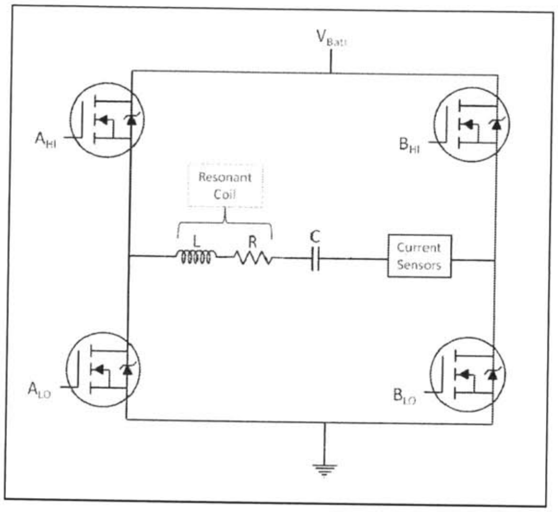

Figure 1-3: RLC Circuit Diagram [2]

EMFF operational frequency was desired to be as low as possible. Given physical, thermal and operational design constraints, a $310uF$ capacitor was chosen for the EMFF configuration. From experimental results obtained by Alinger et al. [2] it was determined that for frequencies lower than $1kHz$, the inductance and resistance of the RUs' resonant coils are:

$$\begin{aligned} L &= 11.9mH \\ R &= 1.1\Omega \end{aligned}$$

Given these values, the resonant frequency of the RLC circuit in the EMFF configuration is:

$$f_{EMFF} = \frac{1}{2\pi\sqrt{LC}} = \frac{1}{2\pi\sqrt{11.9mH * 310\mu F}} = 82.90Hz \approx 83Hz$$

Current Sensors

The current that flows through the resonant coils is measured by ACS709LLFTR-20BB-T Hall-Effect sensors (HES) manufactured by Allegro Microsystems. For redundancy, three HESs are in series with the circuit. In addition, the RUs are equipped with a pair of LTC1968 RMS-to-DC converters manufactured by Linear Technology.

1.3.2 RINGS Firmware

RUs are equipped with a PIC32MX340F512H manufactured by Microchip. Given the existing capabilities and software infrastructure in SPHERES, it was decided that the functional requirements of the firmware would be to:

1. Configure the internal RLC circuit to the different operational modes: IDLE, EMFF, WPT-TX, WPT-RX.
2. Drive the current flowing through the coils to a commanded RMS level.
3. Synchronize the current waves using the IR pulses received.
4. Receive measurements from the system sensors and change to any 'Error Mode' accordingly.
5. Send acknowledgement messages and telemetry data back to the SPHERES satellite.

1.3.3 EMFF Near-Field Dynamics Model

Models of EM forces and torques can be classified into three major categories according to the relative distance between the spacecraft that are generating the magnetic fields:

1. Near-Field Model: Is the exact solution to the magnetic forces and torques generated in an EMFF system.
2. Far-Field Model: When the vehicles are sufficiently far away, they can be modeled as point magnetic dipoles and their exact geometry can be ignored. This model is the first order Taylor series expansion of the force between the two vehicles.

3. Mid-Field Model: For situations in which satellites need to operate in close proximity, the Far-Field model is inaccurate. The Mid-Field model incorporates the next higher order expansion of the Taylor series.

RINGS operates in the SPHERES test volume aboard the ISS. Thus, given the small operational distances between the vehicles the Far-Field model assumption does not hold and the Near-Field model must be used instead. The rest of this section describes the governing equations of the Near-Field model.

According to the 'Lorentz Force Law', a continuous charge distribution in motion in the presence of a magnetic field can be described by the following equation:

$$d\vec{F} = i\vec{dl} \times \vec{B} \tag{1.1}$$

By applying equation 1.1, Biot-Savart's Law and Faraday's Law the resulting EM force and torque of two loops carrying current are [3]:

$$F_{ij} = \frac{\mu_0 I_i I_j}{4\pi} \oint_i \oint_j \frac{\vec{dl}_i \times \left(\vec{dl}_j \times \hat{r}_{ij}\right)}{\|\vec{r^2}\|} \tag{1.2}$$

$$\tau_{ij} = \frac{\mu_0 I_i I_j}{4\pi} \oint_i \oint_j \vec{R}_i \times \frac{\vec{dl}_i \times \left(\vec{dl}_j \times \hat{r}_{ij}\right)}{\|\vec{r^2}\|} \tag{1.3}$$

where F_{ij} and τ_{ij} are the resulting force and torque on loop i due to loop j respectively, μ_0 is the permeability of free space and $\vec{dl}_i$ is an infinitesimal length of conductor i. Equations 1.2 and 1.3 assume that all segments of loop i and j carry the same level of current I_i and I_j respectively. $\vec{R}_i$ is the position vector of element $\vec{dl}_i$ relative to the center of mass of object i as shown in Figure 1-4:

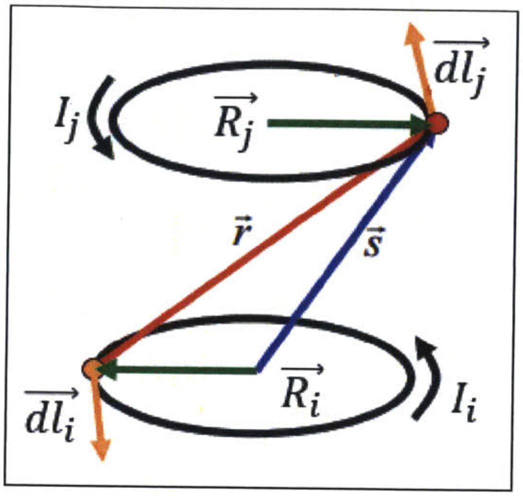

Figure 1-4: Two Loops of Current [3]

Equations 1.2 and 1.3 have no analytic solution. In order to create a high-fidelity numerical simulation that can be applied to scenarios where the two loops of current are in close proximity, a discrete form of 1.2 and 1.3 is used:

$$F_{ij} = \frac{\mu_0}{4\pi} \sum_{i=1}^{N_i} \sum_{j=1}^{N_j} \frac{I_i \vec{dl}_i \times \left(I_j \vec{dl}_j \times \hat{r}_{ij} \right)}{\|\vec{r^2}\|} \tag{1.4}$$

$$\tau_{ij} = \frac{\mu_0}{4\pi} \sum_{i=1}^{N_i} \sum_{j=1}^{N_j} \vec{R}_i \times \frac{I_i \vec{dl}_i \times \left(I_j \vec{dl}_j \times \hat{r}_{ij} \right)}{\|\vec{r^2}\|} \tag{1.5}$$

where N_i and N_j are the model parameters that determine the number of segments used to represent the coils. In his thesis, Buck [4] describes an 'Intelligent Discretization' method to choose these parameters depending on the range of distances between the two loops. In addition, [4] compares: (1) the forces of the Near-Field numerical simulation to the Far-Field model for the case in which the RUs' coil plane normal vectors are co-axial (RUs are facing each other) and (2) the torques for the case in which the RUs' coil normal vectors are orthogonal. Figure 1-5 shows the relative error of the Far-Field model for the two cases mentioned above:

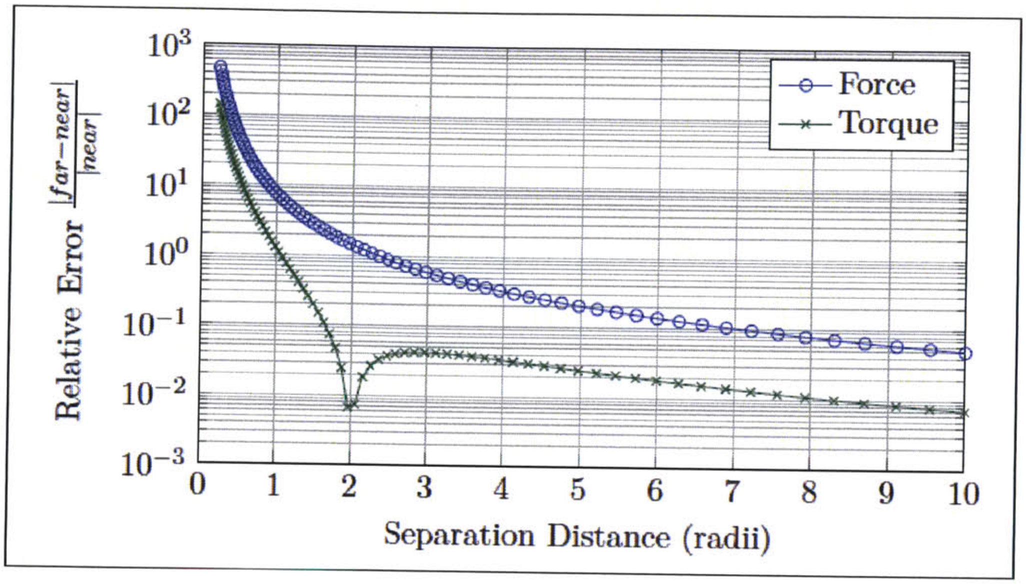

Figure 1-5: Near vs Far-Field - Relative Error for Axial Force and Shear Torque [4]

In Figure 1-5 the X-axis is normalized to the RUs' radius. It is shown that at 7 radii (approximately 2.1 meters), the relative error between the Far-Field and Near-Field models is above 10%. Thus, for the operational distances of RINGS the figure above proves that the Far-Field model is not applicable and the Near-Field model has to be used instead.

1.4 Thesis Overview

The majority of this thesis involves the development and validation of a simulation of RINGS. In addition, closed-loop controllers for RINGS are developed and tested in simulation to achieve position control. This work is organized as follows:

- Chapter 2 explains the motivation for a current controller for RINGS. A model of a PI Current Controller for RINGS is developed. The behavior of the system is simulated in SIMULINK and then compared to experiments performed on the engineering RUs. The objective of these experiments is to study the response and stability of the system when using a PI current controller.

- Chapter 3 starts by describing the SPHERES simulation developed by Katz [5].

Then, it presents the development of the SPHERES-RINGS Simulation (SRS) and a description of the different components and their integration with the SPHERES simulation.

- Chapter 4's objective is to validate the SRS developed in the previous chapter by comparing experimental data obtained aboard the ISS with simulation results. Partial results show the necessity to modify the initial version of the SRS and a justification for these modifications are given.
- Chapter 5 develops a closed-loop position controller that uses EM actuation for a single axis and SPHERES thrusters for the other 5 DoF. This controller is simulated in the SRS to test the stability of the system. Due to the instability observed in certain maneuvers, an 'Adaptive Control' method known as 'Reference Input' is implemented and tested to achieve stability of the system.
- Chapter 6 summarizes the conclusions of this work and it suggests future steps for the progress of the RINGS program and the demonstration of EMFF in a micro-gravity environment.

Chapter 2

Modeling and Implementation of a PI Current Controller for RINGS

2.1 Introduction

This chapter describes the motivation, development and testing of a Proportional-Integrator current controller for the RINGS. Initially, a 'One-Coil Model' was implemented in Simulink to test the performance of the PI controller. In this model only one RU with a PI controller is simulated. Then a 'Two-Coil Model' was developed to study the impact that inductive coupling between two RUs has in the performance of the PI controller. The simulation results are also compared against experimental tests performed in the ground testbed.

2.2 Motivation

Equations 1.2 and 1.3 show that the EM force and torque are directly proportional to the loop currents i_1 and i_2. Given that the frequency of the sinusoidal field for EMFF ($83Hz$) is fast when compared to the rigid body motion, the average result across time is identical to a non-oscillating system driven at the Root Mean Square (RMS) level of the sinusoidal system. Thus, the control variable of interest becomes the RMS current level flowing in the loops.

The RUs' RLC circuit is driven by controlling an H-bridge (see Section 1.3.1), using a PWM signal to generate alternate voltage and subsequently control the level and frequency of the current flowing through the circuit (see Figure 1-3). With this architecture, using Fourier series expansions, the steady-state current is:

$$I_{ss}(t) = V_{Batt} \sum_{n=1}^{\infty} D_n \left|G_n\right| cos\left(\frac{2\pi n}{T}t - \phi_n + \angle G_n\right) \tag{2.1}$$

where G_n is the RLC circuit transfer function and:

$$\begin{aligned}
D_n &= \sqrt{A_n^2 + B_n^2} \\
\phi_n &= tan^{-1}\left(\frac{B_n}{A_n}\right) \\
A_n &= \frac{2}{n\pi} sin\left(\frac{\pi n t}{T}\right)\left(cos\left(\frac{\pi n t}{T}\right) - cos\left(\frac{\pi n\,(t-T)}{T}\right)\right) \\
B_n &= \frac{2}{n\pi} sin\left(\frac{\pi n t}{T}\right)\left(sin\left(\frac{\pi n t}{T}\right) - sin\left(\frac{\pi n\,(t-T)}{T}\right)\right) \\
G_n &= \frac{1}{j\omega_n L(\omega_n) + R(\omega_n) + \frac{1}{j\omega_n C}}
\end{aligned}$$

Equation 2.1 shows that the current is directly proportional to raw battery voltage V_{Batt}. As the RU uses battery's energy, V_{Batt} decreases and for a given Duty Cycle (DC) the I_{ss} will also decrease. Figure 2-1 shows simulation results performed by Alinger [2] where the effect on I_{ss} when varying V_{Batt} is assessed:

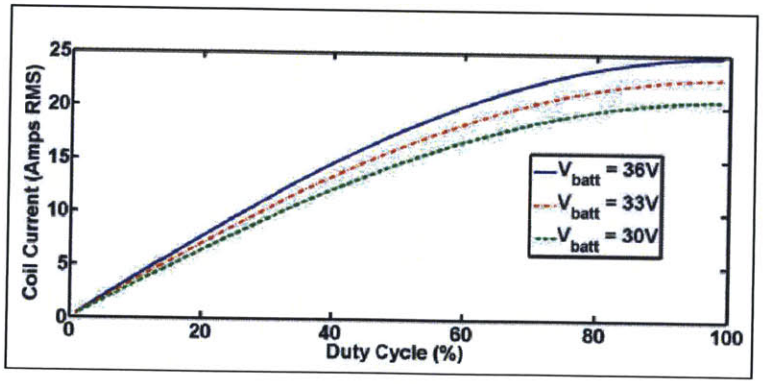

Figure 2-1: I_{ss} vs. Duty Cycle for different (V_{Batt}) [2]

It is observed that the battery voltage has a significant effect on the RMS current. For example, at 60% DC, the RMS current decreases by 17% (from 20A to 16.7A) when V_{Batt} decreases from 36V to 30V.

In addition to the fluctuation of the battery voltage, the level of current flowing though the coils will be affected by the 'inductive coupling'. According to Faraday's Law of Induction, the time rate of change of the magnetic flux through the circuit will induce an Electromotive Force (EMF) in any other closed circuit. The magnitude of the EMF is proportional to the time rate of change of the magnetic flux, the RUs coil inductance, and the coupling coefficient. The coupling coefficient, κ, is a geometric constant between 0 and 1 that represents the effective magnetic flux that goes through the second RU's coil. Thus, the change in current in one RU will create a disturbance on the current level of the second RU and vice versa.

2.3 Proportional-Integrator (PI) Controller

From the previous discussion, it was decided to develop a PI current controller that is capable of maintaining a reference RMS current level and is robust to the disturbances created by the inductive coupling. The equation for a PI controller is:

$$C(t) = K_P * E(t) + K_I * \int_0^t E(t)dt \tag{2.2}$$

where K_P and K_I are the proportional and integral gains respectively. Given that the PI controller will be digital, the integral term was approximated using:

$$\int_0^t E(t)dt \approx T_S \sum_{n=0}^{N} E(n) \tag{2.3}$$

where T_S is the sampling period. The equation for the PI controller becomes:

$$C(n) = K_P * E(n) + K_I * T_S \sum_{n=0}^{N} E(n) \tag{2.4}$$

2.4 'Ziegler-Nichols' Method for Tuning PI Controller Gains

The baseline optimal gains for the PI controller were estimated using the 'Ziegler-Nichols' method and then they were slightly tuned to achieve the desired response.

In order to determine the optimal gains for the system, we give the physical system (RU) a step input and measure the response. Figures 2-2 and 2-3 show the response of the system when an input step of 20% and 60% DC were commanded at time $t = 0$. The RMS current step given to the system is:

$$I_{RMS\_20} = \frac{V_{Batt} * 0.2}{R} * \frac{1}{\sqrt{2}} = \frac{0.2 * 36V}{1.2\Omega} * \frac{1}{\sqrt{2}} = 4.25A$$

$$I_{RMS\_60} = \frac{V_{Batt} * 0.6}{R} * \frac{1}{\sqrt{2}} = \frac{0.6 * 36V}{1.2\Omega} * \frac{1}{\sqrt{2}} = 12.76A$$

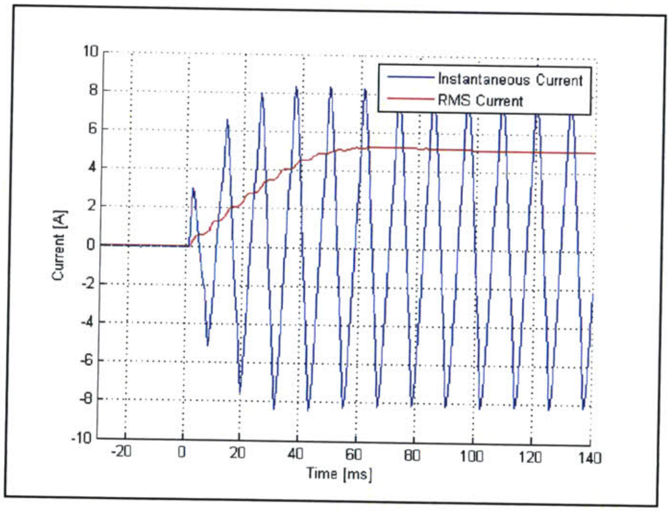

Figure 2-2: RINGS Response to 20 % DC Input Step

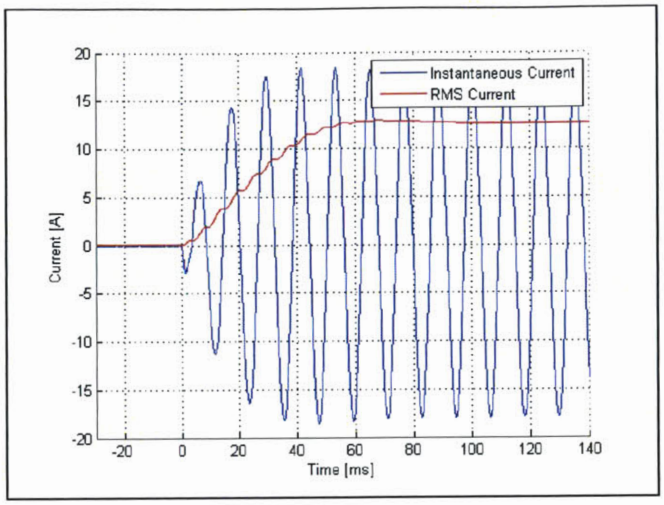

Figure 2-3: RINGS Response to 60 % DC Input Step

From the experimental results shown above, it is estimated that the inflection point of the response occurs at $15ms$. From this result, the process reaction curve parameters are:

$$A = 12.45A$$

$$\tau = 40.88ms$$

$$L = 1.9967ms$$

From these parameters we can calculate the regulator parameters suggested by Ziegler and Nichols:

$$R = \frac{A}{\tau} = \frac{12.45}{40.88} = 0.3045$$

$$K_p = \frac{0.9}{RL} = \frac{0.9}{0.3045 * 1.9967} = 1.4803$$

$$K_t = \frac{0.27}{RL^2} = \frac{0.27}{0.3045 * 1.9967^2} = 0.222$$

2.5 One-Coil Model

A 'One-Coil Model' was developed by Alinger [2] in Simulink to study the behavior without including the back and forward inductance effect. The block diagram in Figure 2-4 shows the different components of the system:

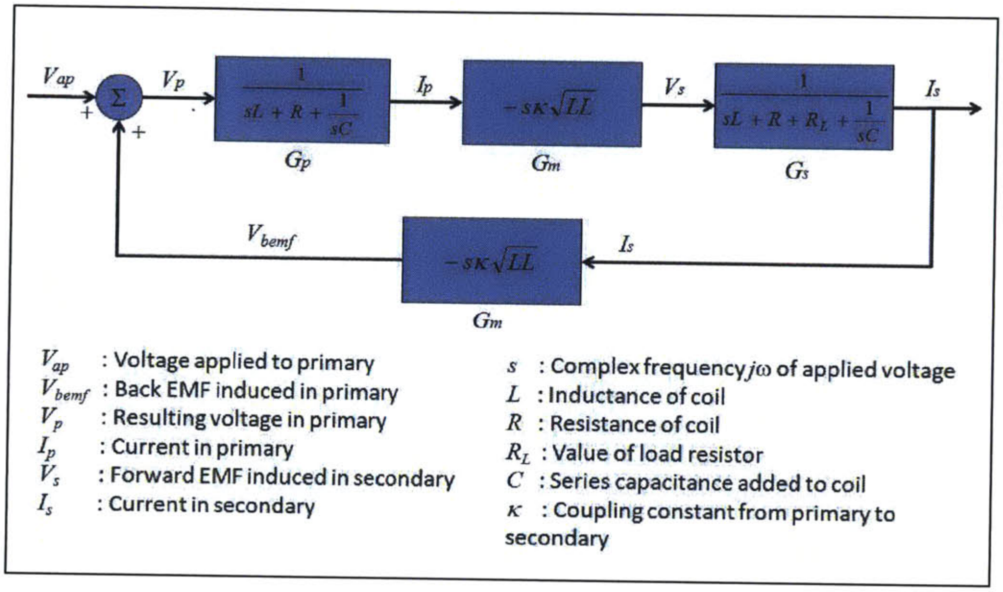

V_{ap}
Σ
+
+
V_p
$\frac{1}{sL + R + \frac{1}{sC}}$
G_p
I_p
$-s\kappa\sqrt{LL}$
G_m
V_s
$\frac{1}{sL + R + R_L + \frac{1}{sC}}$
G_s
I_s
V_{bemf}
$-s\kappa\sqrt{LL}$
G_m
I_s
V_{ap} : Voltage applied to primary
V_{bemf} : Back EMF induced in primary
V_p : Resulting voltage in primary
I_p : Current in primary
V_s : Forward EMF induced in secondary
I_s : Current in secondary
s : Complex frequency $j\omega$ of applied voltage
L : Inductance of coil
R : Resistance of coil
R_L : Value of load resistor
C : Series capacitance added to coil
κ : Coupling constant from primary to secondary

Figure 2-4: 'One-Coil Model' Block Diagram [2]

In order to validate this model, the simulation was driven by the same pair of DC step inputs as above (20% DC and 60% DC) and the results were compared. The circuit parameters used for this simulation are the ones that were obtained experimentally:

$$\begin{aligned} C &= 310uF \\ L &= 11.9mH \\ R &= 1.2\Omega \end{aligned}$$

Figures 2-5 and 2-6 compare the simulation and experimental system response when it is driven with a 20% and 60% DC respectively:

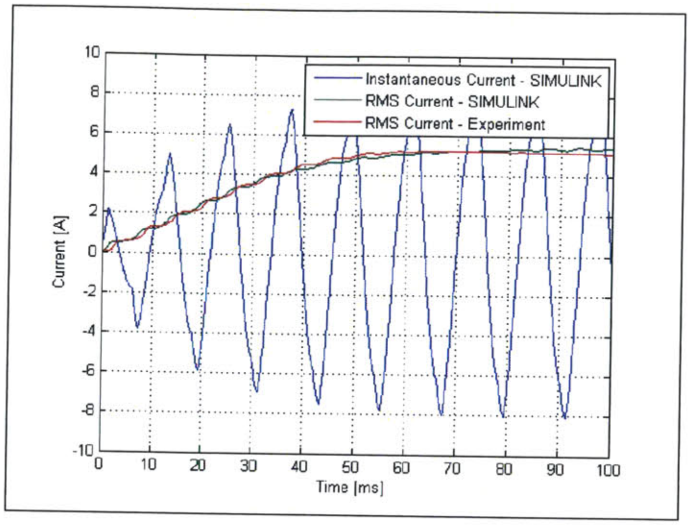

Figure 2-5: One-coil Model vs. Experiment - Response to 20 % DC Step

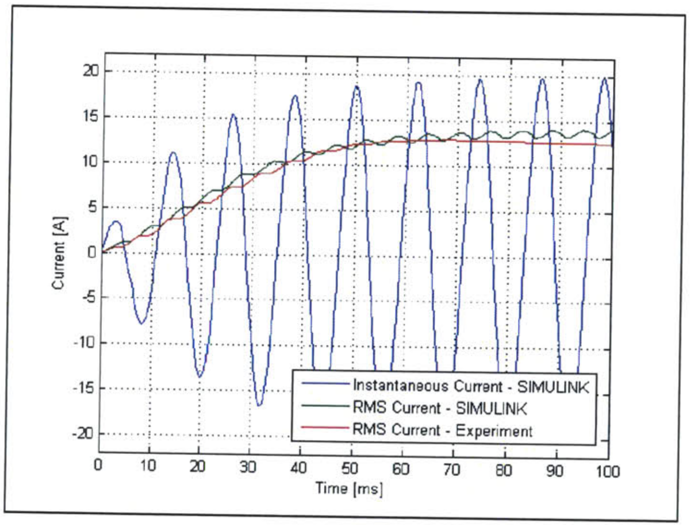

Figure 2-6: One-coil Model vs. Experiment - Response to 60 % DC Step

As it can be seen in the previous figures, the system's output response in the simulation closely matches the one obtained from experimental measurements. The RMS errors are 0.1493A and 0.6954A for the 20% DC and 60% DC step cases respectively. Differences in the output response can be attributed to small differences in the capacitance, resistance and inductance of the coil as well as the battery voltage.

2.6 One-Coil PI Current Controller Model

The 'One-Coil Model' was extended by including a model of the hardware implementation of the PI current controller. The objective of this simulation is to analyze its performance and study the resulting behavior of RINGS. Figure 2-7 is the block diagram of the system which includes the RU coil, the PI controller, and the current sensor:

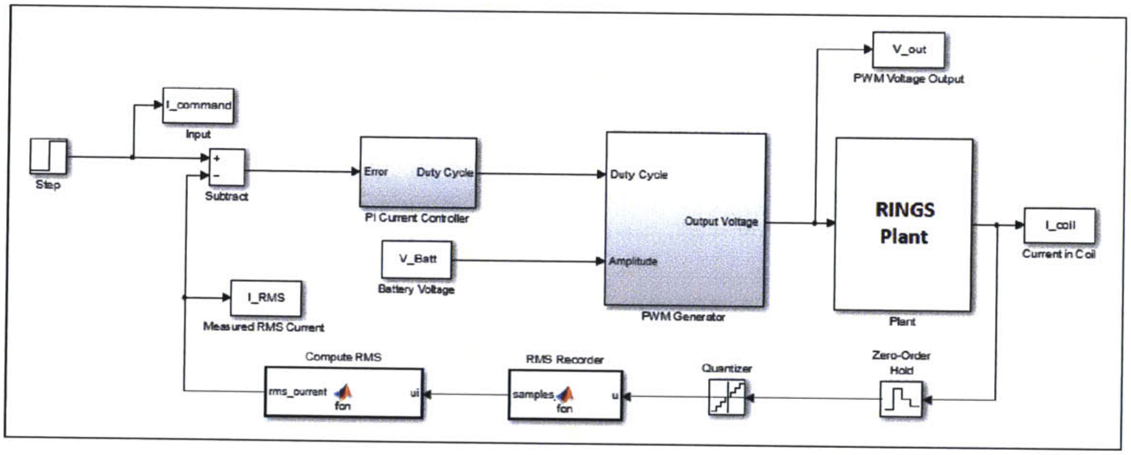

Figure 2-7: PI Current Controller Model Block Diagram

The PI controller and sensor block were modeled to replicate the actual functionality of the RINGS hardware and firmware. The controller implemented in Simulink and in the RINGS firmware has the following characteristics:

1. Sampling Rate: The RU microcontroller reads samples from the Hall Effect Sensor [1] at a rate of 2.49kHz, which is 30 times the EMFF operational frequency (83Hz). As it is explained by Franklin et al.[19], the sampling frequency of a digital controller should be high enough so that the input is sampled at least 6 times during the rise time of the system to an input step. To confirm that this sample rate was high enough, the rise time of the system to an input DC step was used. From the experiments performed in section 2.5 the rise time of the response is approximately $40.6ms$. Thus, the sampling period should be at least

[1] Hall Effect Sensor Part Number: ACS709LLFTR-20BB-T made by Allegro Microsystems

$6.77ms$ or equivalently $150Hz$. The sampling frequency chosen for RINGS was higher than $150Hz$ due to system requirements of the WPT operation mode.

2. Quantization: The RU PIC microcontroller is equipped with a 10-bit Analog-to-Digital converter. This characteristic was incorporated in the model by quantizing the output signal of the HES.

3. Using the last 90 measured current values, the RMS current value is computed and fed back to the PI controller.

4. PWM Generation Module: The RINGS firmware has a resolution of 0.005 to set the duty cycle of the PWM signal. Thus, the output DC of the current controller is converted to the closest value that can be resolved.

The controller gains used in this simulation were the ones found using the 'Ziegler-Nichols' method in Section 2.4. Figure 2-8 compares simulation and experimental results of a step input from 0A to 12A:

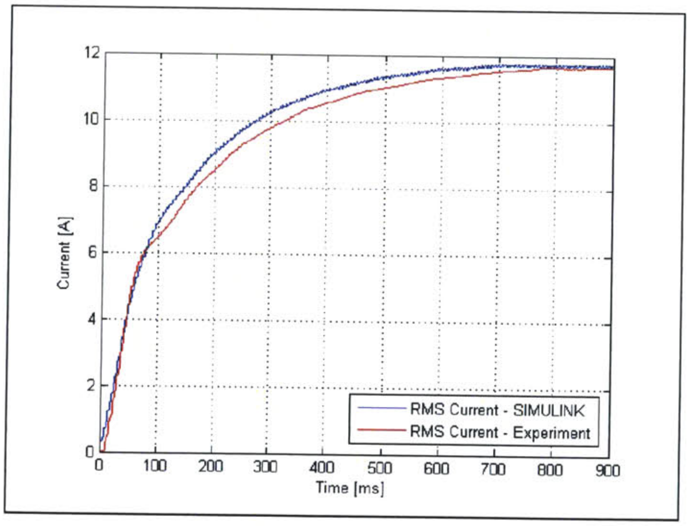

Figure 2-8: One-Coil PI Current Controller Model - System Response to a 12A Step Input

Figure 2-9 shows the response of the system when it is initially driving 12A and a step input of -9A is commanded:

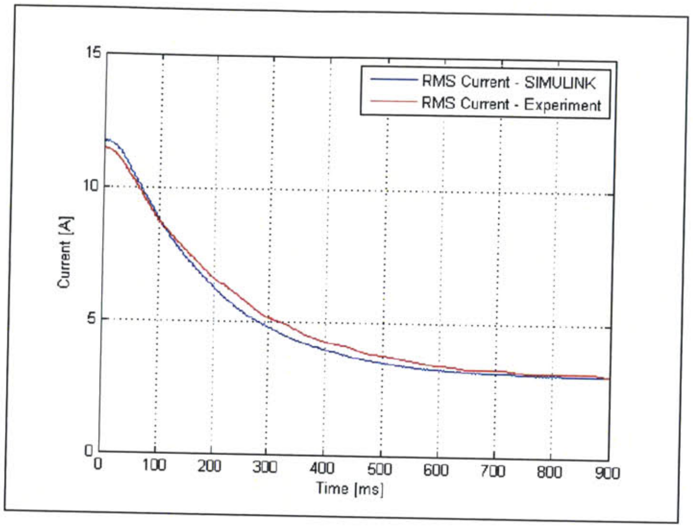

Figure 2-9: One-Coil PI Current Controller Model - System Response to a -9A Input Step

The response of the physical system shows similar characteristics as the response predicted by the simulation. The RMS error of these experiments are 0.3186A and 0.2459A respectively. The system responses show no overshoot and their performance characteristics are:

Rise Time: $t_r = 422ms$

Settling Time: $t_s = 634ms$

2.7 Two-Coil PI Current Controller Model

The 'Two-Coil Model' developed by Alinger [2] was extended to analyze the stability of the PI current controller when the two RUs are at a distance of 2 to 3 coil radii from each other. Figure 2-10 shows a block diagram of the 'Two-Coil PI Current Controller Model':

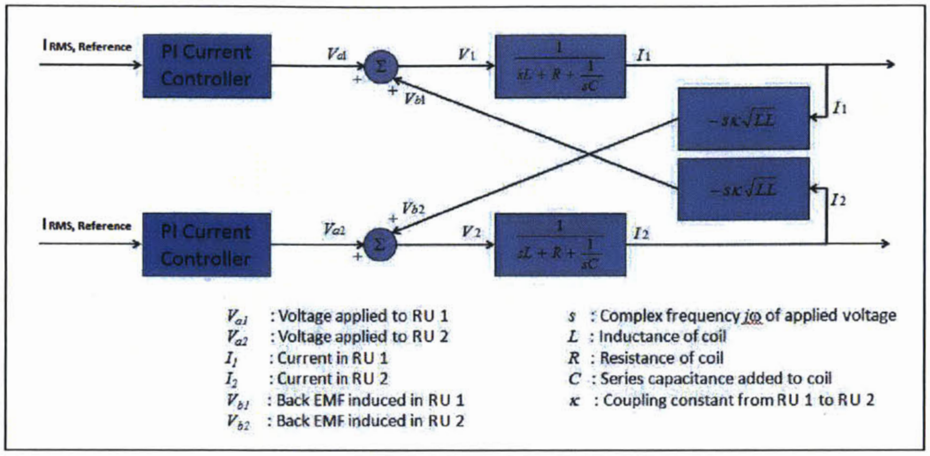
I RMS, Reference
PI Current Controller
V_{a1}
+
V_1
$\frac{1}{sL + R + \frac{1}{sC}}$
I_1
+ V_{b1}
$-s\kappa\sqrt{LL}$
I_1
$-s\kappa\sqrt{LL}$
I_2
I RMS, Reference
PI Current Controller
V_{a2}
+ V_{b2}
+
V_2
$\frac{1}{sL + R + \frac{1}{sC}}$
I_2
V_{a1} : Voltage applied to RU 1
V_{a2} : Voltage applied to RU 2
I_1 : Current in RU 1
I_2 : Current in RU 2
V_{b1} : Back EMF induced in RU 1
V_{b2} : Back EMF induced in RU 2
s : Complex frequency $j\omega$ of applied voltage
L : Inductance of coil
R : Resistance of coil
C : Series capacitance added to coil
κ : Coupling constant from RU 1 to RU 2

Figure 2-10: Two-Coil PI Current Controller - Simulation Block Diagram [2]

As it was explained in section 2.2, the current flowing in the RU coils will induce a back EMF in the other neighboring coil and its magnitude is a function of the coupling coefficient κ. Alinger [2] calculated experimentally the value of this coefficient for the case in which the two RU coil plane normal vectors are co-axial (RUs are facing each other) at a range of 0.2 to 2 meters. An equation of the form:

$$\kappa = (d^a + 1)^b \tag{2.5}$$

is used to fit the experimental data, where d is the separation distance between the two RUs and a and b are the curve fit coefficients. From the experimental data, the values for these coefficients are:

$$\begin{aligned} a &= 0.84 \\ b &= -6.25 \end{aligned}$$

Figure 2-11 plots κ as a function of the RUs' separation distance when they are positioned in the aforementioned configuration:

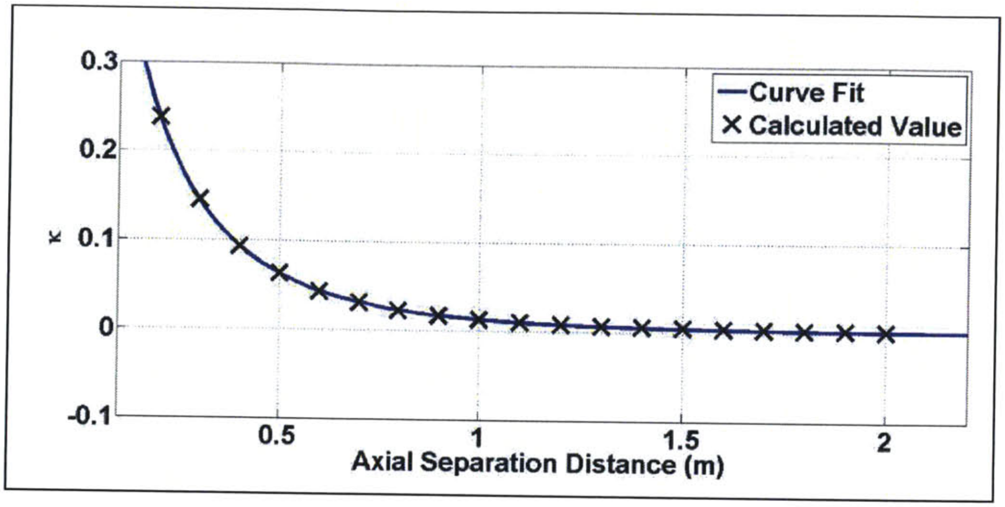

Figure 2-11: Coupling coefficient (κ) vs. Axial Separation Distance [2]

Using the 'Two-Coil PI Controller Model', the stability of the controller is tested under different conditions. As it is shown in Figure 2-12 the two RUs were placed in an axial configuration at a distance of 50 and 75 centimeters from each other. These distances were chosen because they are in the operational range of the RUs aboard the ISS. The following three scenarios were simulated and experimentally tested:

1. Scenario 1: RU 1 was given a 9A input step from 3A to 12A while RU 2 was commanded to keep a constant 12A. The RUs were placed at a distance of $50cm$.

2. Scenario 2: RU 1 was given a -9A input step from 12A to 3A while RU 2 was commanded to keep a constant 12A. The RUs were placed at a distance of $50cm$.

3. Scenario 3: RU 1 was given a 9A input step from 3A to 12A while RU 2 was commanded to keep a constant 12A. The RUs were placed at a distance of $75cm$.

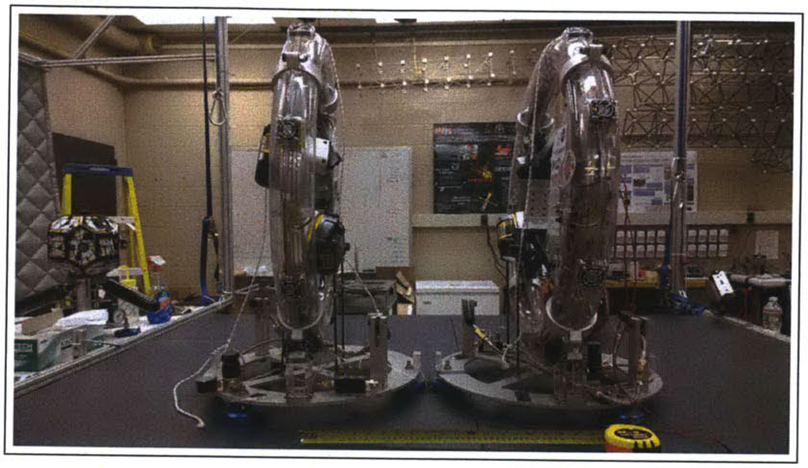

Figure 2-12: Two-Coil Experimental Set-Up

In order to assess the stability of the PI controller, the results from simulation are compared with tests performed using the engineering RUs in the ground testbed. These are shown in Figures 2-13, 2-14 and 2-15:

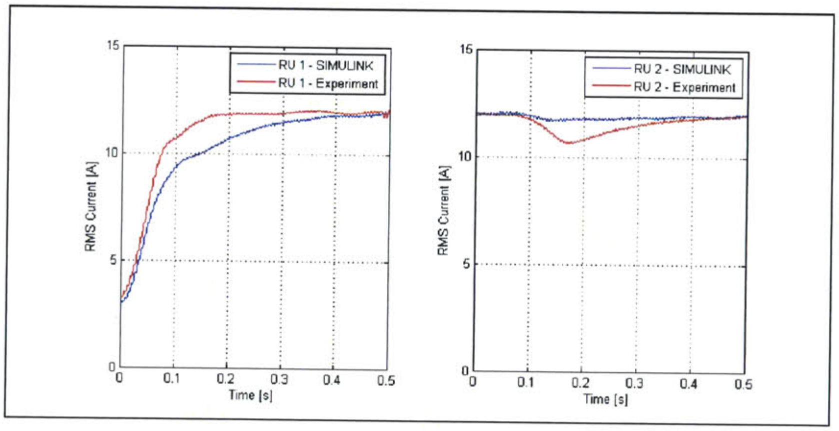

Figure 2-13: Two-Coil PI Current Controller Simulation vs. Experiment - Scenario 1

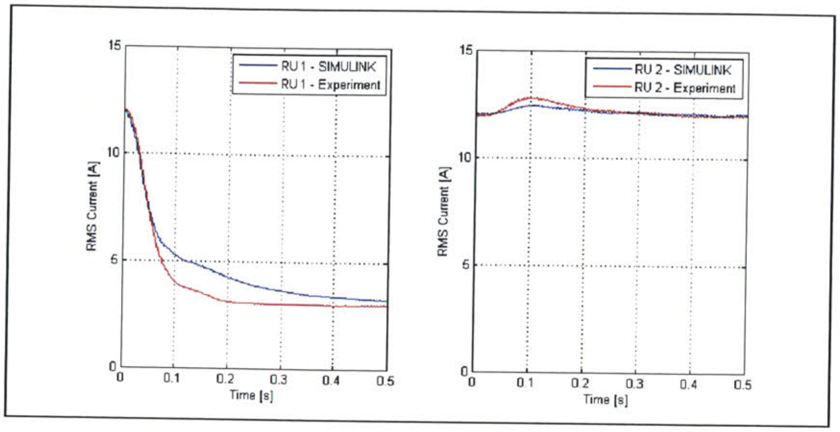

Figure 2-14: Two-Coil PI Current Controller Simulation vs. Experiment - Scenario 2

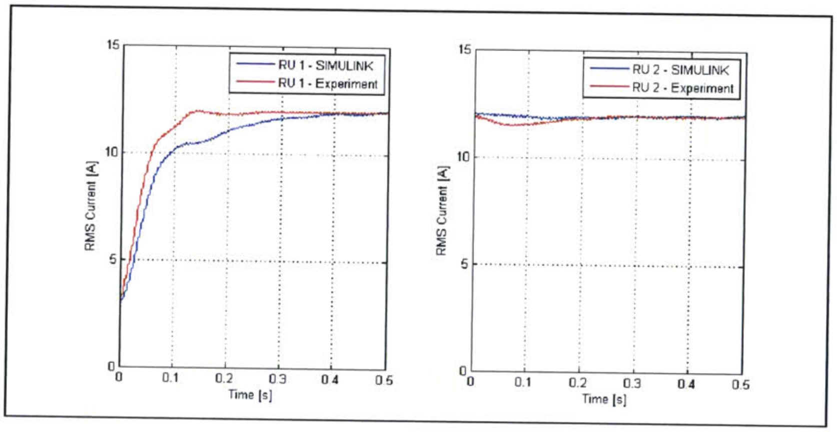

Figure 2-15: Two-Coil PI Current Controller Simulation vs. Experiment - Scenario 3

The responses of the RUs show similar characteristics as the responses predicted by the model. It is observed that the settling time of the response in the experimental cases is lower than the settling time predicted by simulation. In addition, the coupling effect causes greater disturbances in the physical RU coils. Table 2.1 shows the RMS errors for the different scenarios. These discrepancies can be attributed to differences between the RLC circuit parameters used in the simulation and the ones in the engineering RUs' coils. Differences in the set-up used for the calculation of the coupling coefficient might also be a cause of these errors.

Scenario	RMS Error - RU 1 [A]	RMS Error - RU 2 [A]
1	0.8894	0.4706
2	0.7824	0.1612
3	0.8121	0.1854

Table 2.1: Two-Coil PI Current Controller Model vs. Experiment - RMS Error

2.8 Summary

This chapter develops and simulates a PI current controller for RINGS. First, a 'One-Coil PI Controller Model' is validated with an RMS error of 0.32A. Then, the results of the 'Two-Coil PI Controller Model' and experiments show that the PI controller is capable of maintaining a constant RMS current level and correcting for the disturbances created by step commands. Given that the settling time is lower than $0.5s$ and RMS current commands from the SPHERES satellites are given at maximum frequency of $1Hz$, the PI controller can be utilized in RINGS tests.

Chapter 3

SPHERES - RINGS Simulation (SRS)

3.1 Introduction

The SPHERES simulation developed by Katz [5] is a software simulation engine based on MATLAB, Simulink and external C/C++ libraries such as Boost. The simulation intends to provide a high fidelity model of the SPHERES satellites to allow guest scientists to test their control algorithms before implementing them aboard the ISS. The SPHERES-RINGS simulation (SRS) is an extension of the SPHERES simulation that incorporates a model of the RUs and a numerical integration module to simulate the Near-Field EM dynamics. This chapter is organized as follows:

1. Section 3.2: High-level description of the major components of the SPHERES simulation.

2. Section 3.3: Description of the SRS modules and their integration with the SPHERES simulation.

3.2 Description of SPHERES Simulation

The two major features of the current SPHERES simulation are:

1. It can be built entirely into C/C++ code, which provides a great performance improvement with respect to previous versions of SPHERES simulations and it allows for easy distribution.

2. It allows the guest scientist to write the test code for implementation on the hardware and run the same code in the simulation almost interchangeably. (Only few binary flags/constants need to be modified)

Figure 3-1 portrays the test code development process. It is an iterative process in which the guest scientist develops the flight code for testing in the simulation and ground test bed, performs performance analysis on the data collected, and makes modifications or improvements as necessary. Once the flight code performs as expected in both simulation and the ground test bed, it is ready to be uploaded to the ISS and tested during an ISS test session.

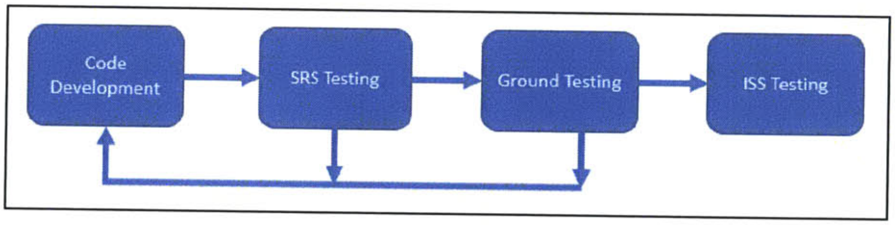

Figure 3-1: SPHERES Test Development Process

Figure 3-2 shows the SPHERES simulation top-level block diagram. The simulation is composed of four major blocks:

1. Global Metrology: Provides timing information that is used by the SPHERES satellites to estimate their position, velocity, attitude and angular velocity within the test volume.

2. Satellites & Payloads: Simulates up to three SPHERES satellites attached to an external payload. Each unit can be enabled or disabled according to the type of test being performed. The external payloads can provide external forces and torques to the SPHERES satellite. Two UART connections exist between the external payload and the units for communication.

3. Termination Conditions: Monitors different error conditions and satellites' parameters. It terminates the simulation if any of the error conditions occurs.

4. Simulation Output: Provides high frequency simulation data/output to external programs for post-simulation analysis. It can optionally be enabled or disabled by the user.

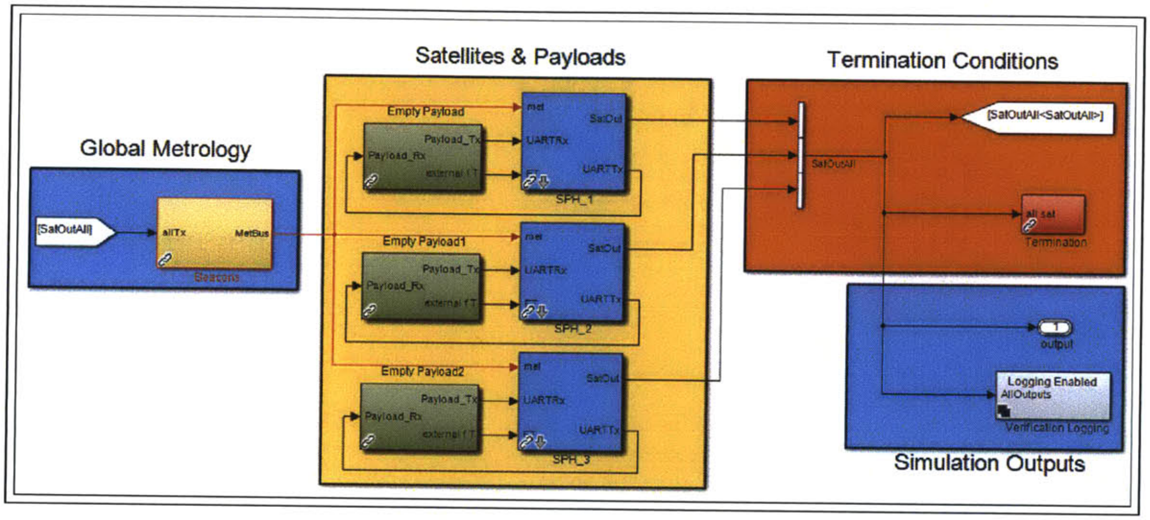

Figure 3-2: SPHERES Simulation Block Diagram [5]

The SPHERES satellite subsystem is composed of three major modules:

1. Dynamic Model: It is programmed in MATLAB and Simulink. The dynamic engine models the SPHERES satellites as a 6-DOF rigid body and includes its 12 thrusters. It runs with a fixed time step of 1 millisecond. The size of the time step was chosen to match the tick frequency of 'SpheresCore,' the operating system of the SPHERES satellites, and it is equal to the fastest frequency at which the thrusters can be commanded. The integration method used by the engine is a 4th order fixed-step Runge-Kutta solver which has an accumulated error of $O(h^4)$.

2. Sensor Model: SPHERES satellites are equipped with gyros, accelerometers and a metrology subsystem based on the reception of US pulses. These sensors are modeled as follows:

(a) Gyros: There are 3 gyros aligned with each of the body axes. The random noise of the sensors is assumed to be zero-mean Gaussian noise and the discretization error in the data acquisition is also captured.

(b) Accelerometers: The model takes into account the rotational coupling between acceleration and angular velocity due to the fact that the sensors are not co-located with the CoM. The measurement noise has two components: a zero-mean Gaussian noise and a high-variance random noise that is caused by a ringing each time a thruster valve opens or closes. This source exponentially decays after this event happens. In addition, discretization error due to the Analog-to-Digital converter (ADC) is also included in the measurement model.

(c) Ultrasound Global Metrology System (USGMS): It allows the SPHERES satellite to compute an estimate of its current state. The state vector includes position in the test volume, velocity, attitude and angular velocity. The USGMS consists of a set of beacons (from 5 to 9 depending on the configuration) that are placed in different corners of the test volume. Each of the beacons possess a unique ID. An IR pulse emitted by the SPHERES satellite triggers the beacons to send back an US pulse after certain amount of time depending on their ID. The US receivers on the SPHERES satellites detect these pulses, and using the Time of Flight (TOF) information, the SPHERES satellites compute an estimate of their state. The noise model of the USGMS includes random measurement losses, receiver and transmitter biases, distance bias and random noise.

3. SPHERES Software Simulation: SPHERES satellites are equipped with a Texas Instruments TMSC6701A Digital Signal Processor (DSP). For performance reasons, a model of the operating system (OS) running on the DSP was created to model the execution of the SPHERES software. The model implements basic OS services such as threads, interrupts and synchronization constructs.

3.3 Description and Integration of RINGS Simulation

The SPHERES - RINGS simulation is an extension of the SPHERES simulation that models the behavior of the RINGS due to the generated EM forces. Figure 3-3 is a block diagram of the SRS. As it can be observed, even though each RU is physically attached to a SPHERES satellite, both RUs are modeled inside a single external payload block. The RINGS payload block has the following input ports:

1. States of SPHERES satellites 1 & 2 (<SatOutAll>): Contains the state of both SPHERES satellites: position, velocity, attitude and angular velocity.

2. UART RX channels from SPHERES 1 & 2: These connections are highlighted in red and named <Payload_Rx1> and <Payload_Rx2> respectively. These channels are used to send data from the SPHERES satellite to the RU micro-controller. Note that these connections should be made by the user to establish a serial connection between the SPHERES satellite and any external payload.

The RINGS block models the dynamics of the RUs by including a numerical integrator block known as the 'Near-Field EM Physics Model' that outputs the generated EM forces and torques. The outputs of the RINGS block are:

1. EM Forces and Torques for SPHERES satellite 1 & 2 (<FT1> & <FT2>): These signals contain the generated EM forces and torques (in the SPHERES body axes) and are fed back to the SPHERES satellites as external forces and torques.

2. UART TX channels to SPHERES 1 & 2 (<Payload_Tx1> & <Payload_Tx2>): These channels are used to send data from the RU micro-controller to the SPHERES satellite.

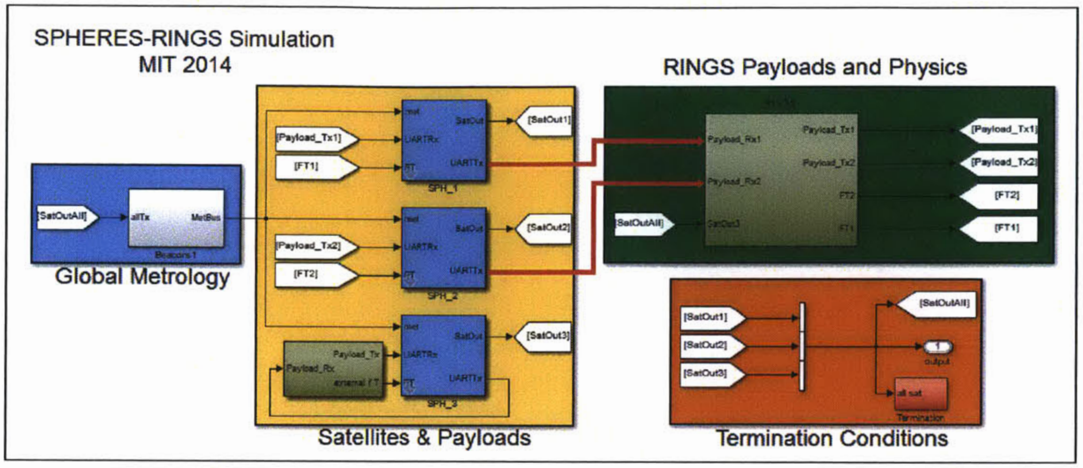

Figure 3-3: SRS Block Diagram

The reasoning behind using a single external payload block is that the 'Near-Field EM Physics Model' block couples the state of the two RUs. An alternative design could have been to model each RU as a separate block and place the 'EM Physics Model' as an extra external block that incorporates the RUs' state and the RUs' coil current as inputs. However, this design had a more complex signal interconnection and did not render any advantage with respect to the current design.

Figures 3-4, 3-5 and 3-6 show the different components inside the RINGS block. The RINGS block has four major modules:

1. RINGS Units (RUs): Each sub-block models a single RU. The input to these blocks are the UART channels from the SPHERES satellites and a set of simulation tuning parameters which are explained in Section 4.5. The output of these blocks are the UART channels to the SPHERES satellites `<Payload_Tx>` and the instantaneous electrical current flowing through the RU RLC circuit `<Electrical Current>`.

2. Near-Field EM Physics Model: This block contains the numerical routines in 'C' that compute the generated EM forces and torques acting on the RUs using equations 1.2 and 1.3. These equations show that EM forces and torques are a function of the relative position and attitude of the RUs and the instantaneous current that is flowing through the RLC circuit of the RUs. Thus, all these

variables are inputs to this block. At each time step of the simulation, the calculated forces and torques are fed back to the SPHERES satellites' dynamic engine (not shown in diagram). In addition, forces and torques in the inertial frame are outputted but only used for analysis and debug purposes.

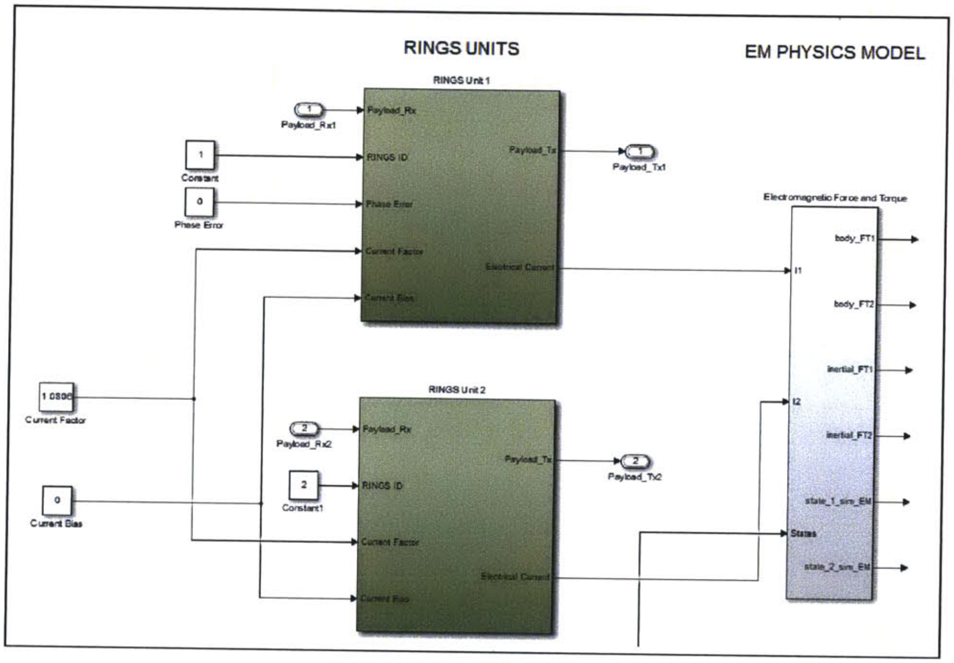

Figure 3-4: SRS Block Diagram - RINGS Units & EM Physics Model

3. State Input: This block allows the user to choose the source from which the 'EM Physics Model' is fed. For debugging and testing purposes, the user is allowed to specify a `.mat` file containing predetermined time-series of the state of the SPHERES satellite. As an example, in Figure 3-5 the source of the position of SPHERES satellite 1 (`<pos>`) is the file named `state_1_force_y.mat` while the other components of the satellite's state (`<vel>, <quat>, <omega>`) are taken from the SPHERES simulation dynamic engine `<SatOut3>`. All these signals are concatenated into the `<States>` signal which is an input to the 'Near-Field EM Physics Model'. The user can change these sources by rewiring the appropriate signals.

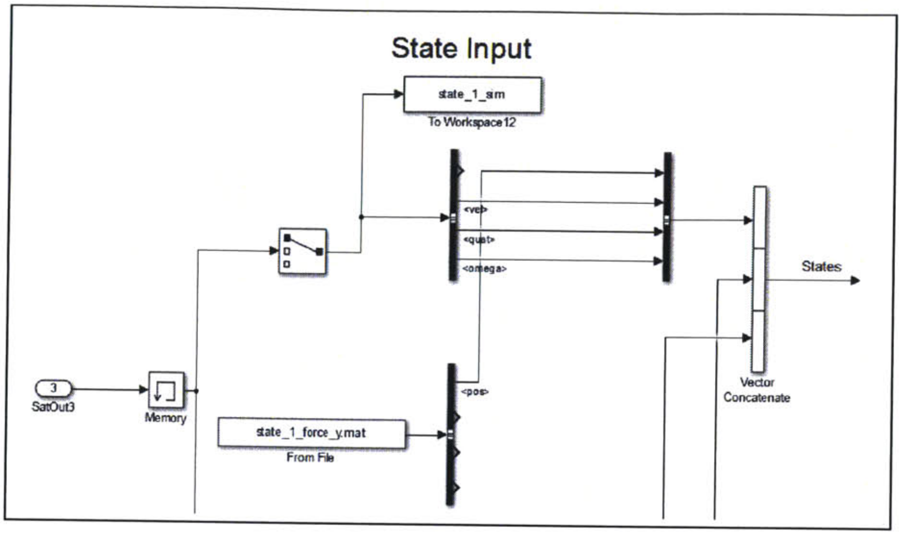

Figure 3-5: SRS Block Diagram - State Input

4. Output Variables: As shown in Figure 3-6 simulation variables are saved in the MATLAB workspace using 'To Workspace' Simulink blocks.

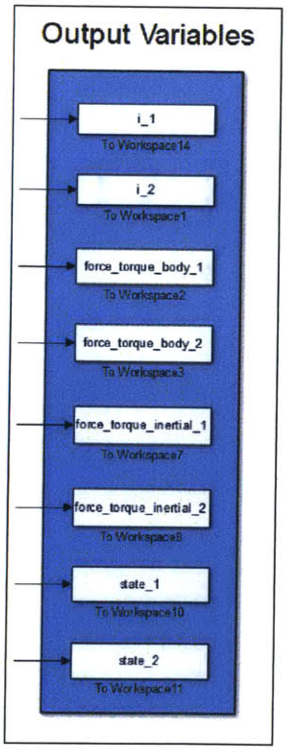

Figure 3-6: SRS Block Diagram - Output Variables

Table 3.1 contains a description of the variables that are currently sent to the MATLAB Workspace:

Variable Name	Description
state_1	RU 1 State
state_2	RU 2 State
i_1 [A]	RU 1 Instantaneous Current
i_2 [A]	RU 2 Instantaneous Current
force_torque_body_1	Force & Torque on RU 1 in Body Frame
force_torque_body_2	Force & Torque on RU 2 in Body Frame
force_torque_inertial_1	Force & Torque on RU 1 in Inertial Frame
force_torque_inertial_2	Force & Torque on RU 2 in Inertial Frame

Table 3.1: SRS Output Variables

The following sections provide a description of the different sub-modules of the SRS.

3.3.1 RINGS Units Firmware & SPHERES - RINGS Communication

The firmware of the RUs was modeled using MATLAB functions executing at the same frequency as in the RUs micro-controller. It receives commands from the SPHERES satellites to set the configuration mode and the RMS current level flowing through the RLC circuit. The SPHERES satellites are equipped with two UART ports that can be used to communicate with external payloads. RUs use one of these serial communication ports to receive commands from the SPHERES satellites and send acknowledgement messages and telemetry data back. (See Appendix A for a description of the SPHERES - RINGS Interface and RINGS API)

The SPHERES simulation provides the two UART ports as an output signal of the SPHERES satellite (<UARTTx>) and are connected to the payload as input ports. Given that the RINGS firmware is modeled with MATLAB functions, it was necessary to create a mechanism to receive and to send bytes from the serial port, mimicking the micro-controller's UART module. Embedded in a MATLAB function a Receive (RX) and a Transmit (TX) buffer were created along with read / write pointers for each of them. Figure 3-7 shows how pointers are manipulated when a read and a write operation occurs:

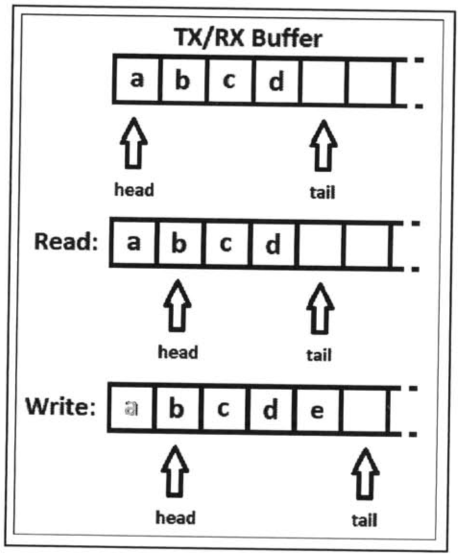

Figure 3-7: RINGS Communication Buffer

As an example, when byte 'e' is received, it is written into the RX buffer and the tail pointer is moved forward. The MATLAB function executes periodically and reads all the bytes pointing from the 'head' until the 'tail'. Once the bytes are received, they are parsed into packets. Appendix B contains the source code of a MATLAB function that can be used for any payload that communicates with the SPHERES satellite through the UART channel. This function should be executed at a frequency of $1kHz$.

3.3.2 RINGS PI Current Controller

Initially, the current controller that was developed in Chapter 2 was intended to be included as a sub-module in the RINGS block. However, this was not possible due to the fact that the SPHERES - RINGS simulation runs at a fixed-size step of 1 millisecond, and the integration step needs to be smaller to generate the PWM signal with the required resolution. Thus, in order to simulate the dynamics of the RLC circuit, the commanded RMS current was passed through a low-pass filter and then fed as an 'envelope' to a sine wave of the commanded frequency. Figure 3-8 is a block diagram of how the filtering was implemented in Simulink:

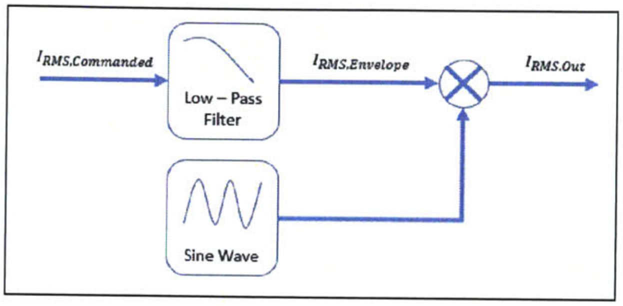

Figure 3-8: RLC Circuit Current with Lowpass Filter

In Figure 3-8, $I_{RMS,Out}$ is the resulting coil current that is fed to the 'Near-Field EM Physics Model'. In order to find the appropriate low-pass filter time constant, experimental data on the system response to a step input described in Section 2.7 was used. Using MATLAB Curve Fitting Tool, it was determined that the low-pass filter time constant should be: $\tau = 0.041s$.

The validity of adding the low-pass filter to simulate the coil dynamics with the addition of the PI controller was tested by simulating an I_{RMS} input step from 3A to 12A. The results of this test are shown in Figure 3-9:

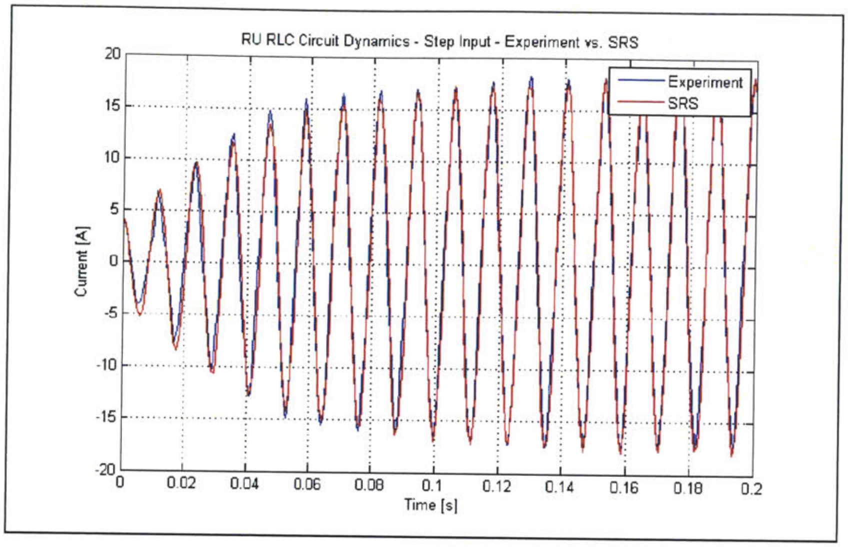

Figure 3-9: RU RLC Circuit Dynamics Test - Experiment vs. SRS

From the figure above, it is observed that the simulated circuit dynamics match the experimental results.

3.3.3 Features Excluded from the SRS

The SPHERES - RINGS simulation doesn't capture the following characteristics of the physical system:

1. RU Temperature: Due to NASA safety requirements, the RU is not allowed to exceed a temperature of $35°C$. If the temperature sensors embedded in the RU detects that this limit has been exceeded, it transitions into a 'Safe Mode' in which the current stops flowing through the RLC circuit. The SRS doesn't take into account the effects that temperature has on the system. Experimental testing has shown that the variation of temperature due to continuous operation increases only by approximately $2°C$ after 8 to 10 minutes of continuous operation. Given that the average length of a RINGS test is 120 seconds, the variation of temperature in a single test is not significant.

2. Low Battery: Given that the duration of RINGS tests is no greater than 180 seconds, it is assumed that the battery voltage will remain constant and won't be

lower than the threshold value. This assumption is valid given that experimental data shows that the battery voltage remains constant for at least 8 minutes when coil current levels are between 7A and 15A.

Chapter 4

SPHERES - RINGS Simulation (SRS) Validation

The RINGS program performed 4 sessions aboard the ISS between August 2013 and July 2014. The first session objective was to perform a hardware checkout of the RINGS to confirm its correct functionality. The objectives of the following three sessions were to perform a mass identification of the system, and to perform open - loop and closed - loop position control tests to support SRS validation.

4.1 SPHERES - RINGS Test Design

Two types of tests were designed to validate the SRS:

1. System Identification Tests (SIT): These tests are used to experimentally determine the center of mass (CoM), inertia properties and thrusters force matrix of each RU. The 'Thrusters Tests' consist of firing SPHERES thrusters sequentially both individually and in pairs. The 'Initial Positioning' tests consist of using thrusters to drive the RU to a target location in the test volume.

2. Electromagnetic Actuation Tests: These tests consist of performing maneuvers using a pre-determined sequence of open-loop current commands. These tests provide data about the EM actuation capability of the RUs in a microgravity

environment. The tests have the following general architecture:

(a) Initial Positioning Phase: The RUs use the SPHERES thrusters to achieve a target initial position and attitude. During this portion of the test the RUs' RLC circuits do not drive current.

(b) EM Actuation Phase: The RUs generate electromagnetic forces through open-loop current commands.

(c) Data Download Phase: SPHERES & RINGS telemetry data recorded during the test is transferred from the SPHERES satellites to the Express Laptop Computer (ELC) controlled by the ISS crew.

In order to simplify the test setup of the RUs and to initially reduce the number of variables needed to be accounted for, the position of one RU inside the test volume was fixed using restraining tethers. Figure 4-1 is a diagram of the RUs in one type of test performed in the ISS. The RU that is in the right side of the picture is tethered to the Deck and Overhead walls of the ISS while the RU on the left side is free-floating.

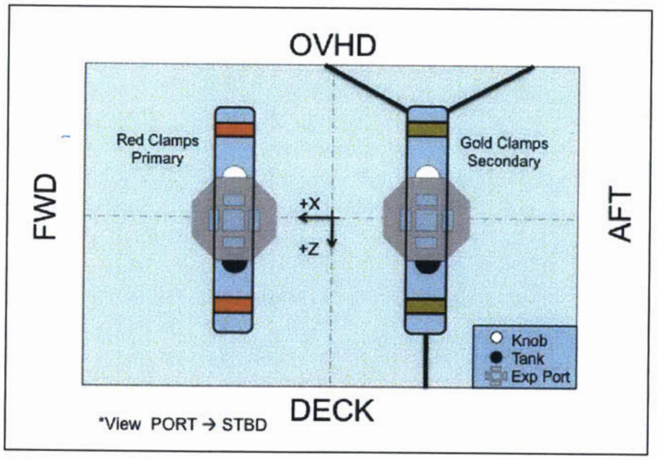

Figure 4-1: RINGS Test Initial Position Set-Up

As explained in Section 1.3.3, when the two RUs' coil plane normal vectors are co-axial and at a distance lower than 7 times their coil radius, the 'Near-Field Model' and 'Far-Field Model' start to diverge by more than 10% (see Figure 1-5). Given that the objective of the tests is to validate the 'Near-Field Model', the RINGS EM actuation should be tested at distances lower than 2.1 meters (RU radius is $0.31m$).

4.2 Coordinate Frames

As a reference for the convention used in this document, Figure 4-2 shows the inertial coordinate frame of the ISS in black and the RINGS body frame in blue. The inertial positive X-axis points towards the FWD wall, the Y-axis towards the Starboard Wall (STBD) and the Z-axis towards the Deck. In the body frame, the X-axis is aligned with the SPHERES expansion port, the Y-axis goes through the face of the RU and the Z-axis completes the right-hand coordinate frame.

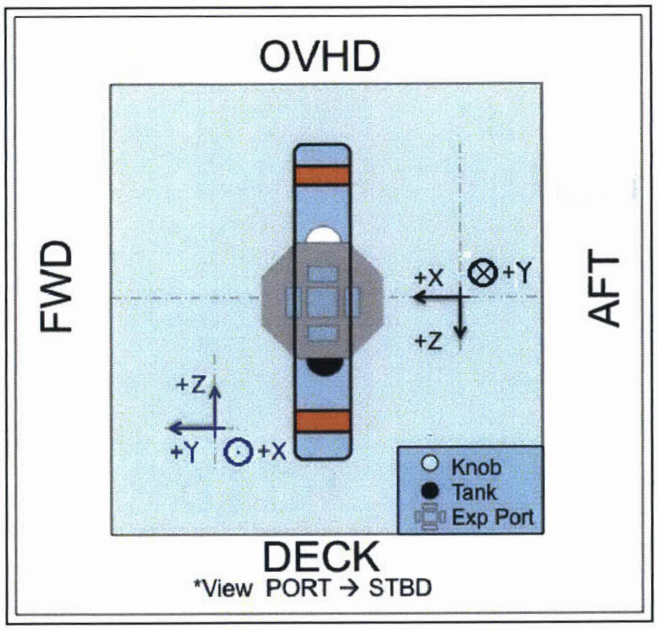

Figure 4-2: Body (blue) & Inertial (black) Reference Frames

4.3 RINGS Physical Parameters Tuning

The objectives of the 'Thrusters Tests' are to determine the location of the CoM, inertia properties and thruster force matrix of the RUs by tuning these parameters in the SRS to match experimental data. These tests consist of firing each SPHERES thruster sequentially for a fixed period of time. In order to obtain more experimental data points, each thruster pulsed 4 times in a row at a frequency of $1Hz$. The test can be visualized in the following timeline:

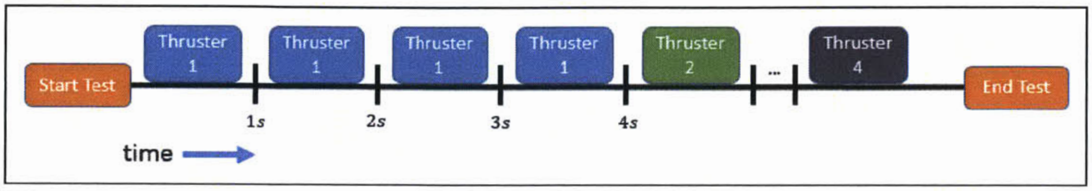

Figure 4-3: Thruster Test Timeline

The length of the firing, amount of time that the thruster was 'ON', was based on the total angle of rotation that was desired to be achieved after 4 thruster pulses and previous estimates the RINGS inertia properties and CoM. Tables 4.1 and 4.2 show the inertia properties and center of mass location estimated by Eslinger [20] from experimental data obtained in the SSL testbed and the RGA flight performed on April 2013. These values were used as a baseline.

Axis	J $[m * s^2]$	Error Bound (95% Confidence Interval)	
X	0.3742	+0.0118	-0.0110
Y	0.924	+0.295	-0.108
Z	0.5577	+0.1377	-0.0922

Table 4.1: SPHERES-RINGS Moment of Inertia - Baseline

Axis	Value [m]	Uncertainty [m]
X	-0.025	±0.005
Z	0.0019	±0.005

Table 4.2: SPHERES-RINGS Center of Mass - Baseline

SPHERES satellites are equipped with three Systron Donner BEI Gyrochip II single-axis rate gyroscopes that are used to measure angular rate. These gyroscopes have a range of measurement of $\pm 83°/s$ and a resolution of $0.0407°/s$. In addition, in order to measure linear acceleration, SPHERES satellites have three Honeywell QA-750 single-axis analog accelerometers. After the digital conversion is performed, these sensors provide a resolution of $1.23 * 10^{-4} m/s^2$. It was desired for the RU to rotate at least 5 degrees so that the motion could be observed by the ISS crew members. Assuming that the CoM is at the geometric center of the SPHERES satellite:

$$\tau = I * \alpha \tag{4.1}$$

$$\alpha = \tau / I_{Baseline} \tag{4.2}$$

$$\begin{bmatrix} \alpha_x \\ \alpha_y \\ \alpha_z \end{bmatrix} = \begin{bmatrix} 0.025 \\ 0.010 \\ 0.017 \end{bmatrix} rad/s^2 \tag{4.3}$$

Given the desired minimum angular rotation of 5 degrees, it was determined that the lower bound for the total firing time needed to be at least 2.4 seconds. Since 4 firings occur per thruster, each firing period was set to $600ms$. The SPHERES code was implemented and tested in the SRS using the baseline moments of inertia listed in Table 4.1.

Initially, the 'Thrusters Tests' were simulated in the SRS and Figure 4-4 shows the results for thrusters 1 through 4 using the baseline parameters listed in Tables 4.1 and 4.2:

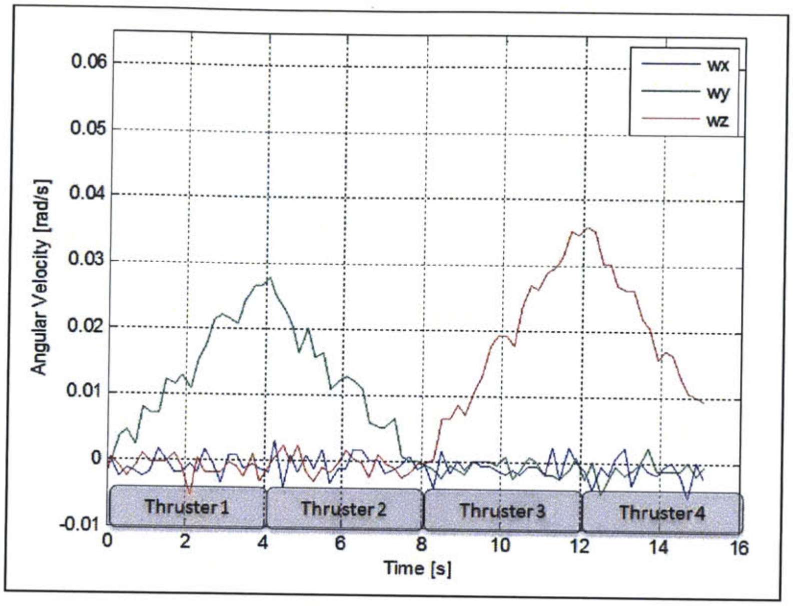

Figure 4-4: RINGS Unit Angular Velocity - SRS Results

As a reference, Table 4.3 shows the torque direction of the twelve SPHERES thrusters:

Thruster	Torque Direction	Thruster	Torque Direction
1	+Y	7	-Y
2	-Y	8	+Y
3	+Z	9	-Z
4	-Z	10	+Z
5	+X	11	-X
6	-X	12	+X

Table 4.3: SPHERES Thrusters Torque Direction

As it is expected, thrusters 1 and 2 produce a positive and negative angular acceleration in the Y-axis respectively (see Table 4.3) while thrusters 3 and 4 act on the Z-axis. The magnitude of the angular velocities observed in the Y-axis are lower than in the Z-axis given the higher inertia in the first axis. These results show that the RU will achieve angular velocities that will be within the range of measurements of the sensors and distinguishable from the sensors noise.

Subsequently, the 'Thrusters Tests' simulated in the SRS were performed in the second RINGS ISS test session. The results are shown in Figure 4-5:

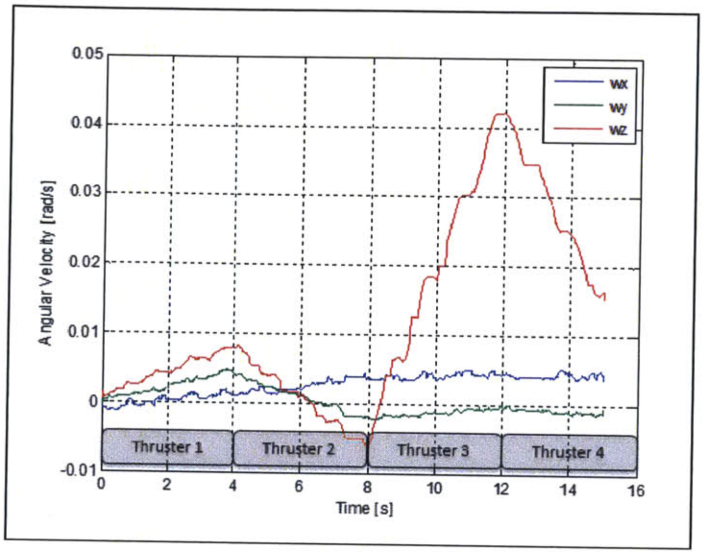

Figure 4-5: RINGS Unit Angular Velocity - ISS

The angular accelerations were estimated from the average slope of the angular velocity. Firing thrusters multiple times was beneficial for data analysis since it is observed that the recorded slopes have some variance associated with noise and variability in the force provided by the SPHERES thrusters.

There are various differences between the predicted SRS results (Figure 4-4) and the experimental data obtained from ISS (Figure 4-5). In the ISS test thrusters 1 and 2 (two of the four thrusters that exert a torque in the $\pm Y$ direction) produce a much more reduced angular acceleration than the one predicted by the SRS. While the SRS predicts a maximum angular velocity of $0.03 rad/s$, ISS results show that the maximum angular velocity was only $0.004 rad/s$, one order of magnitude lower. This reduction in thruster capability is due to the fact that the aforementioned thrusters are impinged by the RINGS hardware. In addition, it can be observed that when thrusters 1 and 2 are fired there is also a noticeable angular acceleration in the Z-axis and the X-axis. This behavior can be attributed to the jet being deflected in the Z and X directions after hitting the batteries or the RUs housing. Figure 4-6 shows how thrusters 1 and 2 direct plume towards the batteries while thrusters 7 and 8 are blocked by the RU housing.

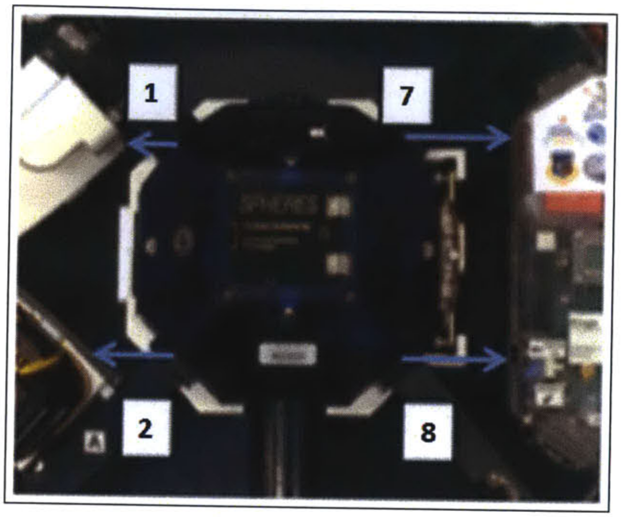

Figure 4-6: SPHERES-RINGS Thrusters Impingement

The thrusters impingement creates a higher uncertainty in the data recorded resulting in broader confidence intervals for the inertia values. An accurate measure of the inertia about the Y-axis is not as important as in the other two dimensions since rotating the RU about the Y-axis doesn't change the EM dynamics. However, the reduced actuation capability may be of importance if translation using thrusters in the X direction is required.

Combining the measurements from the gyros and accelerometers recorded during the ISS thrusters tests, Hilton's analysis [21], which is based on a least-square method, determined that the RU tensor of inertia, CoM and thruster force matrix are:

Axis	J $[m * s^2]$
X	0.3491
Y	0.7555
Z	0.4247

Table 4.4: SPHERES-RINGS Moment of Inertia - ISS

Axis	Position $[m]$
X	-0.01245
Y	0.00633
Z	0.00160

Table 4.5: SPHERES-RINGS Center of Mass - ISS

Thruster	Force X $[N]$	Force Y $[N]$	Force Z $[N]$
1	0.011	-0.001	0.003
2	0.022	0.012	-0.004
3	0.013	0.104	0.000
4	0.005	0.077	0.001
5	-0.002	-0.008	0.077
6	-0.002	0.004	0.091
7	-0.008	-0.013	0.009
8	-0.012	-0.004	-0.003
9	0.008	-0.056	-0.004
10	-0.010	-0.066	0.002
11	0.002	0.017	-0.072
12	0.001	-0.023	-0.095

Table 4.6: SPHERES-RINGS Thrusters Force Matrix - ISS

The 'Thruster Tests' were again simulated using the new physical parameters obtained by Hilton [21]. Figure 4-7 compares the gyro data recorded in the ISS with the simulated results and Figure 4-8 compares Y-axis accelerometer data when one of the thrusters is fired:

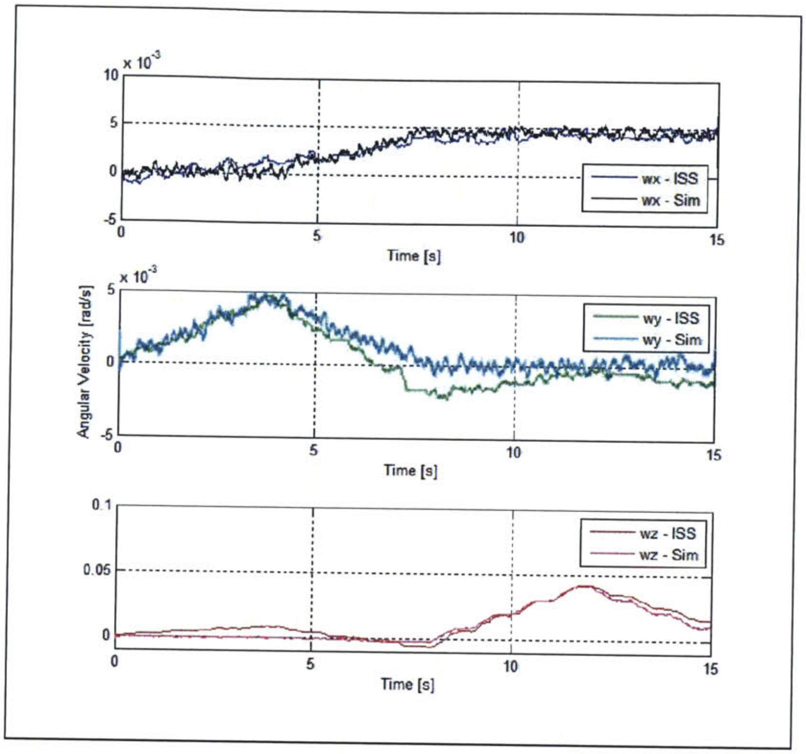

Figure 4-7: Gyro Readings - ISS vs. SRS

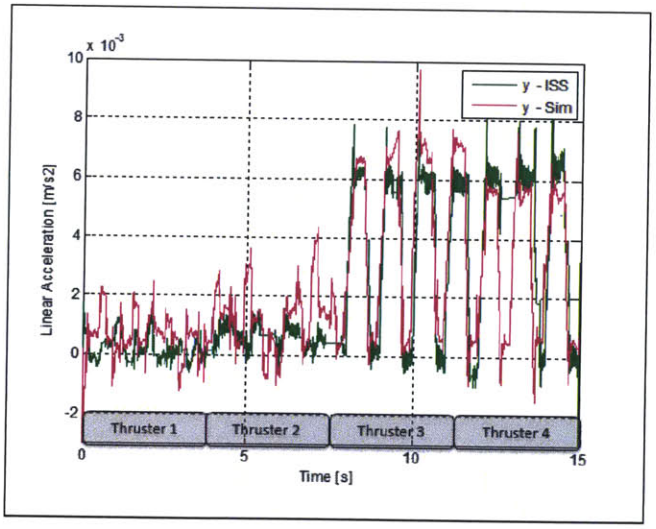

Figure 4-8: Y-Axis Accelerometer Readings - ISS vs. SRS

The maximum percentage difference in angular velocities and linear accelerations between the SRS and the ISS experiments is below 15%. The observed positive and negative angular accelerations in the Z-axis (Figure 4-7) when thrusters 1 and 2 fire in the ISS are due to the thruster jet producing a torque when being deflected by the battery packs (Figure 4-6). This phenomenon is not currently modeled in the SRS due to the increased complexity and lack of data for validation. However, it is considered that the effects on the control and simulation outputs are negligible.

4.4 RINGS Physical Parameters Validation

The second step in the validation process of the RINGS physical parameters is to compare the SPHERES position and attitude recorded during the 'Initial Positioning' phase of the tests in the ISS with the SRS results.

As it is explained in Section 4.1, during this phase the RUs use only thrusters to navigate to an initial target position and hold that position before they transition to the 'EM Actuation Phase'. A PD control law was used for position and attitude control. This controller was employed under the assumption that the starting position of RU (place at which the ISS crew member deploys the unit) would be near the desired initial position and that the attitude error would also be small.

In order to choose the controller gains, the RU was modeled as a double-integrator plant:

$$G = \frac{1}{ms^2} \tag{4.4}$$

The resulting gains and performance characteristics of the response are given in tables 4.7 and 4.8 respectively:

Position Controller Gains	Value
Kp	0.15098
Kd	2.8418
Attitude Controller Gains	Value
$K_{p,x}$	0.0028408
$K_{d,x}$	0.059696
$K_{p,y}$	0.0055598
$K_{d,y}$	0.11473
$K_{p,z}$	0.0042339
$K_{d,z}$	0.08897

Table 4.7: RINGS PD Controller Gains for Initial Positioning

Response Parameter	Value
Overshoot	15.9%
Rise Time	$8.15s$
Settling Time	$54.9s$

Table 4.8: System Response Characteristics

The 'Initial Positioning' phase was simulated in the SRS and compared to the results obtained in the ISS tests. In this particular test, the RU 1 (free-floating unit) target position and attitude are:

Target Position	Value [m]
X	+1m from RU 2 X-Position
Y	0.0
Z	0.0
Target Attitude	Value [degrees]
Yaw	-90
Pitch	0
Roll	180

Table 4.9: 'Initial Positioning' Phase - RU 1 Target Position and Attitude

Figures 4-9 and 4-10 show the results for position and attitude of RU 1 during the 'Initial Positioning' phase. In addition, Figure 4-11 shows the error in position and attitude between the SRS and ISS tests.

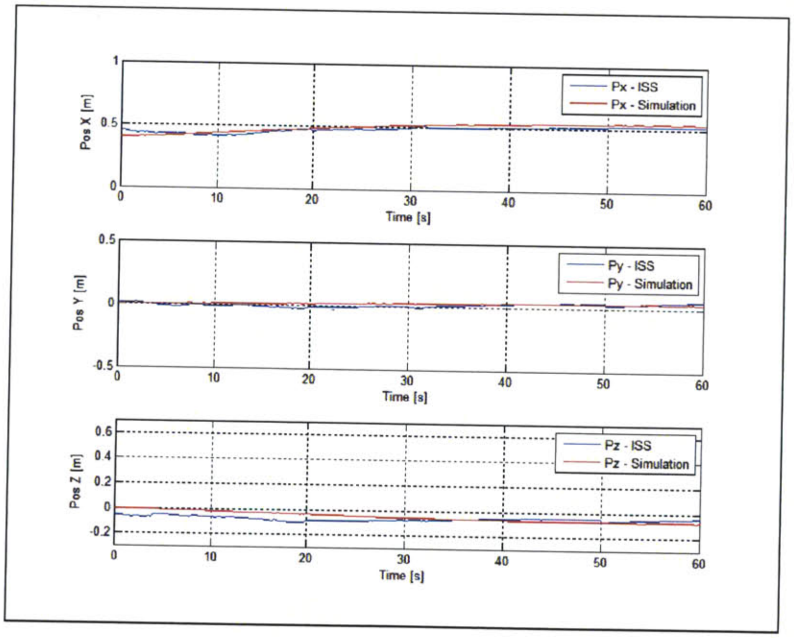

Figure 4-9: RU 1 Position - ISS Test vs. SRS

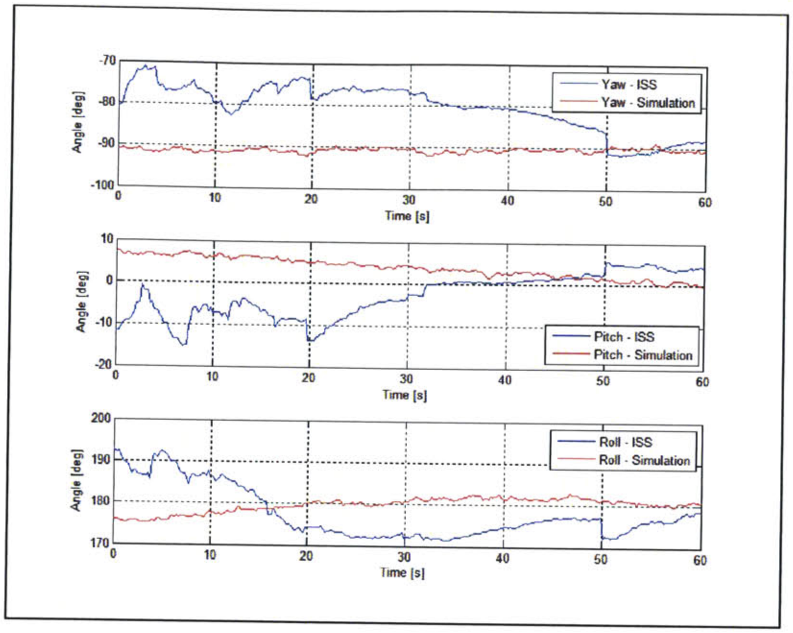

Figure 4-10: RU 1 Attitude - ISS Test vs. SRS

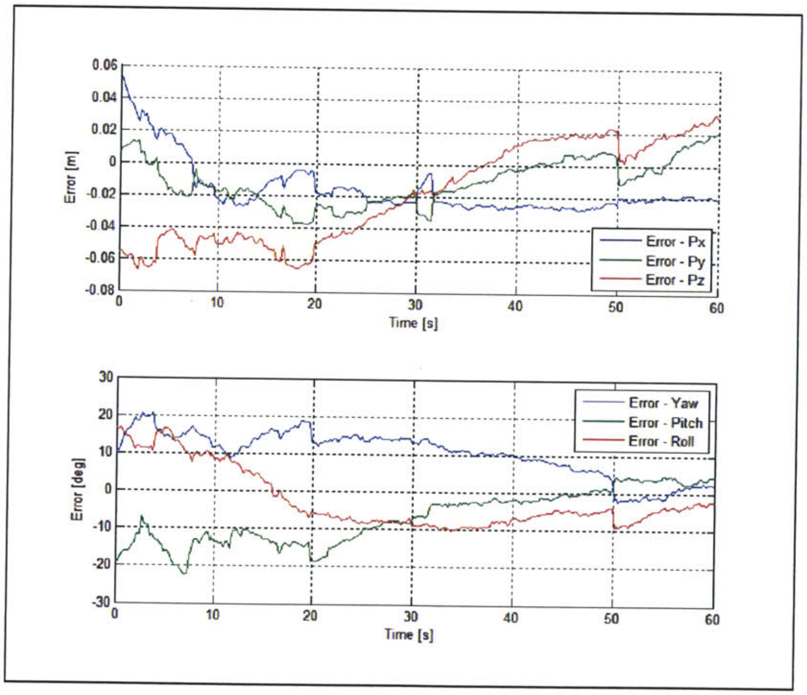

Figure 4-11: RU 1 Position and Attitude Error - ISS Test vs. SRS

During the 'Initial Positioning' phase, RU 1 (free-floating unit) is commanded to a position one meter apart from RU 2 (tethered unit) in the X-axis. From the metrology system data received from ISS, it was determined that the RU 2 was tethered at coordinates $(-0.4m, 0m, 0m)$. Thus, as shown in Figure 4-9, RU 1 navigates to coordinates $(0.6m, 0m, 0m)$.

In Figure 4-11 it is shown that at the end of the 'Initial Positioning' phase $(t = 60s)$ the error in the X-axis is $2cm$. This error is due to the fact that RU 2 is not rigidly tethered and is still able to move up to $10cm$ in the X-axis (see Section 4.5). Thus, the target X-position of RU 1 varies few centimeters as it receives the updated state from RU 2. The errors in the Y-axis and Z-axis can be explained by the fact that the actuation in the Y-direction was limited due to impingement and the coupling effect on the thrusters.

In order to assess attitude error, quaternions are used to compute the quaternion error relative to the desired attitude. Figure 4-11 shows the Euler angle rotations in the SPHERES body frame that are derived from the error quaternions thereby providing an intuitive understanding of attitude error. The quaternion values are converted to 'Euler Angles' using a 321-rotation. These results show that the controller attempts to correct for the error in all three axes and the final error is below 2.5 degrees. The source of these errors can be attributed to two main factors: (1) the coupling effect of the thrusters that the RU controller does not account for and (2) the presence of noise in the estimator. In other instances of equivalent tests, the final error in the Z-axis is higher than 3 degrees due to the large amount of error that the controller needs to correct. In order to mitigate this error, a more aggressive controller would need to be designed that had a lower settling time. Given that the 'EM Actuation Phase' follows the 'Initial Positioning' phase, it is important that the RU achieves the desired position and attitude during this phase. For the tests that involved EM attraction, small errors in the RU attitude did not cause the system to become unstable. Given the small differences observed between the ISS experimental results and the SRS, it is determined that the 'Initial Positioning' phase in the SRS is validated with a maximum error of $3cm$ for position and 3 degrees for attitude.

4.5 EM Force Validation

'Electromagnetic Actuation Tests' focused on gathering data about the EM actuation capability of the RUs in a microgravity environment. As it is described in Section 4.1, the RUs start by positioning themselves at a fixed distance from each other using thrusters only. After the desired initial positioning is achieved, the 'EM Actuation Phase' starts. For these tests, a predetermined current profile was used and is shown in Figure 4-12. The shape, magnitude and phase of the current profile was driven by the following factors:

1. EM actuation should produce a displacement of the RUs large enough to be measured by the SPHERES estimator.
2. Current profile should prevent RUs from colliding with each other or make them exit the test volume.

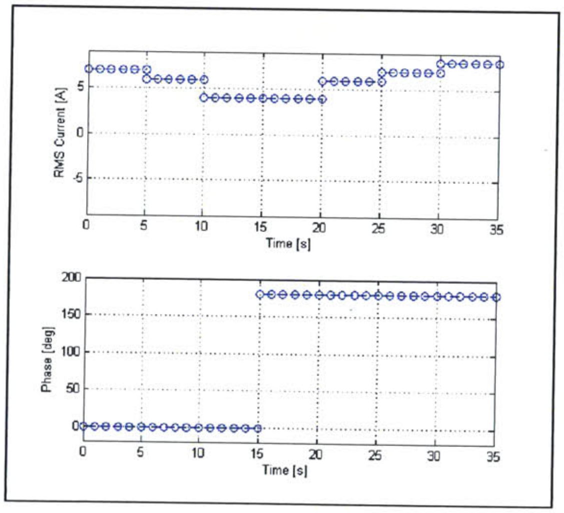

Figure 4-12: EM Actuation Test - Current Profile

Initially, this test was designed to validate both EM attraction and repulsion. Thus, the current profile in Figure 4-12 drives the RUs current in-phase (attraction force) for the first 20 seconds and 180 degrees out-of-phase (repulsion force) for the last 15 seconds. However, for reasons explained in Section 4.6, the data gathered in these tests could only be used to validate EM attraction.

Given that closed-loop control with thrusters had not been demonstrated on ISS for the RINGS hardware, three different types of tests were designed where thruster actuation was responsible for a different number of DOF during the 'EM Actuation Phase'. Table 4.10 describes the actuation on all 6 DOF for each type of test:

Test Type	X Translation	Y Translation	Z Translation	X Rotation	Y Rotation	Z Rotation
1	EM	None	None	None	None	None
2	EM	Thrusters	Thrusters	Thrusters	Thrusters	Thrusters
3	EM	None	None	Thrusters	Thrusters	Thrusters

Table 4.10: Thruster Actuation in 6 DOF

Translation in the X-direction is achieved by EM forces generated by the RINGS. In type 1 tests, no thruster are fired during the 'EM phase'. In type 2 tests, thrusters are used to hold the axial configuration [1] in the 5 DOF so that the coils can more effectively actuate in the axial direction. Type 3 tests were designed to assess the actuation capability when the thrusters are only allowed to control torque. If the thruster control proved ineffective during the ISS session, only Type 1 tests would have been used for the rest of the session so that data on EM actuation could still be gathered. Since it was observed that closed-loop thruster control was effective in the 'Initial Positioning' phase, tests of type 2 and 3 were performed. These last two types of tests could prove the feasibility of EMFF with coils and reaction wheels as actuators.

As explained earlier, RU 2 is tethered to the Deck and Overhead of the ISS during the tests. However, Figures 4-13 and 4-14 show that the RU is still able to move up to 15cm in the X-direction and 25cm in the Z-direction from its initial position. In addition, oscillations in attitude of up to 17 degrees are observed.

[1] Axial Configuration: The RUs' coil plane normal vectors are co-axial (RUs are facing each other)

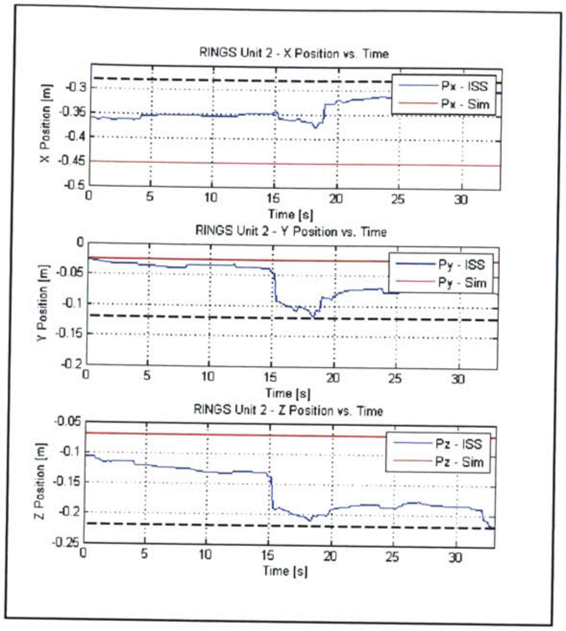

Figure 4-13: EM Actuation Test - RU 2 Position Oscillations

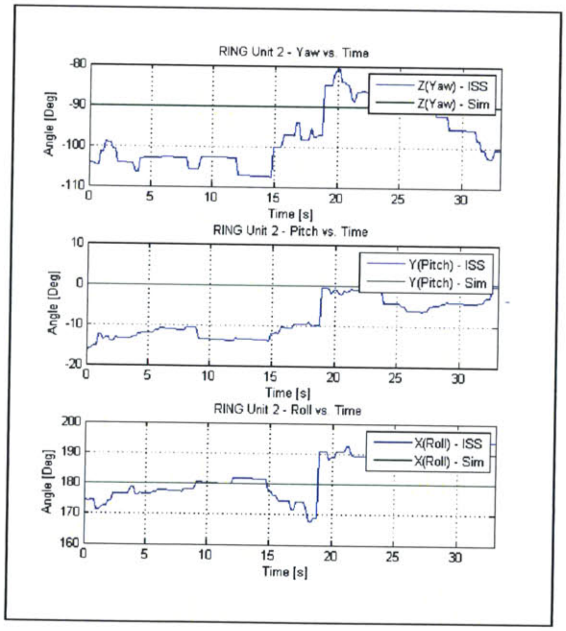

Figure 4-14: EM Actuation Test - RU 2 Attitude Oscillations

Due to these oscillations in position and attitude, modeling RU 2 as being fixed at an initial position is not a valid assumption and it causes large discrepancies in the computation of resulting EM forces and torques in the SRS. Thus, it was decided to validate the simulation by feeding the attitude of RU 1 and both position and attitude of RU 2 from telemetry data obtained during the ISS test. All other state variables of RU 1 are propagated and fed back to the SRS dynamics engine. Figure 4-15 shows a block diagram describing how inputs are fed into the SRS:

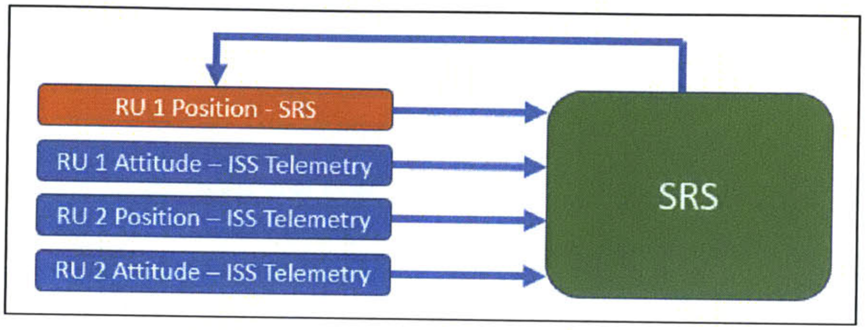
RU 1 Position - SRS
RU 1 Attitude – ISS Telemetry
RU 2 Position – ISS Telemetry
RU 2 Attitude – ISS Telemetry
SRS

Figure 4-15: SRS Validation of Axial EM Tests - Inputs

Figures 4-16 plots the position of RU 1 during the 'EM Phase' of a type 1 test predicted by the SRS and the telemetry data obtained from the ISS. In addition, Figure 4-17 shows the error between these two variables.

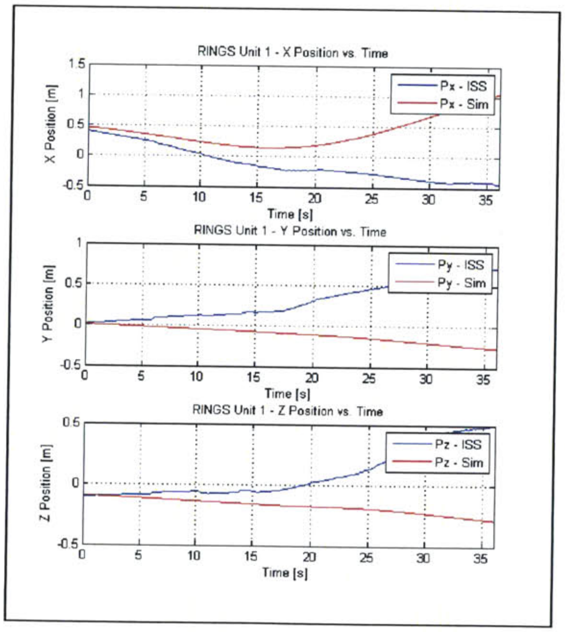

Figure 4-16: Axial EM Type 1 Test - RU 1 Position - ISS Test vs. SRS

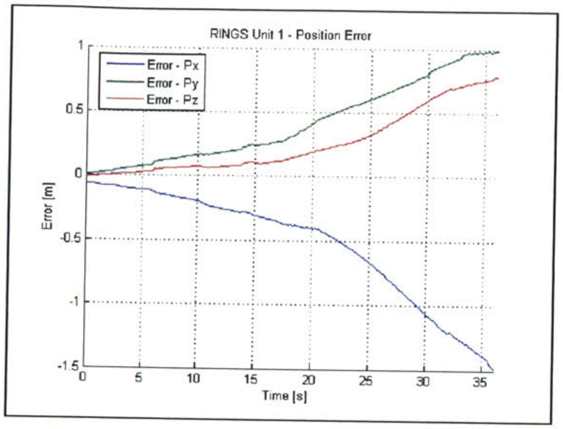

Figure 4-17: Axial EM Type 1 Test - RU 1 Position Error - ISS Test vs. SRS

It is observed in Figure 4-17 that the error in the X-axis, where the strongest EM force occurs, monotonically increases during the 'EM Phase' and it is unbounded. The SRS results clearly diverge from the experimental ISS data: position error in all three axis at the beginning of the 'EM Phase' ($t = 0s$) is less than $2cm$ and at $t = 28s$, the error in the X-axis is approximately $1m$. In Figure 4-16 there are three major discrepancies between the SRS and the ISS test results:

1. During the 'Attraction Phase' (0s to 15s) the SRS underpredicts the EM force that was observed during the ISS test causing RU 1 to move a lower distance.

2. During the 'Repulsion Phase' (15s to 28s) the SRS overestimates the repulsive EM force. It is observed that while in the SRS RU 1 exhibits motion in the negative X-axis, it is hardly noticeable in the ISS test.

3. RU 1 drifts in the positive Y and Z direction even though no thruster is fired in this phase of the test. In addition, EM forces can't produce this drift given that data shows that the unit maintained its axial configuration with an error of less than 15 degrees in all yaw, pitch and roll angles.

In order to explain and correct the observed discrepancies between SRS and ISS experimental data, two major modifications were made to the SRS:

1. Drag Model: The SRS previously did not model drag forces that might be present when operating in the ISS test volume. From data obtained in the ISS

test session 51 for the SPHERES - VERTIGO program, Setterfield's analysis [22] concluded that the airflow inside the test volume in which the RINGS test data was taken is at least 17.5 cm/s. Thus, the SRS was modified to incorporate drag forces in both X, Y, and Z directions using the drag equation:

$$D = \frac{1}{2}\rho(V_{RINGS} - V_{Airflow})^2 C_D A \tag{4.5}$$

The drag model uses a constant value for the velocity of the airflow. Table 4.11 lists the values used for the reference areas, airflow velocities and drag coefficients, which are appropriate for the circular and rectangular shape of the RUs with this Reynold's number.

Parameter	Value
ρ	$1.225\frac{kg}{m^3}$
$C_{D,x}$	1.28
$C_{D,y}$	2.1
$C_{D,z}$	2.1
$V_{Airflow,x}$	16 cm/s
$V_{Airflow,y}$	20 cm/s
$V_{Airflow,z}$	11 cm/s
A_x	$0.27m^2$
A_y	$0.0576m^2$
A_z	$0.0576m^2$

Table 4.11: Drag Model Parameters

2. Current Model: The SRS was modified to allow for parameters related to the RUs' coil current to be tuned. The choice of the parameters was based on the researchers evaluation that a possible cause of the discrepancies was a difference between the current commanded to the RUs and the actual current that circulated in the coils during the experiments. Section 4.6 provides a justification on

why these modifications are valid. The following parameters were chosen:

(a) Current Offset: A constant variation of the current with respect to the commanded RMS current.

(b) Linear Current Bias: A variation that is linearly proportional to the commanded RMS current.

(c) Phase Error: Difference between the commanded and the actual phase shift between the current waves of the two RUs.

Through an iterative process, the values that provided the closest match between SRS results and ISS data were found. These are shown in Table 4.12:

Parameter	Value
Current Offset	0A
Linear Current Bias	1.0806
Phase Error (Attraction Phase)	0 deg
Phase Error (Repulsion Phase)	62 deg

Table 4.12: 'Current Model' Parameters

After tuning the parameters to obtain a close match with type 1 tests, type 2 and 3 tests were simulated using this modified version of the SRS which includes the 'Drag Model' acting on the RUs and the 'Current Model'. The results of the RU 1 position and error for a type 3 test are shown in Figure 4-18 and 4-19 respectively:

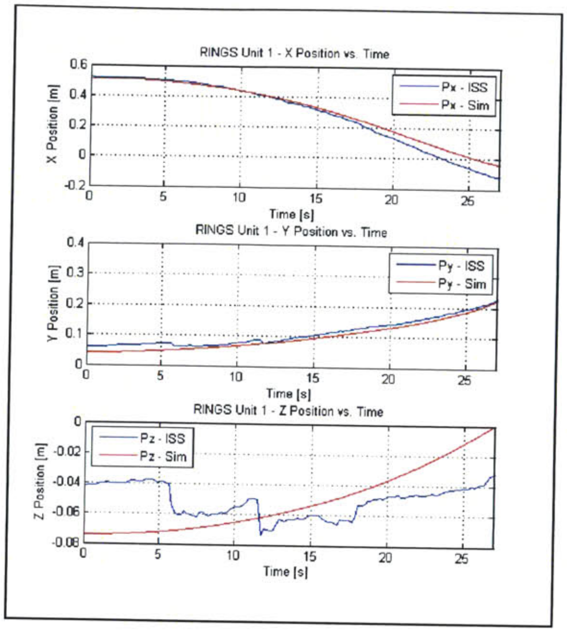

Figure 4-18: Axial EM Type 3 Test - RU 1 Position - ISS vs. SRS with 'Drag Model' and 'Current Model'

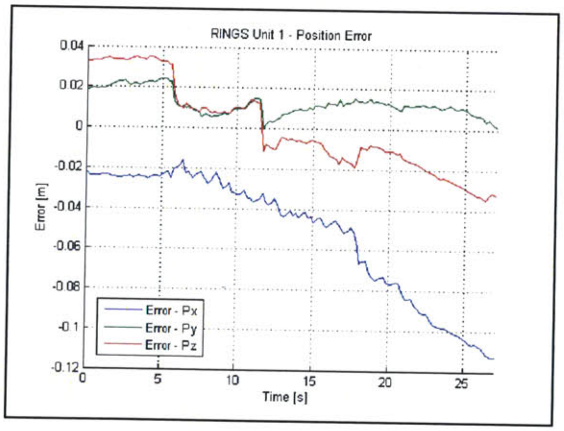

Figure 4-19: Axial EM Type 3 Test - RU 1 Error - ISS vs. SRS with 'Drag Model' and 'Current Model'

For the attraction portion of the test ($t < 15s$), the figures above show that the modified SRS predicts the position of RU 1 with a maximum error of $4.2cm$ and $2cm$ in the X & Y axes respectively. These errors represent 15% and 11% of the total distance traveled. The telemetry data for the Z-position contains jumps which might be caused by reflections of the US pulses with the RUs hardware. These reflections provide the SPHERES estimator erroneous TOF measurements and deteriorate its accuracy. After $t = 28s$ the system became unstable and the SRS results diverge from the experimental data. Even though the error in the X-axis stays below $10cm$ for the attraction portion of the test, it is observed that it monotonically increases. Thus, at this point, it can only be stated that the modified SRS (simulation including drag and current models) successfully models EM attraction maneuvers for a maximum period of $20s$.

The validation of the repulsion portion of the test was put on hold because a phase error that affected repulsion and not attraction did not make sense from a dynamics perspective. The following section discusses the RU hardware and software verification process used in order to confirm that the system was operating correctly before continuing with the dynamics model validation process.

4.6 RINGS Hardware/Software Verification

Section 4.5 describes the addition of a 'Current Model' to the SRS that increases the commanded RMS current by a constant linear factor and introduces an additional 'phase shift error' only when the phase offset commanded is 180 degrees (repulsion force). This section provides more insight into what caused each of those discrepancies between the SRS and the experimental data.

A RINGS hardware verification was performed to fully characterize the shape of the magnetic field generated by the RU coil. A test coil of $8.2cm$ diameter with 36 turns is co-axially centered with a RU coil and connected to an oscilloscope (on a $1M\Omega/18$ pF input) to measure the induced voltage on the test coil while the RU coil drives current. In this experiment, the RU is commanded current levels from 1A to 12A at 1A steps and the induced voltage on the test coil is recorded. Figure 4-20 shows the induced voltage on test coil when the RU is commanded 3A RMS:

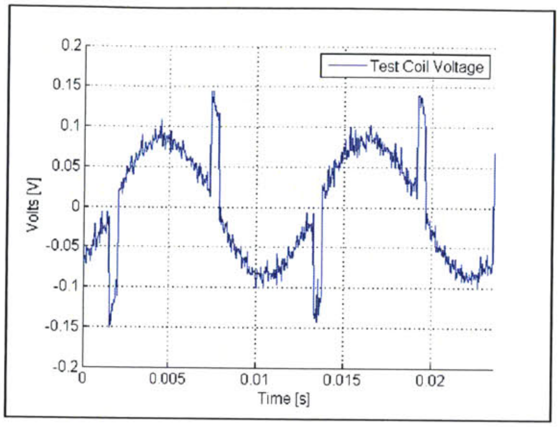

Figure 4-20: RINGS Hardware Verification - Induced Voltage - 3A RMS

In Figure 4-20 it is observed that the wave contains what is commonly referred as a 'glitch'. This glitch can be described as an addition of an alternating pulse twice the frequency of the sine wave to the sine wave itself. This anomaly is observed for all the tested current levels. The 'glitch' has an alternating positive and negative value in each cycle and always happens at the same time point of the cycle. As the current level increases the duty cycle and magnitude of the glitch increase.

By taking the Fast Fourier Transform (FFT) of the recorded waves, it was determined that its fundamental frequency is around 83 Hz, which is the value expected according to specifications. Figure 4-21 shows the FFT of the induced voltage when the RU is commanded 3A RMS.

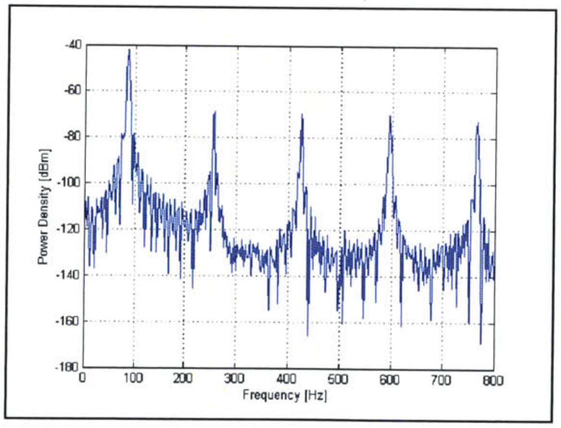

Figure 4-21: RINGS Hardware Verification - FFT - 3A RMS

By integrating the FFTs of the induced voltages at different RMS current levels, the additional power contained in the 'glitched' wave with respect to a perfect sinusoid was determined. The results are shown in Table 4.13:

I RMS [A]	Additional Power [%]
-12	2.86
-10	4.93
-7	9.00
-3	27.7
-1	39.9
1	38.1
3	25.3
7	9.61
10	5.28
12	3.61

Table 4.13: RINGS Hardware Verification - Additional Power

The shaded values are believed to be skewed due to the high noise in the acquired waveforms. Given that the additional power proved to be significant it was decided to connect an external Hall-Effect sensor[2] and an oscilloscope in series with the RUs' coils. This experiment provides a direct measure of the current that circulates through the coils. Figure 4-22 is a diagram of the test set-up.

[2] Hall-Effect Sensor Part Number: ACS750 SCA-075 made by Allegro Microsystems.

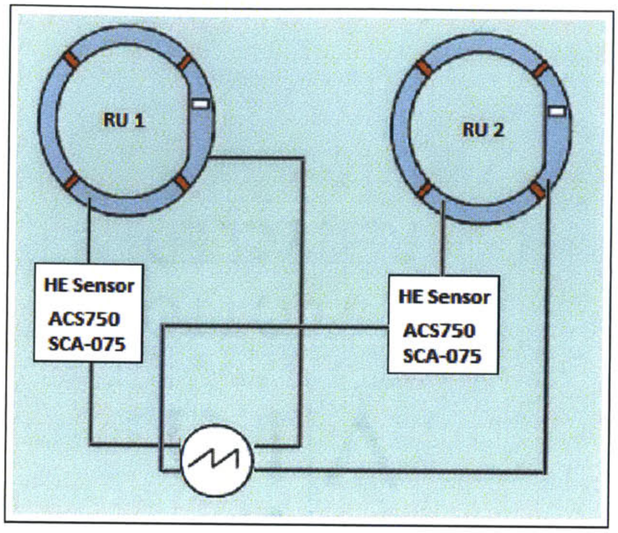

Figure 4-22: Hardware Verification Test Setup

The RUs are commanded RMS current levels from 1 to 10 A and the resulting RMS current measured by the HES is recorded. Figure 4-23 shows the measured RMS cuerrent as a function of the commanded RMS current:

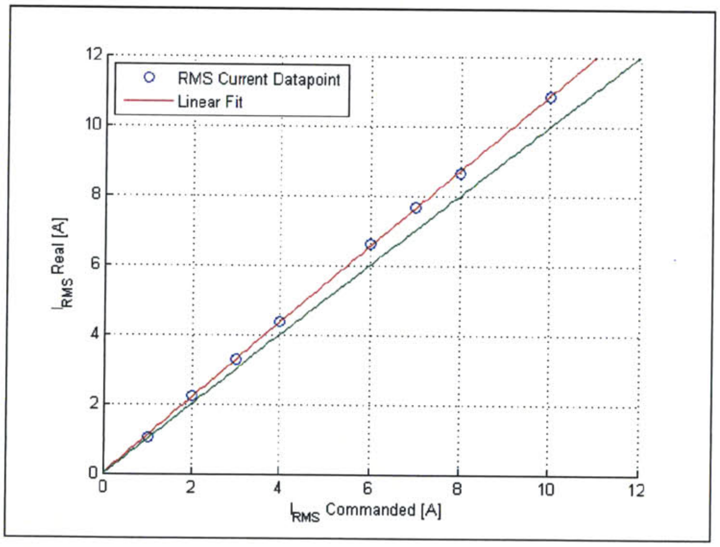

Figure 4-23: Commanded vs. Real I_{RMS} Current - Error: 8.6%

By using a linear regression, it is determined that the error between the commanded and the actual RMS current flowing through the coils is 8.6 %. This discrepancy can be explained by the fact that the sampling rate of the HES in the RINGS is not high enough to capture the power added by the 'glitch' and thus the RINGS current controller is fed back with an RMS value that is lower than the real one. The difference between this error and the additional power that was used as a parameter in the 'Current Model' of the SRS (8.06%, see Table 4.12) is 0.56%.

The second part of the RINGS hardware verification assesses the correct functionality of the current synchronization mechanism between the two RUs. The tests consist in commanding both RUs to different constant current levels (1A through 12A at 1A steps intervals both in 0 and 180 degrees phase shift). During these tests the current waves are recorded using the same oscilloscope to measure their phase difference.

When the RUs are commanded to be in-phase (0 degree shift), the RINGS behave as expected and the current waves in the coils are permanently in-phase. However, in the tests that command a 180 degree phase offset, it is observed that the current waves randomly jump in and out of phase. The periods that the phase shift is 0 or 180 degrees are also random and it is not possible to discern any type of pattern. Figure 4-24 is a snapshot of the current measurements during one of the 180 degrees phase shift tests:

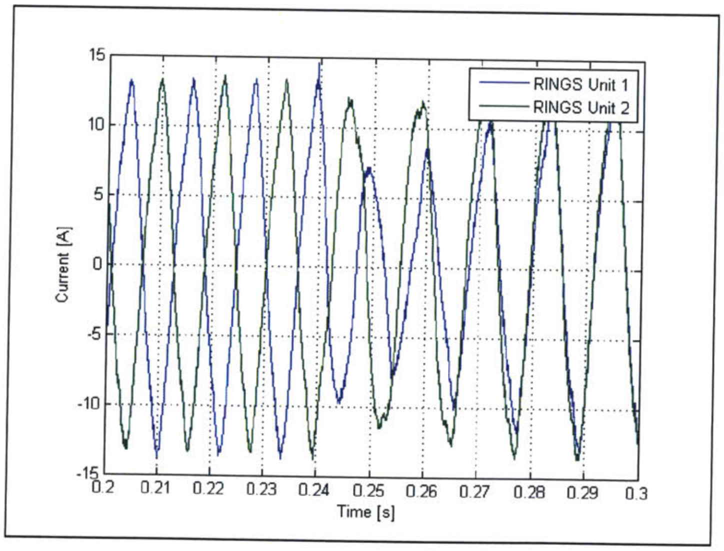

Figure 4-24: Hardware Verification - Phase Shift Anomaly

Initially, the two waves are 180 degrees out-of-phase as expected. However, at

$t = 0.24s$ (without giving any new command) they start transitioning to be in-phase. After an analysis of possible causes of this anomaly, researchers identified a memory allocation error in the RINGS firmware so it was modified to fix this erroneous behavior.

Researchers conclude that RUs' current waves alternating to be in and out of phase is the cause of the 'weaker' repulsive force observed in the ISS data in comparison to the one predicted by the SRS. By modifying the SRS to add an 'average phase error' of 62 degrees during the 'repulsion phase', this weaker repulsive force could be modeled to accurately match it to the force observed in the ISS test.

Since the firmware was modified to correct for the repulsion memory allocation error, SRS validation tests for repulsion were completed in the following ISS test session. The results of this validation are discussed in 4.7

4.7 EM Force Validation: Repulsion

After the hardware verification described in Section 4.6, a set of tests to validate 'EM repulsion' were performed aboard the ISS. In the same manner as the 'EM attraction' tests, the RUs are initially in an axial configuration with an initial separation distance of $0.8m$ in the X-axis. During the 'EM Phase' both RUs drive a constant RMS current of 5A. The current waves have a phase shift of 180 degrees to produce the repulsive EM force. Figure 4-25 compares the position results from the SRS and experimental ISS data and figure 4-26 shows the error between them.

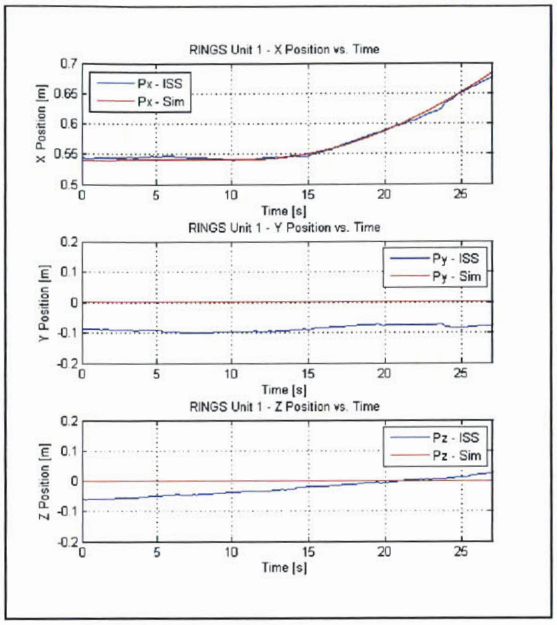

Figure 4-25: Axial EM Repulsion Test - Position

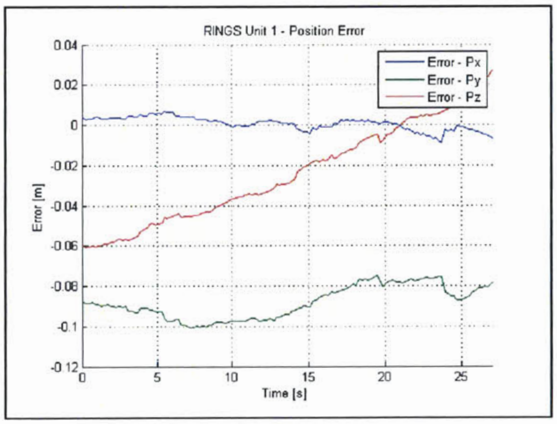

Figure 4-26: Axial EM Repulsion Test - Error

The error in the X-axis, where the maximum EM repulsive force occurs, is less than $1cm$ across the test. The error observed in the Y & Z axis are caused by the fact that during the 'Initial Positioning' phase the SPHERES telemetry system was not very accurate and as it can be seen in Figure 4-25 the RU didn't start the 'EM Phase' in the desired $0m$ position in the Y & Z axes. From the data gathered in this test it is not possible to determine if the error in position are bounded since the error in the Z-axis does not show to converge during the length of the test.

4.8 EM Torque Validation

The objective of these tests is to gather data on the EM actuation capability in the shear configuration. Similarly to the axial EM actuation tests, the RUs navigate to their initial position using the SPHERES thrusters. Figure 4-27 shows the initial configuration after the 'Initial Positioning' phase:

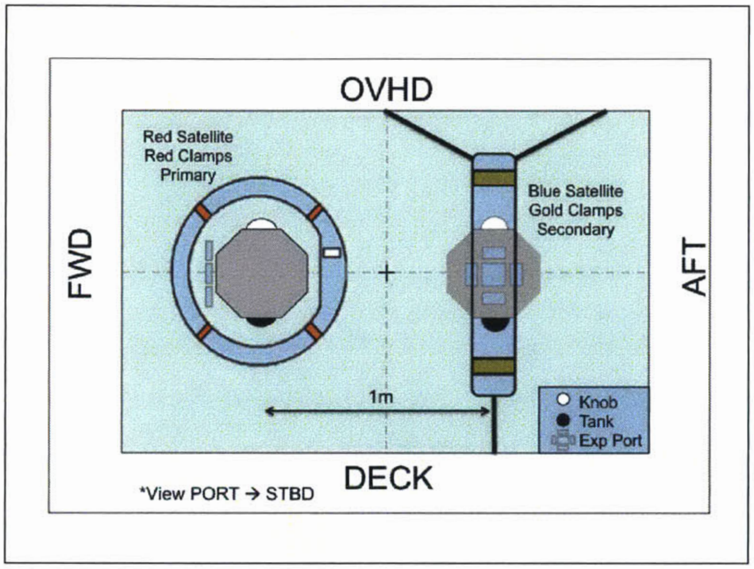

Figure 4-27: EM Shear Test - Initial Configuration

As it is shown in the previous figure, in the shear configuration RU 1 is rotated 90 degrees relative RU 2 about the Z-axis. In this configuration and due to the fact that the two RUs are not perfectly aligned, a shear force and a torque are generated.

Given that both position and attitude of RU 1 change during the 'EM Phase', only the position and attitude of RU 2 are fed from telemetry data obtained during ISS tests. In these tests, the complete state of RU 1 is propagated and fed back to the SRS dynamic engine. Figure 4-28 shows a block diagram describing how inputs are fed into the SRS for the shear EM tests:

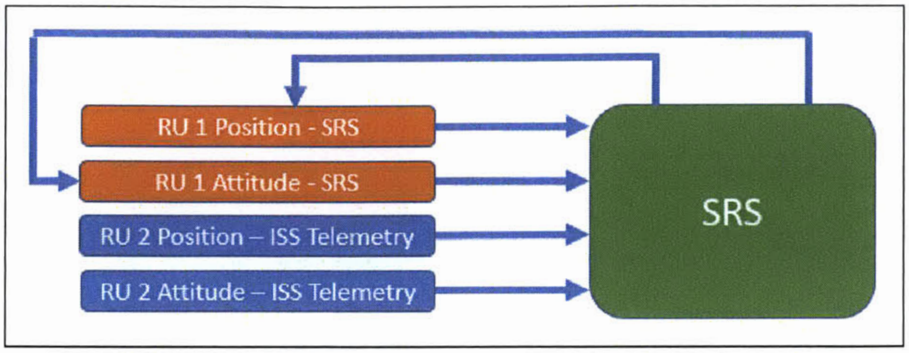

Figure 4-28: SRS Validation of Shear Tests - Inputs

Figures 4-29 and 4-30 compare the position and attitude data of RU 1 during the 'EM Phase' predicted by SRS and the experimental ISS data:

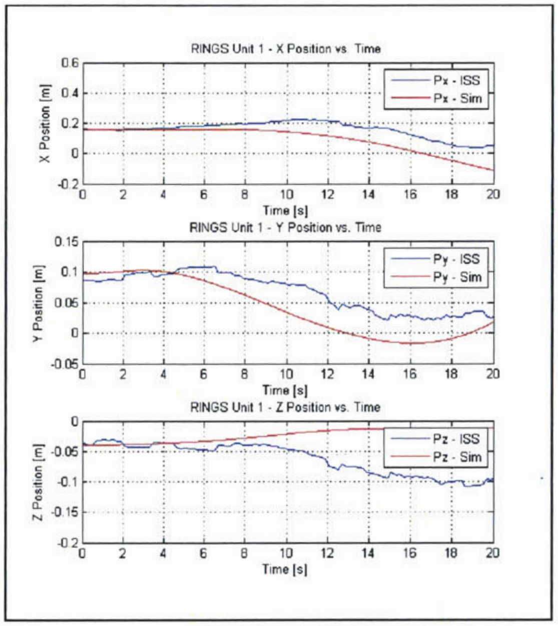

Figure 4-29: Shear EM Test Type 1 - RU 1 Position - ISS vs. SRS

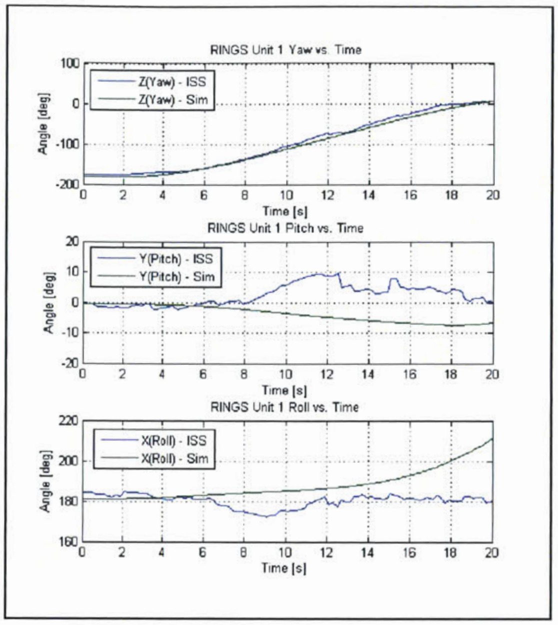

Figure 4-30: Shear EM Test Type 1 - RU 1 Attitude - ISS vs. SRS

The attitude quaternions were converted to 'Euler Angles' using a 321-rotation. In terms of Euler Angles, RU 1 starts with a 180-degree rotation in the X-axis meaning that the SPHERES CO_2 tank is facing the deck and the regulator knob is facing the ISS Overhead. In the Z-direction, the unit starts with a negative 180-degree rotation meaning that the SPHERES satellite expansion port is facing the AFT wall of the ISS. The Y-rotation is 0 degrees meaning that there is no angular difference between the inertial reference frame and the body reference frame.

In this configuration it is expected that the EM actuation would produce a torque about the Z-axis and a force in the Y-axis. This is confirmed by the data of the test shown in the figures above. Initially, RU 1 repelled from RU 2 and then attracted when the rotation was around 90 degrees at approximately $t = 10s$. After time $t = 20s$, when RU 1 second rotation occurs, the rotation about the X-axis was large enough that the generated torque caused the system to become unstable.

Figure 4-31 shows the error for both position and attitude during the shear test. There is a large discrepancy in the X & Z positions as well as in the roll angle. During this test, an abnormal behavior was observed in the position and attitude estimation of RU 2: at $t = 10s$ there is an instantaneous jump of $10cm$ and 10 degrees in the estimate of RU 2. A possible explanation of the divergence of the results are the inaccuracies in the state estimation of RU 2. However, the rotation about the Z-axis predicted by the SRS, the major effect of EM actuation expected for this test, matches the experimental ISS data with maximum error difference of 10 degrees.

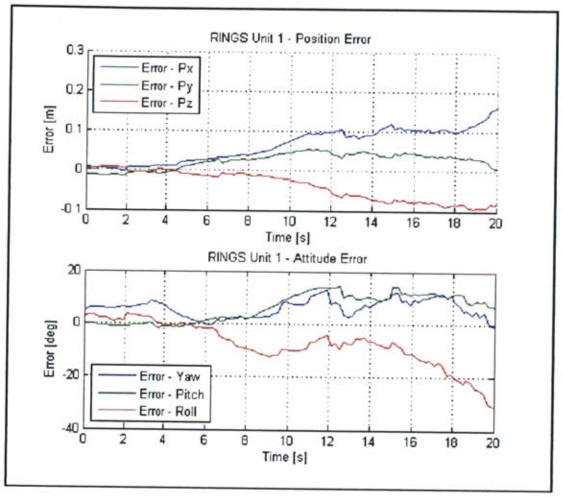

Figure 4-31: Shear EM Test Type 1 - RU 1 Error - Validation

Given the small differences in the rotation about the Z-axis between the ISS test and the SRS, it is considered that the SRS can successfully model tests in which shear forces and torques occur with an error of 10 degrees.

4.9 Summary

This chapter steps through the SRS validation process through comparisons between the results of tests performed in the ISS and the SRS. First, ISS and SRS results for System Identification Tests are compared and values for CoM, inertia properties and thrusters force matrix are determined. These tests assess the effects that the thruster impingement have on the system. Subsequently, 'Initial Positioning' tests are used to validate the new updated RINGS physical parameters. Afterwards, EM actuation tests (Axial EM attraction, Axial EM repulsion and Shear EM tests) are compared against the SRS. These tests revealed the need to account for the effect that drag forces have on the RUs. In addition, a verification of the RUs' hardware and software was necessary to explain discrepancies observed in the results.

The maximum position error in the EM attraction and repulsion tests is $10cm$. In the case of the EM shear test, the maximum errors in position and attitude are $15cm$ and 30 degrees respectively. At this point, the researcher concludes that the SRS is a tool that can be used to test control algorithms coded in the SPHERES satellites with an accuracy in position and attitude of 15% for a maximum time period of $25s$.

Chapter 5

Evaluation of Closed-Loop Position Controllers Using the SRS

5.1 Introduction

Using the latest version of the SRS, this chapter analyzes the performance of a Proportional-Integral-Derivative (PID) controller for the position of the RUs when they are in an axial configuration. Then, a direct adaptive control method known as 'Input Shaping' is incorporated to the PID controller in order to achieve stability of the system.

Given the difficulties experienced while operating the RUs simultaneously aboard the ISS, all the tests in this chapter model RU 2 as being at a fixed position inside the testbed and driving a constant RMS current level. The closed-loop position control tests start with the RUs placed in an axial configuration and can be classified by the following variables:

1. RINGS initial orientation within the ISS testbed: there are two possible orientations that may render optimal for the RINGS actuation capability. These are described, simulated and compared in section 5.3.

2. Input type: 'Station Keeping' tests command RU 1 to keep the initial separation distance and orientation constant. 'Step Input' tests command RU 1 to move

to a target separation distance from RU 2 along the axial axis.

3. Attraction vs. Repulsion Step Input tests: In 'Attraction' tests, the RUs' target separation distance is lower than their initial separation distance. Contrarily, in 'Repulsion' tests, the RUs' target separation distance is greater than their initial separation distance.

Table 5.1 describes the parameters of each type of test that is simulated and described in this chapter:

Test Type	Controller Type	Testbed Configuration	Input Type	Initial Sep. [m]	Target Sep. [m]
1	PID	A	Station Keeping	0.6	0.6
2	PID	B	Station Keeping	0.6	0.6
3	PID	A	Step	0.6	0.4
4	PID	A	Step	0.5	0.85
5	PID with Input Shaping	A	Step	0.5	0.85

Table 5.1: CLPC Test Parameters

5.2 Description of the CLPC

A PID controller is developed to demonstrate the capability of the RUs to achieve position control in an axial configuration. The EM PID controller uses the RU's coil as the actuator to generate EM forces and achieve a target separation distance in the axial axis. The standard SPHERES PID controls the other five DOF and maintains the axial configuration using thrusters. Figure 5-1 is a block diagram of the PID controller.

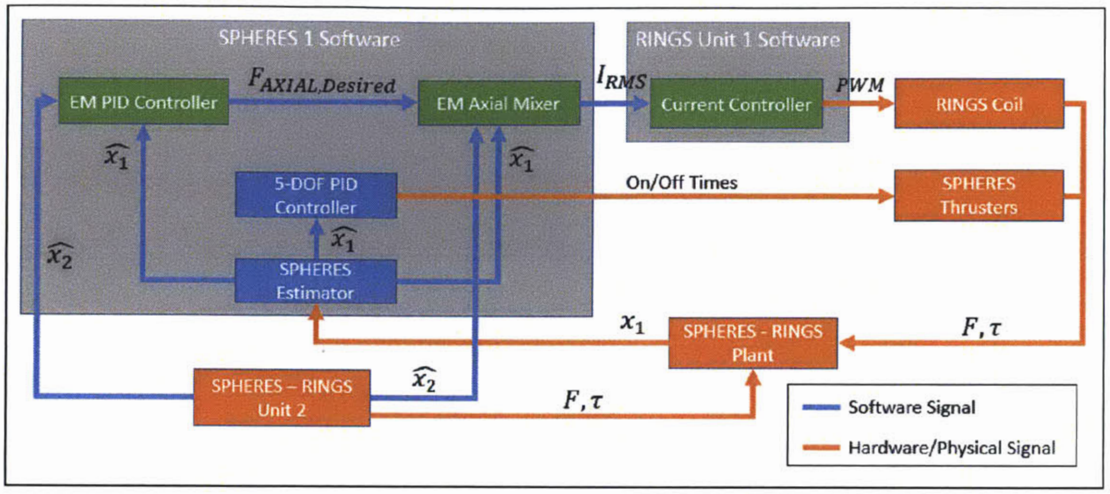

Figure 5-1: PID Position Controller

In addition to the PID controller, an 'EM axial mixer' is implemented to convert the desired force to a RMS current level. In order to create the mixer, the RMS current level of RU 2 ($I_{RMS,2}$) is first set to a constant value. Then, using the 'Near-Field EM Physics Model' a function that outputs the desired RMS current for RU 1 as a function of desired EM axial force and separation distance can be obtained:

$$I_{RMS,Desired} = f(F_{Axial,Desired}, d)$$

The functions in Figure 5-2 plot the required RMS currrent in RU 1 to achieve 0.1N (same force provided by SPHERES thrusters) as a function of the separation distance when $I_{RMS,2}$ is set to $7A$ (red) or $10A$ (blue). As an example, when $I_{RMS,2} = 10A$ and the RUs are at a distance of $85cm$, an $I_{RMS} = 15A$ is required to achieve 0.1N of EM force. If 0.2N is desired instead, these functions should be scaled by a factor of 2. The black dashed line represents the maximum RMS current level that can flow through the RU coil. These functions were approximated using a 7th-order polynomial and implemented inside the SPHERES satellites' controller algorithm.

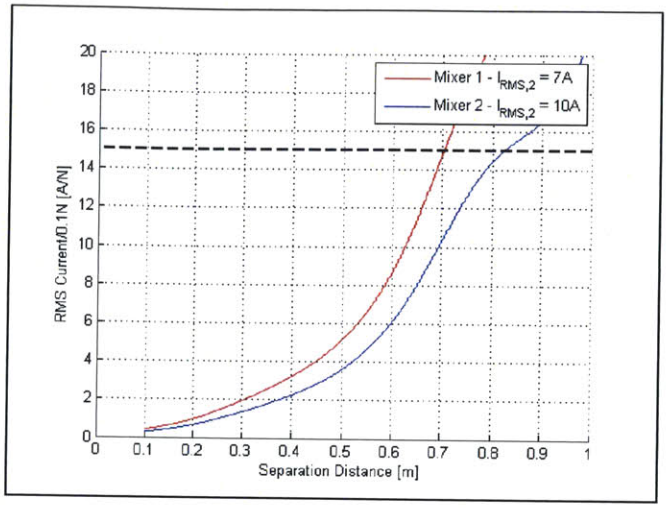

Figure 5-2: Mixer Function for Axial Configuration - I_{RMS}/F vs. Axial Separation Distance

The desired EM force that is output by the EM PID controller is fed into the EM axial mixer along with the estimated separation distance between the RUs to obtain the desired RMS current level for RU 1. At the end of each SPHERES control cycle, this desired RMS current is sent from the SPHERES satellite to the RU.

5.3 Axial Station Keeping Tests for Optimal RU Orientation

In Chapter 4, drag forces acting on the RUs were characterized assuming a constant airflow in the test volume. Model calibration and the analysis performed by Setterfield [22] determined that the maximum average air velocities occur in the Y & X directions and their estimated average value are $20cm/s$ and $16cm/s$ respectively. In addition, as it is explained in Section 4.3, there is thruster impingement in the four SPHERES thrusters that are on the RUs' X-Z plane. Given these two conditions, two possible configurations could prove to be optimal to counteract the effects of the airflow for axial configuration tests:

1. Configuration A (Figure 5-3): The SPHERES satellite CO_2 tank points in the positive Y-axis, while the expansion port points towards the positive Z-axis.

In this configuration the impinged thrusters are oriented in the $\pm Z$ directions which is where the airflow speed is the lowest ($13cm/s$).

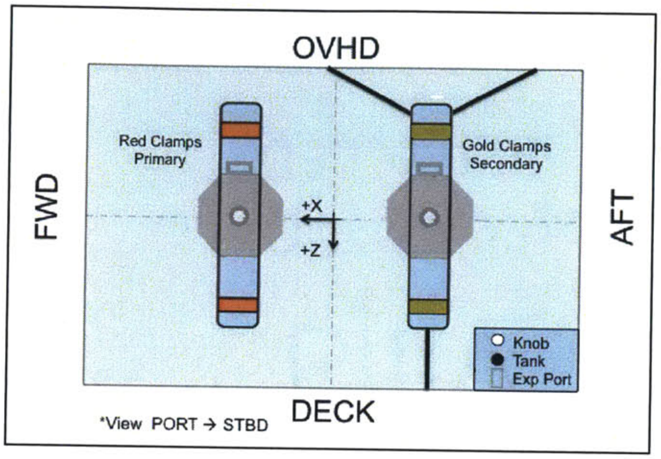

Figure 5-3: Test - Configuration A

2. Configuration B (Figure 5-4): The SPHERES satellite CO_2 tank points in the positive Y-axis, while the expansion port points towards the positive X-axis. In this configuration, the greatest frontal area of the RU faces the Z-axis where the airflow speed is the lowest.

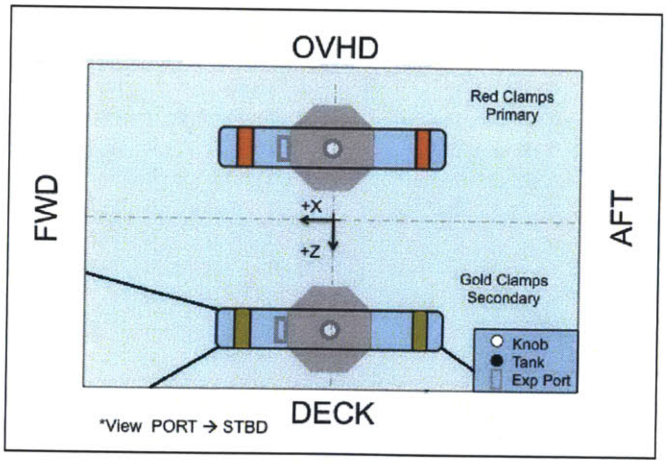

Figure 5-4: Test - Configuration B

Tests 1 & 2 (see Table 5.1) are simulated with the objective of assessing if the PID controller is capable of performing a SK maneuver, where RU 1 maintains a constant separation distance from RU 2. In addition, tests 1 & 2 compare the performance of the controller in keeping the RU at the desired separation distance for the two possible configurations 'A' or 'B'. Figures 5-5 and 5-6 show the position and attitude errors, desired EM force and commanded $I_{RMS,1}$ for tests 1 & 2 respectively. The conventions used for these plots are:

1. The reference for both positions in the three axes and attitude is constant at 0.
2. Positive RMS current values correspond to RUs' current being in-phase while negative values correspond to a 180-degree phase offset.

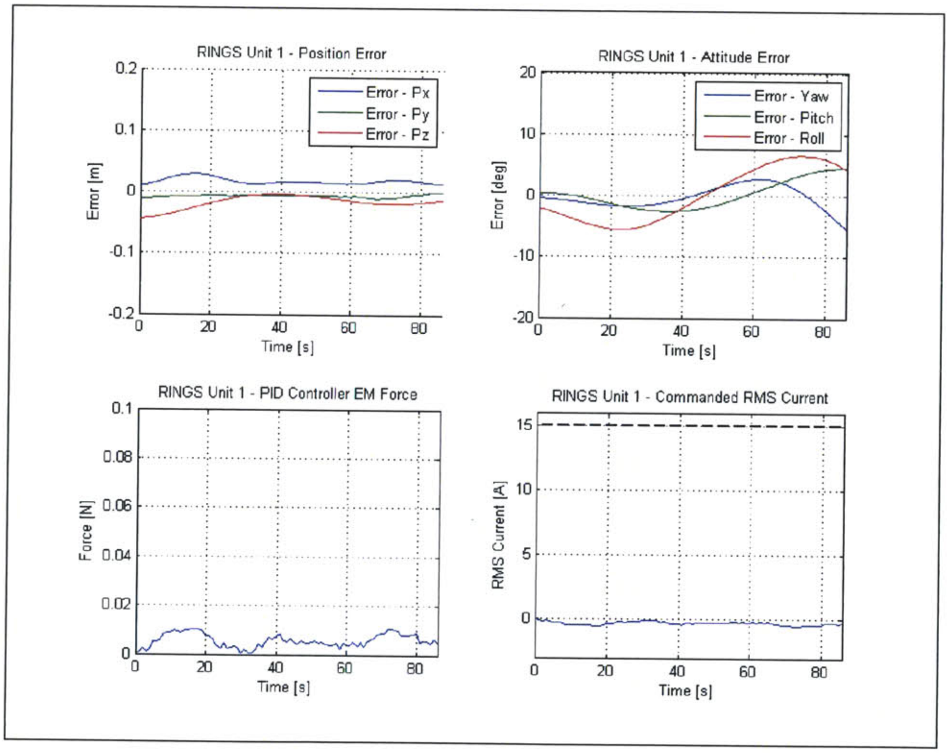

Figure 5-5: PID Controller - Test 1 (Configuration A)

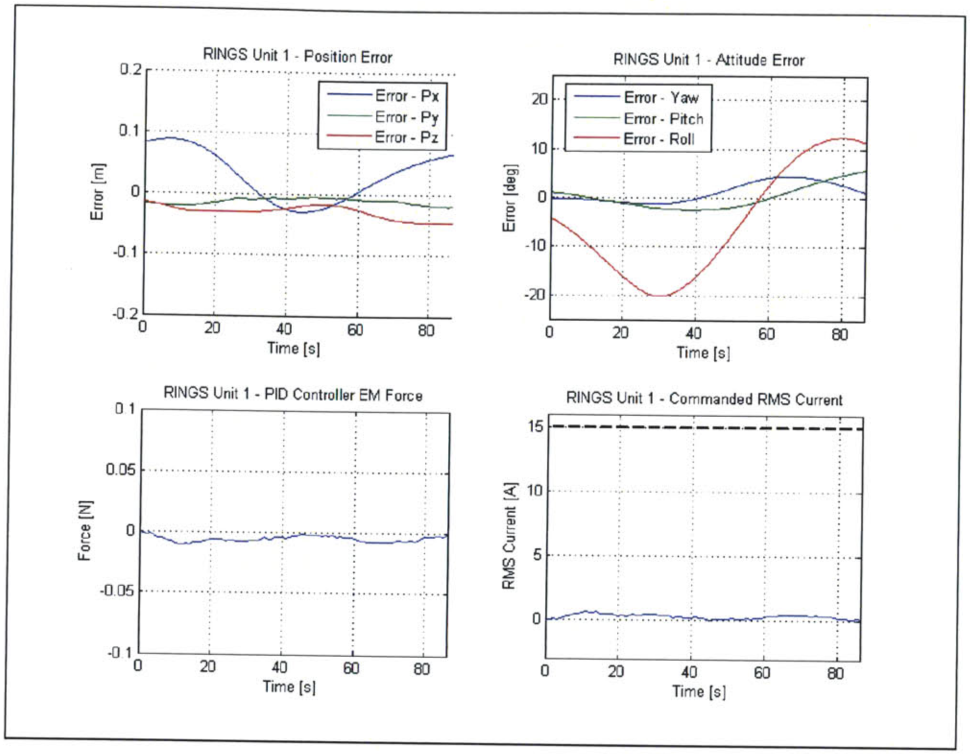

Figure 5-6: PID Controller - Test 2 (Configuration B)

In both scenarios, the EM controller is able to keep RU 1 at a stable position and the required RMS current levels are below the RINGS actuator's saturation point. In addition, the SPHERES controller successfully controls the position in the remaining two axes and the RU attitude. Table 5.2 shows the maximum and RMS errors for both position and attitude. It is observed that both controllers perform better when the RUs are placed in configuration 'A,' than in 'B'. The maximum position error in configuration 'B' is double the error observed in configuration 'A' while the error in attitude is approximately three times larger. Also, the RMS error is greater for configuration 'B'. Given these results, it was decided that the 'Step Input' and 'Input Shaping' tests, which are described in the following sections, would be simulated in configuration 'A'. Using this configuration has the added advantage that it is equivalent to the one already used for the 'EM Actuation Tests' during the ISS tests described in Chapter 4. This gives the scientists confidence that configuration 'A' doesn't have operational constraints that might prohibit performing these tests in future ISS test sessions.

Test Configuration	A	B
Position - Max. Abs. Error [m]	0.0437	0.0879
Position - RMS Error [m]	0.0199	0.0499
Attitude - Max Abs Error [deg]	6.5523	20.1574
Attitude - RMS Error [deg]	3.8283	10.6486

Table 5.2: PID Controller Performance Comparison - Configuration A vs. B

5.4 Step Input Tests

Test 3 places the RUs at an initial separation of $60cm$ and a step input of $-20cm$ (attraction) is commanded. The results of the test are shown in Figure 5-7:

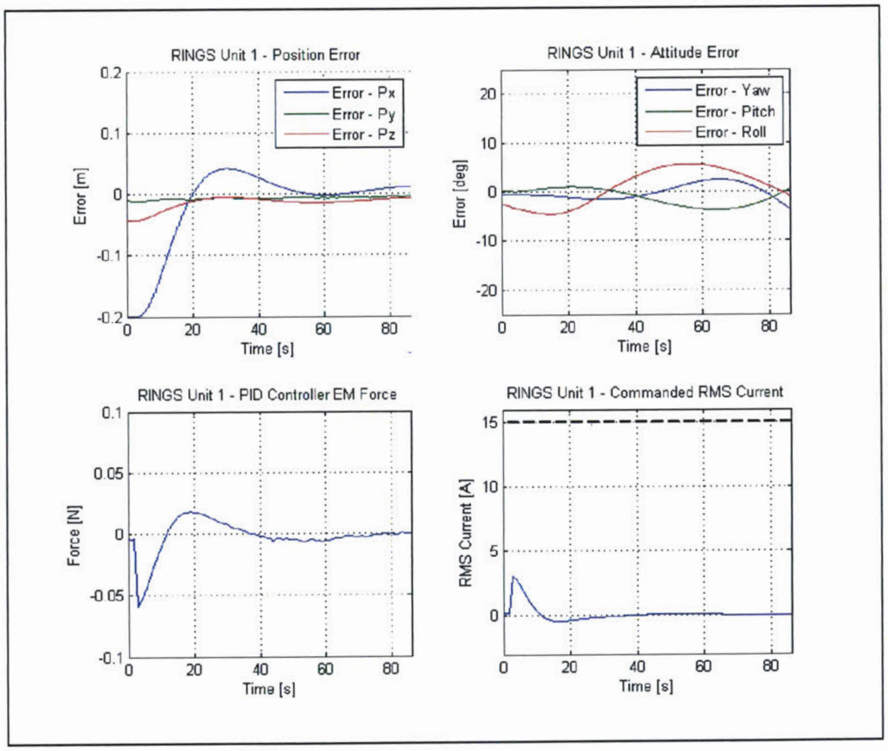

Figure 5-7: PID Controller - Test 3 - Step Input - Attraction

As in the previous figures, subfigures (a) & (b) show the position and attitude errors (reference is at 0) respectively. It is observed in subfigure (a) that the controller manages to move RU 1 to the commanded separation distance in the X-direction while also maintaining the error in the Y & Z dimensions below $4cm$. The response has a rise time of 11.3 seconds, a percent overshoot of 20.8% and a settling time of 85 seconds. Subfigure (b) shows that the controller is also effective at keeping the desired attitude within ±5 degrees. Finally, sub-figures (c) & (d) show that the desired EM force has the same order of magnitude as the SPHERES satellites thrusters capability. The required RMS current levels that are outputted by the EM mixer are below the maximum current RMS levels that the RINGS is able to provide (marked by the black dashed line) guaranteeing that the actuator is not being saturated during the test.

Test 4 is designed to assess the capability of the PID controller to drive the RUs from an initial separation distance to a larger one. In this test, RUs are placed at an initial separation distance of $50cm$ and given an step input of $+35cm$. Figure 5-8 shows the results of this test.

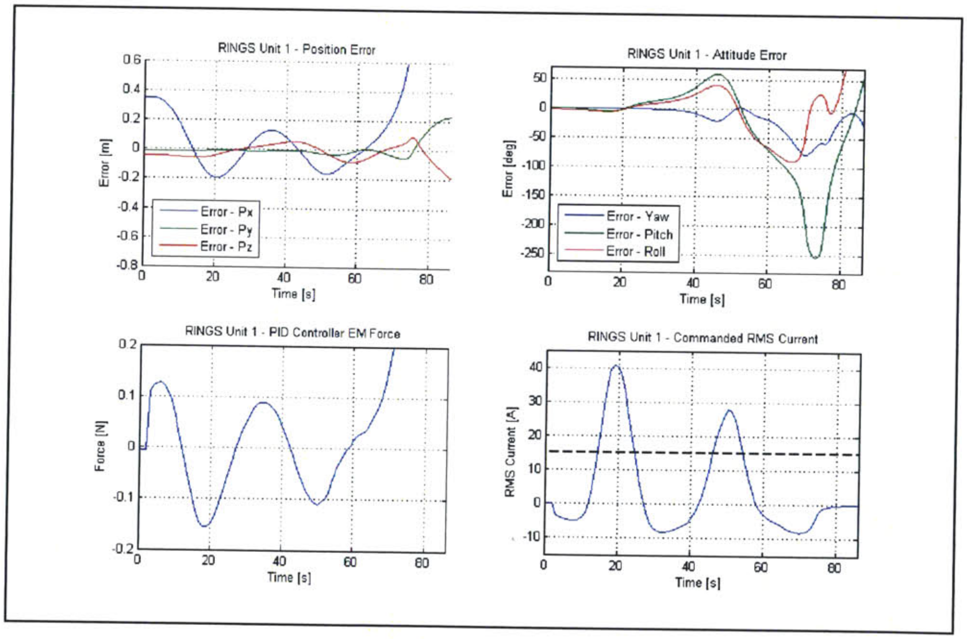

Figure 5-8: PID Controller - Test 4 - Step Input - Repulsion

Contrary to the previous test, the PID controller fails to drive RU 1 to the commanded separation distance and the system becomes unstable. In subfigure (b) it is observed that the RU attitude error monotonically increases until $t = 45s$ where the pitch error achieves a value of 60 degrees. These large errors in attitude make the designed axial EM PID controller ineffective due to the coupling that exists between the RU state and the generated EM forces and torques. Note that: (1) the EM force that is desired in the axial direction is not achieved since the RUs are not in an axial configuration, (2) EM torques and non-axial EM forces are generated that the thrusters need to counteract to maintain the RUs axial configuration. It is observed in subfigure (d) that at $t = 14.5s$ the RU actuator is saturated and is not able to provide the commanded force.

5.5 Direct Adaptive Control

Due to the instability observed in Test 4, a more robust control method known as 'Input Shaping' or 'Model Referencing' [23] was implemented. The commanded position and attitude are fed into a reference model that is designed to produce an output with the desired response characteristics, such as settling time, rise time and overshoot. Given that the controller tracks the output of reference model instead of directly the step input, this method yields a much smaller tracking error and is less likely to saturate the actuators. Figure 5-9 [1] shows a block diagram of the EM PID controller using 'Input Shaping'.

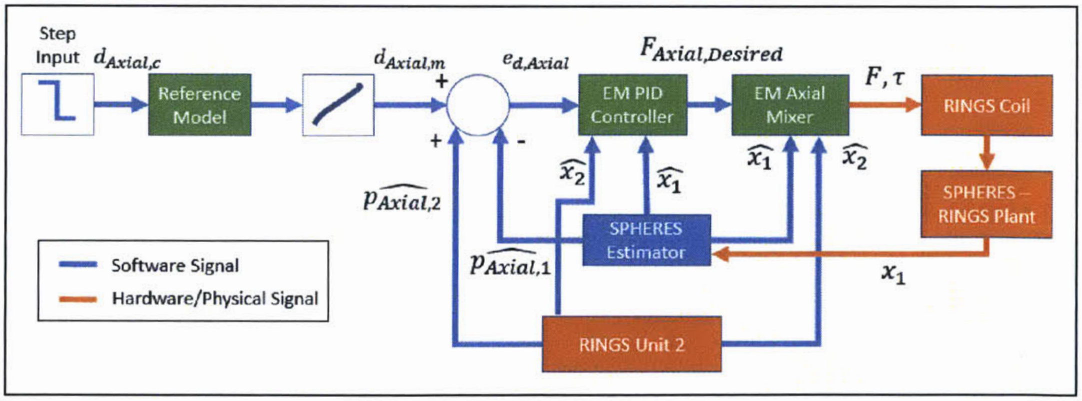

Figure 5-9: EM PID Controller with 'Input Shaping'

In Figure 5-9: $d_{Axial,c}$ is the commanded separation distance, $d_{Axial,m}$ is the sepa-

[1] Some blocks have been omitted for simplification.

ration distance outputted by the reference model, $e_{d,Axial}$ is the distance error in the axial axis and $\hat{p}_{Axial,1}$ and $\hat{p}_{Axial,2}$ are the estimated RUs' positions in the axial axis. Figure 5-10 shows the results of this test:

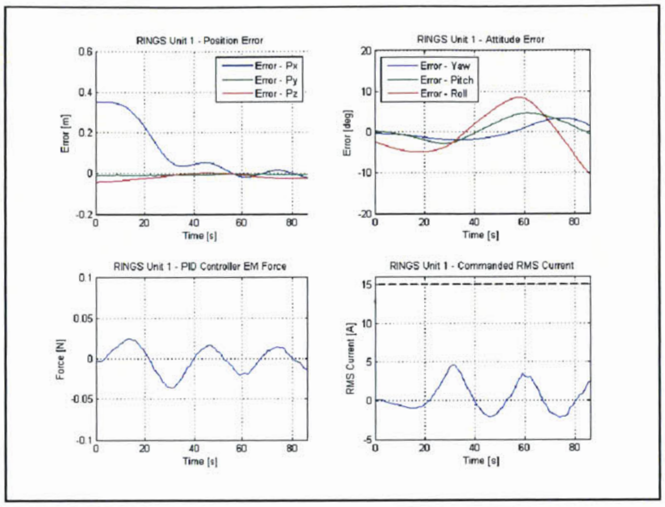

Figure 5-10: EM PID Controller - Input Shape - Repulsion

In this test the controller successfully drives the system to the commanded separation distance. The response has no overshoot, the rise time is $36.97s$ and the settling time is $53.64s$. Subfigures (c) & (d) show that the desired EM force has the same order of magnitude as the SPHERES thrusters and the EM actuator is not saturated. By using the 'Input Shaping' method it is possible to drive the RU to the desired separation distance in an stable manner. However, it is observed in subfigure (b) that the error in the roll angle is increasing. Given that the simulation could not be run for a longer period of time, at this point it is not possible to determine if the attitude is stable.

5.6 Summary

This chapter uses the SRS as a platform to simulate and test the performance of a closed-loop position controller that uses the RUs' coils as the actuators for controlling the separation distance in the axial axis and thrusters for the other five DOF. For these tests, RU 2 is at a fixed position and is commanded a constant RMS current level. Simulation results show that a PID controller is stable for SK and attraction maneuvers. However, an adaptive control method known as 'Input Shaping' is necessary to achieve stability for repulsion maneuvers. Further analysis needs to be performed to determine if the attitude of the RU is stable for this type of maneuver.

Chapter 6

Conclusions and Future Work

6.1 Conclusions

This thesis begins with an introduction, motivation and theoretical background of EMFF. Subsequently, a high-level description of RINGS provides a framework for the primary contributions of this work.

The initial contribution of this thesis is the development and modeling of a PI current controller in Simulink. The implementation of this module in RINGS is to control of the current that circulates through the RUs' coils, which is directly proportional to the generated EM forces and torques. The creation and validation of the current controller model using experimental data allowed researchers to evaluate the stability of this controller for the RINGS experimental test scenarios and find the gains that met the performance requirements.

The second contribution of this work is the modeling of the RINGS as an extension to the existing SPHERES simulation referred to as SRS. 'EM Actuation' open-loop tests are validated by comparing their results to the ones obtained during the ISS test sessions. The validation process required the tuning of the RUs' physical parameters (CoM, inertia properties and thrusters force matrix) as well as a revision of the SRS to include the effects of drag forces acting on the units. In addition, a general explanation of how to integrate new payloads to the SPHERES simulation and serial communication system is given. The SRS can be used as a tool to test, debug and evaluate control algorithms for RINGS before being tested on the ground testbed or the ISS.

Finally, this thesis develops a PID position controller for the case in which the RUs are initially positioned in an axial configuration. This controller uses EM forces to control the RUs' separation distance in the axial axis and SPHERES thrusters for the position in the two other axes and for attitude. After SRS results showed that the PID controller is not stable for repulsion maneuvers, a direct adaptive control method known as 'Input Shaping' was used to achieve system stability for this maneuver. In summary, it is shown that controlling the axial separation distance between the RUs using EM actuation is feasible.

6.2 Future Work

This thesis has developed a model of RINGS that includes the effect of drag forces on the RUs. However, this model has a pair of limitations:

1. Drag Coefficients: The plane of the RU was modeled as a flat solid plate perpendicular to the flow ($C_d = 1.28$) while the other two planes as a smooth brick ($C_d = 2.1$). However, the RUs are not solid as flow can go through them. Thus, the numbers used for C_d could be revised by placing the RUs in a wind tunnel and measuring the drag forces at the adequate Reynolds number or by using a CFD tool to obtain more accurate values of C_d.

2. Constant Attitude: The model takes the frontal areas and drag coefficients in the three axes as constant inputs. Effectively, the model assumes that the RUs' attitude will remain constant throughout the test for the calculation of the drag forces. However, as the attitude of the RU changes from its initial value, both the frontal area as well as the C_d in all three axes will change making this assumption invalid. For the axial configuration tests described in Chapter 5, this assumption holds as long as the attitude deviation of the RU from the axial configuration is small. However, for tests that involve changes in attitude this

model should be generalized.

The current version of the SRS can only be run in 'Simulink Mode' meaning that it has to be open in Simulink to execute. This mode of execution has the disadvantage that it is not easily distributable and major efforts have to be done to set the host architecture variables appropriately. The SPHERES simulation can be generated into independent C/C++ source code which greatly improves performance and portability. However, configuration and compatibility issues have prevented researchers from being able to generate independent source code for the SRS. A follow-on work effort could be to resolve these misconfigurations to be able to compile the SRS and make it easily distributable.

In Section 5.5, a controller that uses an adaptive control approach known as 'Input Shaping' is implemented. This work leaves room for research on more complex adaptive control algorithms such as using time varying gains.

In their theses, Buck [4] and Eslinger [20] developed controllers for RINGS based on 'Optimal Control' and 'Dynamic Programming' methods respectively. Their work include simulations of these controllers for scenarios that can be tested aboard the ISS. However, these controllers were never migrated or tested in the SPHERES-RINGS architecture. Thus, one principal area for further work is to implement these type of controllers in the SPHERES satellites, use the SRS to analyze their performance and, subsequently, test them in the ISS.

Currently, the RINGS software architecture is a 'foreground/background' (or superloop) system. In this type of architecture there is a looping construct for the main portion of the application and interrupts handle time-critical events. The main loop runs when there are no active interrupts. However, given the size, complexity and tight time-control that is required for RINGS, it is difficult to identify the interactions between all the software modules. A prime candidate for further development of RINGS is to migrate the firmware to a Real-Time Operating System (RTOS) approach. In this architecture, concurrent tasks communicate between themselves as they are all simultaneously managed by a kernel. Using this architecture offers the following advantages: (1) more efficient use the micro-controller resources, (2) easier characterization of application's performance and (3) shorter debugging/testing time. In addition, by using this architecture, a follow-on exploration could be to implement control algorithms in the micro-controller itself instead of the SPHERES satellite.

Up to this point, it has been observed that the communication between the SPHERES satellite and the RU is not completely reliable. Two major anomalies have been observed:

1. RUs firmware does not receive commands sent by the SPHERES satellite. Messages to change Operation Mode or set a RMS current level (See Appendix A) are occasionally lost. Possible causes of this issue are: (1) error in the interrupt routine of the RU firmware that handles the reception/processing of packets through the UART line, (2) error in the Expansion Port Version 2 (EXPV2) firmware.

2. Telemetry Data is lost for some time intervals. It has been noted that in some occasions, telemetry data is lost for some portions of the test. Possible causes of this error are: (1) data is lost in the communication line between the RU firmware and EXPV2, (2) data is lost when it is transferred from the SPHERES satellite to the ELC computer.

As it was explained in Section 4.1, the last phase of the RINGS tests is to 'Download Telemetry Data'. Currently, researchers receive an 'End of Test' code that indicates if any anomaly occurred during the test. Adapting the SPHERES GUI to parse RINGS telemetry data in a real-time fashion would give researchers more information about the test and would allow them to proceed appropriately during the ISS test session.

Bibliography

[1] University of Maryland. Final Report for RINGS Payload, NASA Contract NNH11CC33C. Technical report, DARPA, College Park, MD, September 2013.

[2] D. Alinger. System Analysis and Design for the Resonant Inductive Near-Field Generation System (RINGS). Master's thesis, University of Maryland, Department of Aerospace Engineering, 2013.

[3] S. A. Schweighart. *Electromagnetic Formation Flight Dipole Solution Planning.* PhD thesis, Massachusetts Institute of Technology, Department of Aeronautics and Astronautics, June 2005.

[4] A. J. Buck. Path Planning and Position Control and of an Underactuated Electromagnetic Formation Flight Satellite System in the Near Field. Master's thesis, Massachusetts Institute of Technology, Department of Aeronautics and Astronautics, June 2013.

[5] J. G. Katz. *Achieving Broad Access to Satellite Control Research with Zero Robotics.* PhD thesis, Massachusetts Institute of Technology, Department of Aeronautics and Astronautics, June 2013.

[6] ESA. Darwin Mission, December 2014. Online `www.esa.int/science/darwin`.

[7] O. Brown and P. Eremenko. Fractionated Space Architectures: a vision for responsive space. Technical report, Defence Advanced Research Projects Agency, 2006.

[8] J. Everist, K. Mogharei, H. Suri, N. Ranasinghe, B. Khoschnevis, P. Will, and W.-M. Shen. A system for in-space assembly. *Procceedings of 2004 IEEE/RSJ International Conference on Intelligent Robots and SystemsAIAA Spacecraft and Rockets*, 2004.

[9] NASA. Robotic Refueling Mission, December 2014. Online `http://www.nasa.gov/mission_pages/station/research/experiments/778.html`.

[10] D. R. Coulter. Nasas terrestrial planet finder mission: the search for habitable planets . *Earths: DARWIN/TPF and the Search for Extrasolar Terrestrial Planets*, 539:4754, 2003.

[11] T. Hashimoto, S.-i. Sakai, K. Ninomiya, K. Maeda, and T. Saitoh. Formation flight control using super-conducting magnets. *International Symposium on Formation Flying Missions and Technologies, Centre National dEtudes Spatiales, Touluse Space Center, France*, 2002.

[12] L. M. Elias. *Dynamics of Multi-Body Space Interferometers Including Reaction Wheel Gyroscopic Stiffening Effects.* PhD thesis, Massachusetts Institute of Technology, Department of Aeronautics and Astronautics, 2004.

[13] R. Wawrzaszek and M. Banaszkiewicz. Control and reconfiguration of satellite formations by electromagnetic forces. *Proceedings of 2nd Microwave & Radar Week in Poland, STW-2006*, January 2007.

[14] M. Neave and R. Sedwick. Dynamic and thermal control of an electromagnetic formation flight testbed. Master's thesis, Massachusetts Institute of Technology, Department of Aeronautics and Astronautics, 2005.

[15] A. Sakaguchi. Micro-electromagnetic formation flight of satellite systems. Master's thesis, Massachusetts Institute of Technology, Department of Aeronautics and Astronautics, 2007.

[16] D. Miller, A. Saenz-Otero, J. Wertz, A. Chen, G. Berkowski, C. Brodel, S. Carlson, D. Carpenter, S. Chen, and S. Cheng et al. Spheres: a testbed for

long duration satellite formation flying in micro-gravity conditions. *Proceedings of the AAS/AIAA Space Flight Mechanics Meeting, Clearwater, Florida*, pages 167–179, January 2000.

[17] J. Enright, M. Hilstad, A. Saenz-Otero, and D. Miller. The spheres guest scientist program: collaborative science on the ISS. *Aerospace Conference, 2004. Proceedings. IEEE*, 1, January 2004.

[18] E. M. Kong, A. Saenz-Otero, S. Nolet, D. S. Berkovitz, D. W. Miller, and S. W. Sell. Spheres as a formation flight algorithm development and validation testbed: current progress and beyond. *2nd International Symposium on Formation Flying Missions and Technologies*, 1:14–16, 2004.

[19] G. F. Franklin, J. D. Powell, and A. Emami-Naeini. *Feedback Control of Dynamic Systems.* Pearson Prentice Hall, New York, NY, 7th edition, 2014.

[20] G. Eslinger. Dynamic Programming Applied to Electromagnetic Satellite Actuation. Master's thesis, Massachusetts Institute of Technology, Department of Aeronautics and Astronautics, May 2013.

[21] B. Alvisio and A. R. Hilton. SPHERES 46th ISS Test Session Report. Technical report, MIT Space Systems Laboratory, December 2014.

[22] T. Setterfield. SPHERES 51st ISS Test Session Report. Technical report, MIT Space Systems Laboratory, January 2014.

[23] H. Kaufman, I. Barkana, and K. Sobel. *Direct Adaptive Control Algorithms: Theory and Applications.* Communications and Control Engineering Series. Springer, New York, NY, 2nd edition, 1997.

[24] J. Merk. *SPHERES Expansion Port v2 Interface Control Document.* Aurora Flight Sciences, Four Cambridge, 11th Floor Cambridge, MA 02142.

Appendix A

RINGS - SPHERES Communication Interface and API

This appendix describes the communication system between the SPHERES satellites and the RUs. The first section of this appendix explains the communication interface between the SPHERES satellites and the RUs: how to integrate a RINGS test to a GSP project and a description of the packet structure. The second section explains the SPHERES-RINGS API.

A.1 RINGS Communication Interface

Communication between the SPHERES satellites and the RUs happens through a UART connection. The UART line uses the RS-232 standard and is operated at a baud rate of 115.2kbps. The SPHERES satellites send commands to the Expansion Port Version 2 (EXPV2) [24] which in turn forwards the commands to the RU.

A.1.1 Integration of RINGS to a SPHERES GSP Project

In order to develop a project that uses the RUs, it is necessary to follow these steps:

1. The RINGS API functions (described in section A.2) are declared in two header files: `ringsUtil.h` and `ringsComm.h`. These header files should be included in

any source file that uses the API such as `gsp.c`.

2. To initialize communication with the RU, the user should call `ringsInit(...)`. A natural place to call this function is in `ringsInitProgram()` in file `gsp.c`.

3. When calling `ringsInit(...)` the user should also provide a pointer to a callback function to handle the messages (acknowledgment, error and telemetry data) received from the RUs. A default callback function is already provided by the RINGS API. This function does a minimal parsing and processing of the acknowledgment type packets. The user can provide his/her own implementation of the callback function if needed.

4. SPHERES-RINGS tests should call `ringsStartTest()` at the beginning of each test. A natural place to call this function is in `gspTestInit()` in `gsp.c`. This function should be called to ensure that the communication channel is in a valid state at the beginning of the RINGS test.

5. RINGS received messages should be downloaded to the ELC computer before the test is ended since they are not preserved across consecutive tests. It is recommended that the task of the last maneuver of any RINGS test is to download data from the SPHERES satellite to the ELC computer for post-processing. As it is explained in section A.2, RINGS received data is accessible through the RINGS API.

6. SPHERES-RINGS tests should call `ringsEndTest()` instead of `ctrlTestTerminate()` to terminate a RINGS test. A natural place to call this function is either after the last maneuver or in `gspEndTest()` in file `gsp.c`. If this is not called at the end of a test, the communication channel could be left in an invalid state.

A.1.2 RINGS Packet Structure

The RINGS packet structure consists of a header and the body of the packet of varying length. The current version of the protocol does not contain a checksum, length of the packet body or CRC. The types of packets and their respective sizes are constant.

The header of the packet is two byte long: the first byte is an 'Initialization Byte' equal to 0xFF and the second byte is the type of packet being sent or received. Figure A-1 shows the structure of the SPHERES-RINGS packets:

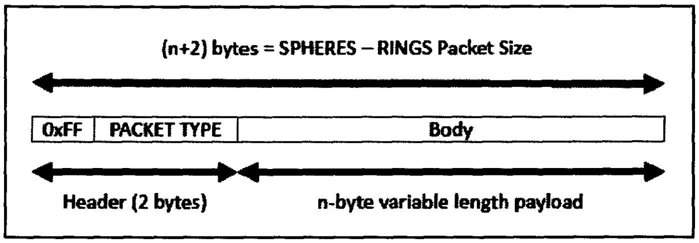
(n+2) bytes = SPHERES – RINGS Packet Size
0xFF
PACKET TYPE
Body
Header (2 bytes)
n-byte variable length payload

Figure A-1: SPHERES-RINGS Packet Structure

A.1.3 Transmitted Messages

Mode Packet

This packet commands the RUs to transition to the desired 'Operation Mode' and the frequency of operation. The byte fields of the packet are described in Table A.1:

Byte	Size(bits)	Field	Type	Description
0	1(8)	Mode	unsigned char	This field is used to specify the 'Operation Mode' that the RU should transition to. The following byte constants are used: 0x01: IDLE 0x02: EMFF 0x03: WPT-RX 0x04: WPT-TX
1-4	4(32)	Frequency (Hz)	unsigned int	This field specifies the frequency in Hz at which the RU should drive the RLC circuit.
5-8	4(32)	SPHERES Time Stamp	unsigned int	This field contains the local SPHERES time.
9	1(8)	Send Long Telemetry Packet	unsigned char	This field specifies if the RU should send periodically 'Long Telemetry Packets' back to the SPHERES satellite after transitioning to the commanded mode. The following byte constants are used: 0x00: Don't send. 0x01: Send.

Table A.1: Mode Packet Structure Details

PWM Packet

This packet is used to command the RU to drive the coil at a constant PWM duty cycle. The RU won't apply the commanded duty cycle if its current 'Operation Mode' is IDLE. The byte fields of the packet are described in Table A.2:

Byte	Size(bits)	Field	Type	Description
0-1	2(16)	Count Amplitude	unsigned short	This field specifies the PWM duty cycle. This field should contain a number between 0 (0% DC) and 200(100% DC)
2	1(8)	Phase	unsigned char	This field specifies the phase offset at which the RU should drive the RLC circuit. (RU coil). The following byte constants are used (All other values are invalid): 0d0: 0 deg Phase Offset 0d180: 180 deg Phase Offset.
3-6	4(32)	SPHERES Time Stamp	unsigned int	This field contains the local SPHERES time.

Table A.2: PWM Packet Structure Details

RMS Current Packet

This packet is used to command the RU to drive the RLC circuit at a specified constant RMS current level. The RU won't apply the command if its current 'Operation Mode' is IDLE. The RU will apply a maximum RMS current level of 15A if the RMS level value specified in the packet is 15A or greater. The byte fields of the packet are described in Table A.3:

Byte	Size(bits)	Field	Type	Description
0-3	4(32)	Command ID	unsigned int	This field contains a unique ID packet to identify the command. This ID is generated by the SPHERES satellite.
4-8	4(32)	SPHERES Time Stamp	unsigned int	This field contains the local SPHERES time.
9	1(8)	Controller Enable	unsigned char	Deprecated. Should always be set to a constant value 0x01.
10 - 13	32(4)	RMS Current Level	float	This field specifies the RMS current level.
14	1(8)	Phase	unsigned char	This field specifies the phase offset at which the RU should drive the RLC circuit. The following byte constants are used (All other values are invalid): 0d0: 0 deg Phase Offset. 0d180: 180 deg Phase Offset.
15 - 18	32(4)	Proportional Gain	float	This field specifies the Proportional Gain used in the PI current controller.
19 - 22	32(4)	Derivative Gain	float	Deprecated. Should be set to 0x00.
23 - 26	32(4)	Integral Gain	float	This field specifies the Integral Gain used in the PI current controller.

Table A.3: RMS Current Packet Structure Details

A.1.4 Received Messages

Short Telemetry Packet

This packet is sent from the RU to the SPHERES satellite at a fixed frequency of $3Hz$. The data received in this packet can be used for real-time operations, health monitoring of the RU and for post-processing of the data. The byte fields of the packet are described in Table A.4:

Byte	Size(bits)	Field	Type	Description
0-3	4(32)	SPHERES Time Stamp	unsigned int	This field contains the last SPHERES time stamp that was received from the SPHERES satellite
4-5	8(16)	RMS Current	unsigned short	This field contains RMS current measured by the RMS Chip 2 in the RU. The value is given in counts and can be converted to Amperes using the conversion formula listed in Table A.8.
6-7	2(16)	Load Power	unsigned short	This field contains the power that is being generated by the RU. Note that this field is only meaningful when the RU 'Operation Mode' is WPT-RX. The value is given in counts and can be converted to Amperes using the conversion formula listed in Table A.8 and RLC circuit resistance.
8-9	2(16)	Coil Temperature	unsigned short	This field contains the RU coil temperature measured by the temperature sensor. The value is given in counts and can be converted to temperature units using Table A.8
10-11	2(16)	Exit Air Temperature	unsigned short	This field contains the measured temperature by the sensor located at the Exit Air Fans. (For a detailed description of the sensors and its physical location see [2]). The value is given in counts and can be converted to temperature units using Table A.8
12-13	2(16)	Duty Cycle	unsigned short	This field contains the duty cycle being applied to the RLC circuit. Note that this value is meaningful only when a PWM command was issued and PI current controller is disabled.
14-15	2(16)	Short Telemetry Packet Count	unsigned short	This field contains the 'Short Telemetry Packet' sequential number that has been sent from the RU to the SPHERES satellite since the last RU reset.
16-19	4(32)	Time Elapsed	unsigned int	This field contains the time in milliseconds elapsed since the last SPHERES time stamp received. (See SPHERES Time Stamp field)
20-23	4(32)	Reference RMS Current	float	This field contains the reference RMS current level used by the PI current controller. Note that this value is meaningful only when the current controller is enabled.
24	1(8)	Reference Phase	unsigned char	This field contains the Reference Phase Offset.
25	1(8)	Not Used	-	-

Table A.4: Short Telemetry Packet Structure Details

Long Telemetry Packet

This packet is sent from the RU to the SPHERE satellite at 30 times the operation frequency only when the 'Send Long Packet' byte is set. (See Mode Configuration Packet section A.1.3). The byte fields of the packet are described in Table A.5:

Byte	Size(bits)	Field	Type	Description
0-1	2(16)	Long Telemetry Packet Count	unsigned char	This field contains the Long Telemetry Packet sequential number that has been sent from the RU to the SPHERES satellite since the RU last reset.
2-5	4(32)	SPHERES Time Stamp	unsigned int	This field contains the local SPHERES time.
6-9	4(32)	Time Elapsed	unsigned int	This field contains the time in milliseconds elapsed since the last SPHERES time stamp received. (See 'SPHERES Time Stamp' field)
10-11	2(16)	unused	-	-
12 - 191	90x 2(16)	Instantaneous Current	unsigned short	These fields (90 samples) contain the current in the RLC circuit measured by Hall-Effect sensor in counts. (See Table A.8 for conversion formula)

Table A.5: Long Telemetry Packet Structure Details

Operation Mode Acknowledgment Packets

This packet is sent from the RU to the SPHERE satellite to acknowledge the valid transition to the commanded 'Operation Mode'. The byte fields of the packet are described in Table A.6

Byte	Size(bits)	Field	Type	Description
0	1(8)	Operation Mode	unsigned char	This field contains the new 'Operation Mode' that the RU transitions to.
1-4	4(32)	Operation Frequency (Hz)	unsigned int	This field specifies the frequency at which the RU should drive the RLC circuit. (Not applicable when the RU transitions to IDLE mode.)

Table A.6: Operation Mode Acknowledgment Packet Structure Details

A.1.5 Telemetry Data Conversion Tables

Tables A.7 and A.8 contain RUs sensor value gains, physical parameters and references to convert received telemetry data to physical units.

Element	Units	Value
BCS RU - HES 1 - 83Hz	[mV/A]	48.74
BCS RU - HES 2 - 83Hz	[mV/A]	49.44
BCS RU - HES 3 - 83Hz	[mV/A]	51.35
BCS RU - HES 1 - 462Hz	[mV/A]	49.76
BCS RU - HES 2 - 462Hz	[mV/A]	50.51
BCS RU - HES 3 - 462Hz	[mV/A]	52.34
CCS RU - HES 1 - 83Hz	[mV/A]	48.98
CCS RU - HES 2 - 83Hz	[mV/A]	49.43
CCS RU - HES 3 - 83Hz	[mV/A]	51.34
CCS RU - HES 1 - 462Hz	[mV/A]	49.28
CCS RU - HES 2 - 462Hz	[mV/A]	49.62
CCS RU - HES 3 - 462Hz	[mV/A]	51.63
Gray RU - HES 1 - 83Hz	[mV/A]	49.11
Gray RU - HES 2 - 83Hz	[mV/A]	49.63
Gray RU - HES 3 - 83Hz	[mV/A]	51.15
Gray RU - HES 1 - 462Hz	[mV/A]	49.37
Gray RU - HES 2 - 462Hz	[mV/A]	50.17
Gray RU·- HES 3 - 462Hz	[mV/A]	51.46
Bronze RU - HES 1 - 83Hz	[mV/A]	49.10
Bronze RU - HES 2 - 83Hz	[mV/A]	50.30
Bronze RU - HES 3 - 83Hz	[mV/A]	51.53
Bronze RU - HES 1 - 462Hz	[mV/A]	49.58
Bronze RU - HES 2 - 462Hz	[mV/A]	50.90
Bronze RU - HES 3 - 462Hz	[mV/A]	51.96
RU RLC Resistance	$[\Omega]$	1.2
RU RLC Inductance	$[mH]$	11.9
RU RLC Capacitance - EMFF	$[pF]$	310

Table A.7: RINGS Units Sensor Gains and Physical Parameters

Element	Units	Function
RMS Current	A	$= ([counts] * (3300/1024) * (1/Gain_{HESensor})$
Coil & Exit Air Temperature	C	$= (([counts] * 3300/1024) - 500) * 0.1$
Duty Cycle	%	$= [counts]/2$

Table A.8: Telemetry Data Conversion Factors

A.2 SPHERES - RINGS API

The SPHERES - RINGS API is composed of 6 functions that are declared in different header files according to their logical functionality. These header files should be included in any SPHERES-RINGS project source files that needs to. call these functions.

Header File ringsComm.h

Prototypes for the following functions can be found in the file `ringsComm.h`

void ringsSetCurrent(...)		
Sets the RMS current through the RLC circuit to the specified value.		
1	float	RMS current level in Amperes to be set. Negative values are interpreted as having a 180 degree phase offset. Note: The absolute maximum value for this parameter is 15. Any value greater than 15 or less than -15 will be interpreted as 15A and -15A respectively.
2	float	Current Controller Proportional Gain.
3	float	Current Controller Derivative Gain. Note: This value can be set to 0 given that most recent version of controller only uses Proportional and Integral gains.
4	float	Current Controller Integral Gain.

int ringsSetDC(...)		
Sets the Duty Cycle of the RU's RLC circuit.		
1	unsigned char	Duty Cycle. Note: The absolute maximum value for this parameter is 100. Returns zero for success, or error '-1' if an illegal parameter is passed.
2	unsigned char	Phase Offset. Logical Identifier: ZERO_PHASE or OUT_PHASE.

int ringsSetMode(...)		
Sets the Operational Mode of the RU. Returns zero for success and '-1' if an illegal parameter is passed		
1	unsigned char	Operation Mode. Logical Identifier: IDLE_MODE, EMFF_MODE, WPTTX_MODE, WPTRX_MODE
2	unsigned int	The operational frequency at which the RLC should be driven. Note: Not applicable when transitioning to IDLE Mode.

Header File ringsUtil.h

Prototypes for the following functions can be found in the file **ringsUtil.h**

void ringsInit(...)		
		Initializes the UART connection with the RU and sets internal state variables. This function must be called once in function: void gspInitProgram() in file gsp.c
1	EXPv2_CFG_CBK	Callback function that will be registered when Configuration data is received from the Expansion Port Version 2. If null no function will be registered.

void ringsStartTest()
Sets internal state variables. This function must be called at the start of every RINGS test. It is recommended to call this function in: void gspInitTest() in file gsp.c

void ringsEndTest()
Sets internal state variables. This function must be called at the end of every test. It is recommended to call this function after the last maneuver and in: void gspEndTest() in file gsp.c

Appendix B

SPHERES - RINGS Simulation - Payload UART TX/RX MATLAB Code

```
function [UARTTx] = Payload(UARTRx)

% INITIALIZATION INTERNAL VARIABLES
%%%%%%%%%%%%%%%%%%%%%%%%%%%%%%%%%%%
% UART RX Code
%%%%%%%%%%%%%%%%%%%%%%%%%%%%%%%%%%%
persistent RxBuf pw pr TxBuf;
if (isempty(RxBuf) || isempty(TxBuf) || isempty(pr) || isempty(pw))
    RxBuf = zeros(2,1e5,'uint8');
    TxBuf = zeros(2,1e5,'uint8');
    pw    = [0,0;0,0]; % Rx/Tx read/write pointers
    pr    = [0,0;0,0]; % First column for Rx; Second Column for Tx
end

% COLLECT DATA INTO RxBuffer
if UARTRx.channel1.size
    for i=1:UARTRx.channel1.size
```

```
        RxBuf(1, pw(1)+1) = UARTRx.channel1.data(i);
        pw(1) = pw(1) + 1;
    end
end

if UARTRx.channel2.size
    for i=1:UARTRx.channel2.size
        RxBuf(2, pw(2)+1) = UARTRx.channel2.data(i);
        pw(2) = pw(2) + 1;
    end
end
%%%%%%%%%%%%%%%%%%%%%%%%%%%%%%%%%%%
% END UART RX Code
%%%%%%%%%%%%%%%%%%%%%%%%%%%%%%%%%%%



%%%%%%%%%%%%%%%%%%%%%%%%%%%%%%%%%%%
% UART TX Code
% User should call addToTxQueue(...) to send data back to SPHERES
%%%%%%%%%%%%%%%%%%%%%%%%%%%%%%%%%%%
if pw(1,2)>pr(1,2)
    % There is data to be sent out
    len = min( pw(1,2)-pr(1,2) , 12 );
    UARTTx.channel1.size = uint8(len);
    for i=1:12
        if i<=len
            UARTTx.channel1.data(i) = TxBuf(1,pr(1,2)+i);
        else
            UARTTx.channel1.data(i) = uint8(0);
        end
    end
    pr(1,2) = pr(1,2) + len;
else
    UARTTx.channel1.size = uint8(0);
end
```

```
if pw(2,2)>pr(2,2)
    % There is data to be sent out
    len = min( pw(2,2)-pr(2,2) , 12 );
    UARTTx.channel2.size = uint8(len);
    for i=1:12
        if i<=len
            UARTTx.channel2.data(i) = TxBuf(2,pr(2,2)+i);
        else
            UARTTx.channel2.data(i) = uint8(0);
        end
    end
     pr(2,2) = pr(2,2) + len;
else
    UARTTx.channel2.size = uint8(0);
end


function [TxBuf,pw] = addToTxQueue(chan,msg,TxBuf,pw)
len = length(uint8(msg));
TxBuf(chan,pw(chan,2)+1:pw(chan,2)+len) = uint8(msg);
pw(chan,2) = pw(chan,2) + len;
%%%%%%%%%%%%%%%%%%%%%%%%%%%%%%%%%%%
% END UART TX Code
%%%%%%%%%%%%%%%%%%%%%%%%%%%%%%%%%%%
```